INTERACTIONS OF ANILINE OLIGOMERS WITH IRON OXIDE SURFACES

INTERACTIONS OF ANILINE OLIGOMERS WITH IRON OXIDE SURFACES

BY

TANZINA CHOWDHURY,

M.Sc. (Umeå University, Sweden) 2008

A Thesis

Submitted to the School of Graduate Studies

in Partial Fulfillment of the Requirements

for the Degree Doctor

of Philosophy

in

Chemistry

DOCTOR OF PHILOSOPHY (**2016**) McMaster University

(Chemistry and Chemical Biology) Hamilton, Ontario

TITLE: Interactions of aniline oligomers with iron oxide surfaces.

AUTHOR: Tanzina Chowdhury

SUPERVISOR: Dr. Peter Kruse

NUMBER OF PAGES: xxii, 174

ABSTRACT

Aniline oligomers have become a very interesting topic for research because of their potential application not only in organic electronics but also in smart coatings for corrosion treatment of iron and steel. A majority of the studies in the literature are focussed on the bulk or direct interaction between the organic molecules with metal substrates, without considering the native oxide film. In order to develop smart coatings (has redox activity and self-healing ability) for iron and steel, one must first understand how these oligomers interact with the native iron oxide film. In this thesis, we develop new knowledge from our fundamental understanding of the interactions of redox-active aniline oligomers with the iron oxide surface. Phenyl capped aniline dimer with two oxidation states [fully reduced (DPPD) and fully oxidized (B2Q1)] and phenyl-capped aniline tetramer (PCAT) with three oxidation states [fully reduced (B5), half-oxidized (B4Q1), fully oxidized (B3Q2)] were chosen for investigation. The former is the smallest redox active aniline oligomer but with one fewer oxidation states than polyaniline whereas the latter mimics the redox system as well as corrosion inhibition properties of polyaniline. Moreover, the phenyl-caps help both of these molecules to resist polymerization on the surface. Raman spectroscopy, mid-IR spectroscopy, atomic force microscopy (AFM), temperature programmed desorption (TPD) and electrochemical impedance spectroscopy (EIS) were used to study interactions. We demonstrate that charge transfer and interconversion to different oxidation states take place during interactions between each of these molecules with iron (III) oxides surfaces. During interaction with the surface, all three tetramer molecules and DPPD prefer standing on

their edge orientation, whereas B2Q1 molecules tend to orient in lying down direction on the same surface. Having amino groups in the chain helps reduced and half oxidized molecules to strongly hydrogen bond with the surface and make them static on the surface. On the other hand, a lack of amino groups makes oxidized molecules mobile and loosely bound to the surface. Interactions and change of oxidation states impact the corrosion inhibition properties of PCAT. Strong ability of sticking to the surface and not fully oxidizing (B3Q2) during interactions makes B5 molecules superior corrosion inhibitors than B4Q1 and B3Q2 molecules. Transformation into B3Q2 form at the beginning of interaction allows B4Q1 to moderately inhibit corrosion but as it transforms back to its original form with time it becomes the 2nd best corrosion protector of iron oxide surface after B5. The study of all oxidation states and their surface interactions with iron oxide surface will open up pathways towards of designing smart coatings using aniline oligomers and other redox-active molecules.

ACKNOWLEDGEMENTS

I would like to express my sincere gratitude to all the wonderful persons who have supported me throughout this work. In particular, I am especially grateful to:

Dr. Peter Kruse, my supervisor, who with his guidance, patience, scientific skill and generosity guided me into the world of surface science. His wisdom and firmness have contributed significantly to face the challenges in science and be successful to find a needle from the hay. His unwavering enthusiasm about physical chemistry kept me constantly engaged with my research and his personal generosity helped make my time in McMaster University enjoyable.

Drs. Kalai Saravanamuttu and Joey Kish, who served as my committee members. I also thank them for constantly pushing me to think, asking the relevant questions and for their brilliant comments and suggestions.

Dr. Stephen Wang, Amirmasoud Mohtasebi, Dr. Enamul Hoque and Allen Pauric my previous and present group members who encouraged me in the graduate study and discussed with me about different academic and non-academic issues. I also cannot forget a young and energetic undergrad student in our group Alan Awez who demised last year.

Connie Carrabs, Christine Cosgrove, Jane Garneau, Linda Spruce and **ABB community**, administrators and office staffs who helped me with administrative support. They are a group of nice people with nice smiles who always encourages the grad student to fulfill their goals.

Dr. Kirk Green and **Leah Allan** from the McMaster regional mass spectrometry facility for their technical assistance and helpful discussions. **Dr. Steve Kornic** (CAOS), and **Frank Gibbs** (BIMR) for assistance with Raman spectroscopy and thermal analysis, respectively. **Drs. Ferenc Borondics**, **Scott Rosendahl**, and **Xia Liu** at CLS for their assistance with mid-IR spectroscopy.

Dr. Mozibur Rahman, my husband and my best friend. Without his back-up and support, I could not come to this point. He is my champion and words are not enough to express how meaningful he is in my life. Moreover, **Yazdan** and **Rayan**, my two boys who blessed my life with joy. They never complain about not giving them enough time due to my busy schedules at Mcmaster and frequent visits to Saskatchewan for experiments.

My **parents (Azamza Chowdhury and Sajeda Kohinoor),** who brought me to life and wish me the best all the time. They always have faith in me and supported me although they live far away.

My **Siblings (Dr. Rezaul Alam Chowdhury and Tasnuva Chowdhury),** who always supported me and kept confidence in me that one day I will be able to fulfill my dream.

TABLE OF CONTENTS

LIST OF FIGURES

LIST OF TABLES

LIST OF ABBREVIATIONS

AC	Alternating current
AFM	Atomic Force Microscope
ATR	Attenuated total reflection
BSE	Backscattered electrons
B2Q1	N,N′-Diphenyl-1,4- benzoquinonediimine Pernigraniline forms phenyl-end-capped dimer (2 benzene and 1 quinoid rings)
B3Q2	Pernigraniline forms phenyl-end-capped tetramer (3 benzene and 2 quinoid rings)
B4Q1	Emeraldine forms phenyl-end-capped tetramer (4 benzene and 1 quinoid rings)
B5	4-(phenylamino) phenyl]-1,4-benzened (Leucoemeraldine form of phenyl-end-capped tetramer, 5 benzene rings)
CLS	Canadian Light Source
DPPD	N,N′-Diphenyl-1,4-phenylenediamine (Leucoemeraldine form of

	phenyl-end-capped dimer, 3 benzene rings)
DTA	Differential thermal analyzer
DTG	Derivative thermogravimetric
EB	Emeraldine base
EIS	Electrochemical impedance spectroscopy
FTIR	Fourier Transform Infrared
GIR	Grazing incidence of reflection
IR	Infrared
NP	Nanoparticles
PCAT	Phenyl-capped aniline tetramer
SCC	Stress corrosion cracking
SCE	Saturated calomel electrode
SEM	Scanning electron force microscopy
TGA	Thermal gravimetric analysis
TPD	Temperature programmed desorption
WE	Working electrode
2D	Two-dimensional

DECLARATION OF ACADEMIC ACHIEVEMENT

This thesis consists of six chapters that include manuscripts of three scientific papers. Chapter 3 is based on the manuscript "Nature of the interaction of N'N-diphenyl-1,4 phenylenediamine with iron oxide surfaces" that has been accepted for publication in the Journal of Physical Chemistry C (JPCC) 121 (2017) 2721-2729. Contributions for the work presented in chapter 3 are as follows: the author of the thesis designed the experiments after consulting with the mentor Dr. Peter Kruse. All the experiments, data analysis, and figure were done by the author. The manuscript drafts were written by the author as well, with some assistance of Dr. Peter Kruse. Other people who contributed to the work in this chapter are Amirmasoud Mohtasebi**,** Dr. Enamul Hoque participated with some helpful discussion. Moreover, Amirmasoud Mohtasebi helped with the handling the vacuum chamber.

Chapter 4 is based on the manuscript "Nature of the interaction of N'N-diphenyl-1,4-benzoquinonediimine with iron oxide surfaces and its mobility on the same surfaces" that has been accepted for publication in the Journal of Physical Chemistry C (JPCC) 121 (2017) 2294-2302. This manuscript was written by the author of the thesis under the supervision of Dr. Peter Kruse. All the experiments were performed; data and figures were analyzed by the author as well. Amirmasoud Mohtasebi participated in the discussion and helped with the vacuum chamber.

Chapter 5 is based on the manuscript “Interactions of different redox states of phenyl-capped aniline tetramers with iron oxide surfaces and consequences for corrosion inhibition” that has been submitted for publication in the Journal of the Electrochemical Society (ECS). The thesis author wrote the manuscript with the guidance of Dr. Peter Kruse. As before, all the experiments were performed for the work as well as data analysis was done by the thesis author. Several individuals participated in the helpful discussions namely, Dr. Peter Kruse, Dr. Joey Kish, Dr. Sarah Xang and Amirmasoud Mohtasebi. Dr. Sarah Xang helped with the electrochemical impedance spectroscopy system and Amirmasoud Mohtasebi with the vacuum chamber. Svetlana Kostina performed the synthesis of PCAT.

The rest of the thesis including the introduction (chapter 1), experimental methods (chapter 2) and summary and future work (chapter 6) were solely written by the thesis author.

CHAPTER - 1
INTRODUCTION

1.1 CORROSION

Corrosion is an electrochemical reaction between metals and their surrounding environment which causes degradation of the metal and also sometimes changes its properties (thermal conductivity and electrical properties etc). It is an ancient problem causing million dollars of loss in almost every country in the world. The cost of corrosion has been reported to be in the order of 1–5% of gross national product for most countries.[1] Among metals, iron and steel corrosion are very well-known. Corrosion processes take place in metals in the form of an active electrochemical cell, consisting of an anode, a cathode, an electrolyte and an electron path.[2,3] The anodic site of the cell is where metal atoms lose electrons to become positively charged, called oxidation reaction. Oppositely, at the cathodic site, those electrons are consumed and the negatively charged ion is produced, which is the reduction reaction.[4] The electrolyte is a conductive solution which conducts electricity through movement of ions. The positive ions move towards the cathodic site, whereas negative ions move towards the anodic site. The electron path can be the corroding conductive metal.[2] The corroded metal acts as an anode because it gets oxidized easily in ambient water containing dissolved atmospheric oxygen. This reaction releases metal ions and electrons.[5]

In iron and steel, the principle anodic reaction is $Fe \rightarrow Fe^{2+} + 2e^-$

The corresponding cathodic reaction is $\frac{1}{2}O_2 + H_2O + 2e^- \rightarrow 2OH^-$

$$Fe^{2+} + 2OH^- \rightarrow Fe(OH)_2$$

$$2Fe(OH)_2 + H_2O + \frac{1}{2}O_2 \rightarrow 2Fe(OH)_3$$

The released electrons reduce the oxygen and produce OH^-, this is a cathodic reaction. Then the Fe^{2+} and OH^- ions can combine to form solid $Fe(OH)_2$, which may undergo further oxidation and form hydrated iron (III) oxide.[4]

Controlling the corrosion on any surface requires a deeper understanding of the corrosion process and type. Some commonly distinguished types of corrosion are described below.

General or **uniform** attack is an electrochemical reaction during which an exposed metal surface is oxidized uniformly. It makes the metal part thinner without any localized corrosion which can eventually cause functional failure.[6] Iron or steel rusting in air are a well-known example of uniform corrosion as discussed above. Uniform corrosion is the most predictable form of corrosion which can be prevented by knowing the process well.[6] Applying a coating or paint, and choosing uniformly microstructured materials are possible ways to prevent this kind of corrosion.[4] General corrosion can be of several kinds, out of them the main two types are **galvanic** corrosion and **atmospheric** corrosion. **Galvanic** corrosion is an electrochemical way of attacking metals when two metals have a difference in electrochemical potential and have a conducting path between them. Through that conducting path, metal ions transfer from the anodic site to the cathodic site during corrosion and form a galvanic cell.[4,6] In a galvanic cell, the more noble metal always acts as a cathode and the less noble metal or metal with more negative potential always acts as the anode. For the electron to travel, the metal surface becomes a conductive path, and the moisture forms the base for the electrolyte. Selecting two metals or alloys with similar or very close electrode potentials to form the galvanic coupling

and using metallic coatings (two types: sacrificial and noble) are possible ways to prevent this kind of corrosion.[2] In **atmospheric** corrosion, the entire exposed metal surface is oxidized due to the corrosive environment. Rusting of steel in the air is an example of this kind of corrosion. This kind of corrosion does not go very deep inside the metal.[2]

Corrosion can also happen at specific sites of the exposed area. This kind of corrosion is known as localized corrosion. Some of the main kinds of localized corrosion are pitting corrosion, crevice corrosion, and erosion corrosion. **Pitting** corrosion initiates by forming very tiny holes on the metal surface which are very difficult to detect visually. Sometime in the corrosive environment, the depth of a pit can grow so fast that the metal becomes un-repairable and looses its functionality. Pitting can initiate in a defect site of the metals due to damage in the protective coatings, mechanical imperfections in the material, etc.[4,6] **Crevice** corrosion is a localized type of corrosion that can attack any shielded area and crevices of the metal surface due to a corrosive environment. This type of corrosion can start initially with a minor localized hole and with time can become aggressive.[4,6] Crevice corrosion is a kind of pitting corrosion. This type of corrosion can take place due to local changes in the chemical properties of the metal such as an increase in the Cl^- ion concentration, a change in pH due to a change in the H^+ ion concentration and decrease of oxygen reduction or cathodic reaction in the crevices.[4] Using proper sealing and coating can reduce this type of corrosion. The corrosion that takes place due to the movement of corrodent over the metal surface is known as **erosion** corrosion. This localized attack takes place due to damage or scratches in protective coatings.[6]

The loss due to corrosion can be huge. Simple metal loss can be related to the loss of operation efficiency and structure of the system and sometimes even requires expensive

replacement of any system. Most importantly it can cause fatal injuries to people due to structure failure of the bridge, cars or aircraft. Moreover, even corrosion product contamination could be a human health hazard. By understanding the different corrosion processes it is possible to prevent their aggressiveness on different surfaces. Some of the prevention mechanisms are discussed in the next section.

1.2 CORROSION INHIBITION

In reality, it is not usually feasible to completely eliminate all corrosion damage but its severity can be reduced by using different methods. There are several methods to inhibit corrosion which includes proper material selection and design, cathodic protection, anodic protection, barrier coatings, and using coating inhibitor etc. For designing the material there are four steps that are followed by corrosion engineers. Those are i) defining the materials functionality, ii) defining the tolerance of the corrosion environment of the materials, iii) material selection for designing and iv) inspection of the designed material.[7]

Cathodic protection is a widely used method for corrosion control mostly for metal with water contact. In the corrosion process, current flows between the anodic and cathodic site in a metal due to the potential difference. In the cathodic protection, the anodic reaction is suppressed by supplying more electrons to the structured metal which eventually would increase the rate of cathodic reaction in the metal. This reduces the corrosion rate by decreasing the rate of the oxidation reaction of the metal.[2]

Anodic protection is just opposite to cathodic protection, which is suitable to prevent corrosion of a metal in aggressive environments like sulfuric acid. In this method, corrosion is prevented by applying a sufficient current to make the potential anodic or positive to produce a passive oxide film on the structured metal. The potential is supposed to be sufficiently anodic to passivate the metal otherwise it will remain active and continue to grow native oxides.[2,3]

Physical barrier coating is the most commonly used corrosion control technique. It separates or isolates the metal from the corrosive atmosphere. Types of coatings include metallic, non-metallic inorganic and organic. These coatings can be applied individually or combination with others depending on needs. Coatings can inhibit corrosion using any of three different mechanisms such as barrier protection, galvanic protection, and chemical inhibition. In the **barrier protection,** the inhibition can be done by either resistance inhibition in which the coating inhibits the current flow between cathodic and anodic sites or it can be done by causing oxygen deficiency at the metal surface to stop the cathodic reaction.[8] In **galvanic protection,** an active metal (zinc) is used as a coating on the substrate metal. The metal used for this type of coating has a more negative electrochemical potential than the substrate metal. The substrate metal becomes cathodic in this case because all the current flows from the coated metal. As a result, the oxidation reaction happens in the coated metal and the underlying substrate is being saved. This coated metal is known as a sacrificial anode.[2,7,8]

In 1985 David DeBerry *et al* [9] observed reduced corrosion rates of polyaniline (PANI) coated stainless steel in an acidic medium which he deposited electrochemically onto it. He concluded anodic protection was achieved via passive oxide formation on stainless steel by

polyaniline coating.[9,10] Due to this very important property of polyaniline, its derivatives and as well as other polymers with similar properties have been identified and utilized.[10-13]

PANI exists in three different oxidation states and also several protonation states as well. Iron (Fe) has two common oxidation states which also involve oxides and oxyhydroxides. As a result when theses two species are combined, the system becomes quite complex to study and understand.[14] Studies show that PANI in contact with the iron surface causes the growth of a gray film underneath the coating on the surface by passivating the iron.[10,14] This means a chemical reaction takes place at the interface of the PANI-Fe system during contact. Even though it is generally understood that PANI inhibits corrosion by forming a passive oxide, details of the chemical process behind the passivation are still not yet resolved.[10,14,15] It was suggested by Wessling et al. that PANI can act as a catalyst by oxidizing iron to the passive state.[10] From the fully oxidized form, PANI becomes reduced by oxidizing or passivating iron. Again from the fully reduced or half oxidized form, it converted back to its initial oxidized form by atmospheric oxygen.[15] Other than inhibiting corrosion polyaniline film have the remarkable property of self-healing which makes them unique compared to conventional organic coatings.[14,16] This self-healing ability of PANI is known as "throwing power". This throwing power means PANI coating can protect underlying substrates even where they are not directly covering the surface, such as the scratched-out region on the coatings.[11,17]

Although PANI has all these outstanding properties, it is not free from disadvantages. First of all, poor solubility of PANI in benign solvents is a great issue as well as difficulty to get well defined organic thin films by vacuum deposition. The main drawback with PANI coating is that in the presence of a larger defect the coating can break down catastrophically due to

conductivity and long range interactions which can cause fast reduction of the caoting.[18] This issue may be avoided through the use of shorter chain oligomers. Moreover, some aniline oligomers can mimic the redox states of PANI and can inhibit corrosion to the same degree as PANI.[13,19] To understand the corrosion inhibition mechanism, shorter chain length oligomers are better model systems because they are well defined, simple systems and can be vacuum deposited easily. This thesis work was focused on simplified models of a corrosion inhibitor, some of the shortest redox active oligomers of polyaniline, namely the phenyl-capped dimer and the phenyl-capped aniline tetramer (PCAT) (Figure 1.1. The phenyl-capped dimer is the shortest chain among the oligomers of PANI and it has two oxidation states, the fully reduced form N'N-Diphenyl-1,4 phenylenediamine (DPPD) and the fully oxidized form N,N'-Diphenyl-1,4 benzoquinonediimine (B2Q1). These dimers have fewer redox states than PANI because they have only two nitrogens atoms in the molecular chain, whereas at least four nitrogens are needed to fully mimic the three major oxidation states of polyaniline. However, for a detailed understanding of the interactions in the PANI–Fe system, investigation of these molecules is nevertheless an important first step. The imine form of the phenyl-end capped-dimer can mimic the same constituting units as the pernigraniline base or fully oxidized form of PANI whereas DPPD can mimic the leucoemeraldine or fully reduced form of PANI. The second step of the investigation was focused on the PCAT. The PCAT coatings have been shown to have the same corrosion inhibiting ability on steel as PANI coatings.[13] It can exist in three different oxidation states [B5 (fully reduced), B4Q1 (half oxidized) and B3Q2 (fully oxidized)] and several protonation states (unprotonated semiquinone and monoprotonated). The most important thing about PCAT is that it is the shortest chained aniline oligomers which can fully mimic the

electronic behavior of PANI. So, the PCAT system was used as one of the model systems for corrosion inhibition in this study. The reason for choosing phenyl-capped molecules is that these molecules cannot polymerize on the surface unlike amino capped molecules. Another problem with amino capped molecules is that it is very difficult to vacuum deposit. As a result, phenyl capped molecules are less complex than amino-capped to study.

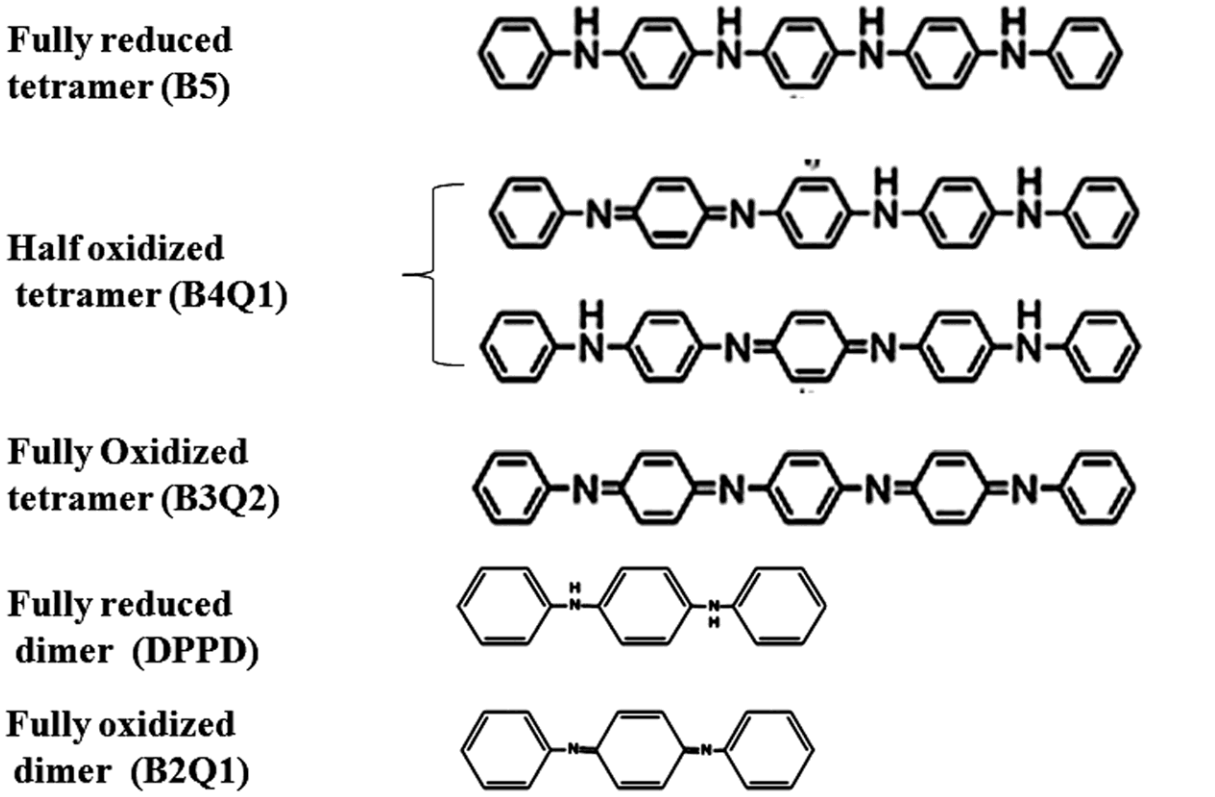

Figure 1-1. The structure of different oxidation states of phenyl-capped aniline tetramer and phenyl-capped aniline dimer.

1.3 INTERACTIONS AND MOBILITY

When molecules interact with surfaces they can interact either through Van der Waals forces or through chemical bonding. If the interaction of the molecules with the surface is very weak and the bonding depends on the molecular polarizability then the interaction is known as physisorption. On the other hand, the situation where the molecules form chemical bonds with the surface is known as chemisorption.

Chemisorbed molecules bond at specific surface sites and their interaction with the surface depends on their exact position and orientation.[21] In this kind of interaction, molecules tend to occupy high coordination sites such as oxygen molecules occupying the face centered cubic threefold hollow sites of the Pt(111) metal.[22] In the case of physisorption, molecules are only slightly bound to the surface and may experience stronger interactions between the molecules than towards the surface. This kind of absorption is common at low temperature.[21] For **non-activated adsorption,** molecules do not come across an energetic barrier (Figure 1.2). Molecules approaching the surface with low kinetic energy fall into the chemisorption well and stick to the surface. When the molecules have a higher kinetic energy they lose some energy as they strike the surface, then they recoil. This means that with increasing molecular kinetic energy the sticking coefficient decreases. In the case of **activated adsorption,** molecules experience an activation barrier as they approach the surface (Figure 1.2). Low energetic molecules cannot overcome the energy barrier but they can still physisorbed. On the other hand, molecules with a kinetic energy equal or higher than the barrier height can overcome the barrier and get trapped into the chemisorption well.[21]

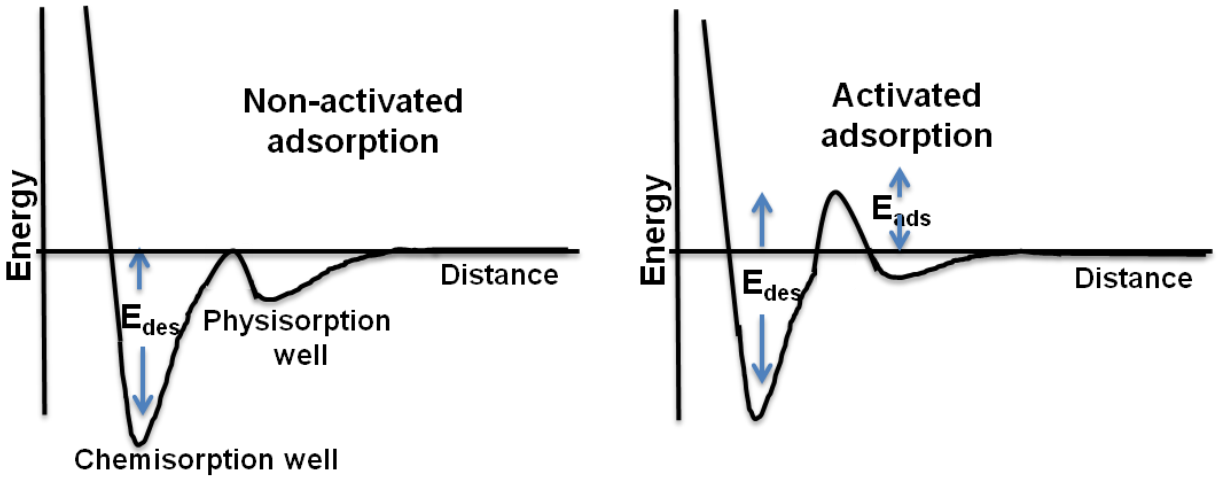

Figure 1-2. One dimensional potential energy curves for molecular adsorption.

The adsorbing molecules bring two kinds of adsorption dynamics for non-activated adsorption. Those are direct and precursor-mediated adsorption. In the case of direct adsorption, molecules can either adsorb directly by losing all their energy at the adsorption sites or lose some of their energy to be captured by the surface but still can slide or hop to one or more sites.[21] In the case of precursor-mediated adsorptions, molecules are trapped into a mobile precursor state by losing enough energy to not return to the gas phase. The precursor could be linked to either a physisorbed state or even a chemisorbed state. Whether a molecule on the surface is mobile or static depends on the strength of the interactions of the specific molecule with the surface. Knowing the interaction chemistry is the first step to understanding the mechanism of corrosion inhibition.

The mobility of molecules across surfaces is key to a wide variety of processes, including catalysis, molecular self-assembly and the formation of supermolecular structures.[23,24] A large numbers of studies have been done to understand the molecular mobility on the surface. In this

section, some of them are discussed. Metal oxide surfaces are usually hydroxylated or hydrated under ambient conditions, so it is important to know the influence of hydrogen on the diffusion processes.[24] The report by Li et al 2010,[24] about the dynamics of catechol [$C_6H_4(OH)_2$] adsorbed on rutile TiO_2(110) by scanning tunneling microscopy, gave a clear picture of that. That report showed that the molecule switches mobility by gaining or losing an extra H atom, which may enable the molecule to roll over to the next lattice site. They also suggested that the catecholate has to release and regain a H atom in order to progress across the surface; otherwise, only a back-and-forth motion between two neighboring lattice sites would be possible.[24] The influence of water vapor on the surface diffusion was also studied by Wang et al 2009.[25] They investigated the role of injected water on the diffusion of pyridine through MgO powder by Fourier transform IR (FTIR) absorption spectroscopy. Their result showed that the injection of water significantly increases the pyridine surface diffusion coefficient by displacement of the pyridine from strong adsorption sites (Lewis acid sites) to weaker hydrogen bonded sites.[25]

Another study of surface diffusion is by Shi et al 2008,[26] about the growth kinetics of tetracene films on silicon dioxide. They observed the growth of the outlines of islands formed by tetracene molecules using AFM. They concluded that the film growth is diffusion mediated. All the above studies showed that molecules are mobile on the surface. In one of the previous study of our group by Greiner et al. 2008,[17] indirect evidence of molecular mobility of aniline oligomer on the steel surface was also found. In that study reduced PCAT (Phenyl capped aniline tetramer) was deposited onto the native oxide covered iron surface using a mask to cover half of the surface to form a film with a well defined edge. The reason for using a mask was to examine the “throwing power” of PCAT. It means the power of a molecules to protect even

where it is not directly covering the surface. AFM results showed that the PCAT film spread several micrometers underneath the edge of the mask. On samples exposed to the ambient atmosphere for several days there was evidence of further spread of PCAT by as much as 800 μm, but PCAT stayed in place on fresh samples only handled in a vacuum and dry nitrogen. That study concluded that PCAT molecules are mobile on the surface and the film underneath the mask nucleates and grows based on thermal migration kinetics. An even larger value for "throwing power" was found by Fahlman et al 1997,[11] in a study of the corrosion protecting capabilities of emeraldine base polyaniline (PANI-EB). They exposed steel samples with and without protective coatings to the corrosive environment and then studied them by X-ray photoelectron spectroscopy. Their sample half coated with EB showed almost no or little corrosion, about 15mm from the edge of EB which they believe is due to "throwing power".

1.4 STRUCTURE OF THIS THESIS

The experimental methods that are used throughout the thesis are discussed in Chapter 2.

Chapter 3 contains a study of the "Nature of the interaction of N'N-diphenyl-1,4 phenylenediamine with iron oxide surfaces," as submitted for publication. In this chapter, the interaction of DPPD with iron oxide surfaces was studied by Raman and visible spectroscopy. The orientation of DPPD was first studied using mid-IR spectroscopy, comparing the intensity ratio of molecular vibrations at different polarization angles. To compliment the mid-IR results, atomic force microscopy (AFM) was used. The step height of the molecular islands as observed by AFM is used to characterized the orientation. Thermal gravimetric analysis was used to

observe the desorption energy or the energy of interaction of DPPD molecules. These energies also compliment the orientation information from mid-IR and AFM.

Chapter 4 describes a study of the "Nature of the interaction of N'N-diphenyl-1,4-benzoquinonediimine with iron oxide surfaces and its mobility on the same surfaces." This chapter utilizes the same characterization technique as Chapter 3 but on a different molecule, which is N'N-diphenyl-1,4- benzoquinonediimine (B2Q1). That chapter also shows proof of mobility of B2Q1 and also discusses the de-wetting of B2Q1 molecules.

Chapter 5, presents a study on "Interactions of different redox states of phenyl-capped aniline tetramers with iron oxide surfaces and consequences for corrosion inhibition." The interaction of three different oxidation states (reduced, half oxidized and fully oxidized) of the phenyl-capped aniline tetramer with iron oxide surfaces was studied using Raman spectroscopy. Mid-IR and AFM are used to study the orientation of all three molecules on the same surface (iron oxide). Lastly, corrosion inhibition of these molecules was tested using electrochemical impedance spectroscopy (EIS) and laser line scanning. Weight loss measurements also were performed in this chapter to confirm the inhibition efficiency.

In the last Chapter 6, all the work in this project is summarized and also future direction is discussed.

1.5 REFERENCES

(1) Reza Javaherdashti. How Corrosion Affects Industry and Life. Anti-Corrosion Meth & Material **2000**, 47 (1), 30–34.

(2) Ahmad, Z. Principles of Corrosion Engineering and Corrosion Control; Butterworth-Heinemann, 2006.

(3) Butler, G.; Ison, H. C. K. Corrosion, Design and Materials: General and Pitting. Philosophical Transactions of the Royal Society of London. Series A, Mathematical and Physical Sciences **1976**, 282 (1307), 225–234..

(4) Perez, N. Electrochemistry and Corrosion Science; Springer Science & Business Media, 2004

(5) Talbot, D. E. J.; Talbot, J. D. R. Corrosion Science and Technology; CRC Press, 2010.

(6) P.E, P. A. S. Corrosion Engineering Handbook, Second Edition - 3 Volume Set; CRC Press, 1996.

(7) Makhlouf, A. S. H. Handbook of Smart Coatings for Materials Protection; Elsevier, 2014.

(8) Revie, R. W. Corrosion and Corrosion Control; John Wiley & Sons, 2008.

(9) DeBerry, D. W. Modification of the Electrochemical and Corrosion Behavior of Stainless Steels with an Electroactive Coating. J. Electrochem. Soc. **1985**, 132 (5), 1022–1026.

(10) Wessling, B. Passivation of Metals by Coating with Polyaniline: Corrosion Potential Shift and Morphological Changes. Advanced Materials **1994**, 6 (3), 226–228.

(11) Fahlman, M.; Jasty, S.; Epstein, A. J. Corrosion Protection of Iron/steel by Emeraldine Base Polyaniline: An X-Ray Photoelectron Spectroscopy Study. Synthetic Metals **1997**, 85 (1–3), 1323–1326.

(12) Van Schaftinghen, T.; Joiret, S.; Deslouis, C.; Terryn, H. In Situ Raman Spectroscopy and Spectroscopic Ellipsometry Analysis of the Iron/Polypyrrole Interface. J. Phys. Chem. C **2007**, 111 (39), 14400–14409.

(13) Wei Yen; Jamasbi Homayoun; Li Shuxi; Cheng Shan; Jansen Susan A.; Sein Lawrence T.; Zhang Wanjin; Wang Ce. Corrosion Protection Properties of Coatings of the Epoxy-Cured Aniline Oligomers Based on Salt Spray and UV-Salt Fog Cyclic Tests. In Electroactive Polymers for Corrosion Control; ACS Symposium Series; American Chemical Society, 2003; Vol. 843, pp 208–227.

(14) Spinks, G.; Dominis, A.; Wallace, G.; Tallman, D. Electroactive Conducting Polymers for Corrosion Control. Journal of Solid State Electrochemistry **2002**, 6 (2), 85–100.

(15) Gabriel, A.; Laycock, N. J.; McMurray, H. N.; Williams, G.; Cook, A. Oxidation States Exhibited by In-Coating Polyaniline during Corrosion-Driven Coating Delamination on Carbon Steel. Electrochem. Solid-State Lett. **2006**, 9 (12), B57–B60.

(16) Lu, W.-K.; Elsenbaumer, R. L.; Wessling, B. Proceedings of the International Conference on Science and Technology of Synthetic Metals (ICSM ’94)Corrosion Protection of Mild Steel by Coatings Containing Polyaniline. Synthetic Metals **1995**, 71 (1), 2163–2166.

(17) Greiner, M. T.; Festin, M.; Kruse, P. Investigation of Corrosion-Inhibiting Aniline Oligomer Thin Films on Iron Using Photoelectron Spectroscopy. J. Phys. Chem. C **2008**, 112 (48), 18991–19004.

(18) Rohwerder, M.; Michalik, A. Conducting Polymers for Corrosion Protection: What Makes the Difference between Failure and Success? Electrochimica Acta **2007**, 53 (3), 1300–1313.

(19) Chen, F.; Nuckolls, C.; Lindsay, S. In Situ Measurements of Oligoaniline Conductance: Linking Electrochemistry and Molecular Electronics. Chemical Physics **2006**, 324 (1), 236–243.

(20) Poncet, M.; Corraze, B.; Quillard, S.; Wang, W.; Macdiarmid, A. G. Elaboration and Characterizations of Oligoaniline Thin Films. Thin Solid Films **2004**, 458 (1–2), 32–36.

(21) Kolasinski, K. W. Chemisorption, Physisorption and Dynamics. In Surface Science; John Wiley & Sons, Ltd, 2012; pp 85–183.

(22) Watwe, R. M.; Cortright, R. D.; Mavrikakis, M.; Nørskov, J. K.; Dumesic, J. A. Density Functional Theory Studies of the Adsorption of Ethylene and Oxygen on Pt(111) and Pt3Sn(111). The Journal of Chemical Physics **2001**, 114 (10), 4663–4668.

(23) Barth, J. Transport of adsorbates at metal surfaces: from thermal migration to hot precursors. Surface Science Reports **40**, 75-149 (2000).

(24) Li, S., Chu, L., Gong, X. & Diebold, U. Hydrogen Bonding Controls the Dynamics of Catechol Adsorbed on a TiO2(110) Surface. Science **328**, 882 -884 (2010).

(25) Wang, X. et al. Direct Spectroscopic Observation of the Role of Humidity in Surface Diffusion through an Ionic Adsorbent Powder. The Behavior of Adsorbed Pyridine on Nanocrystalline MgO. The Journal of Physical Chemistry C **113**, 2228-2234 (2009).

(26) Shi, J. & Qin, X.R. Nucleation and growth of tetracene films on silicon oxide. Phys. Rev. B **78**, 115412 (2008).

CHAPTER -2
EXPERIMENTAL TECHNIQUES

2.1 RAMAN SPECTROSCOPY

If light from a monochromatic source hits a molecule, most of the photons will scatter elastically. It means there is no energy loss or gain (frequency shift) of the scattered light. This is known as Rayleigh scattering. With lower probability, some of the photons will scatter inelastically with a vibrational energy exchange between molecules and scattered light. This is known as Raman scattering.[1]

The inelastic collision between the molecules and the incident photon which generates a frequency difference between the incident and scattered photon gives rise to a Raman spectrum. The Raman line that appears due to the higher frequency of the incident photon than the scattered photon frequency is called **Stokes line**. Oppositely, the Raman line that appears due to lower incident photon frequency than the scattered photon, is called **anti-Stokes line**.[2] In Raman spectroscopy, vibrational transitions of molecules can be detected. To generate a Stokes line, a photon interacts with a molecule in the ground state with frequency ν_0, the molecules absorbs part of the energy of the incident photon (frequency ν_m) and gives rise to emitted photon at lower frequency $\nu_0 - \nu_m$. On the other hand, to generate an anti-Stokes line, a photon after hitting a molecule which is already in vibrationally excited state, leaves the formerly vibrationally excited molecules in the ground state and re-emerges with higher frequency $\nu_0 + \nu_m$ (Figure 2.1).[3]

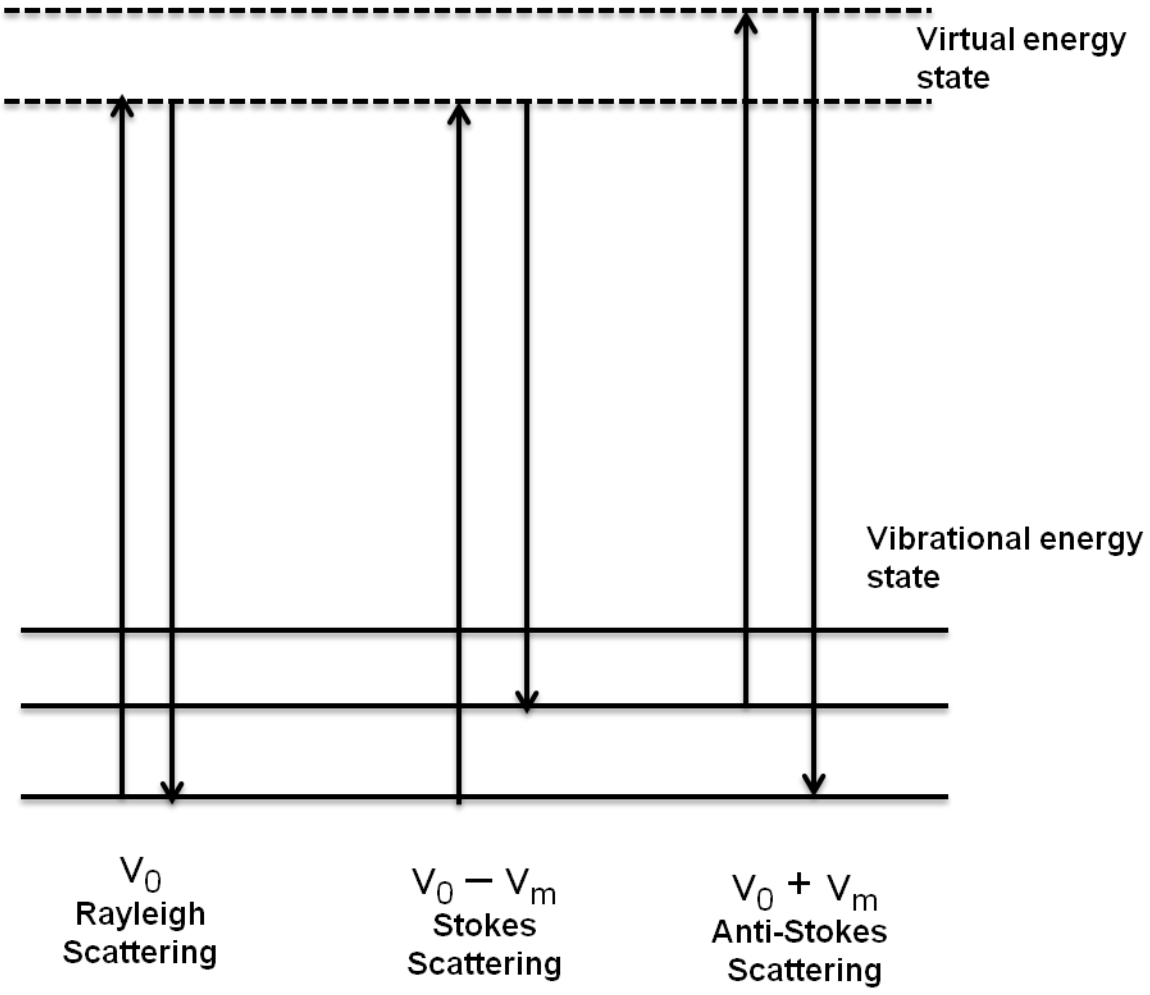

Figure 2-1. Energy level diagram for Raman scattering.

Raman scattering can also be described classically. The oscillating electromagnetic field of the incident laser light induces an electric dipole moment in the sample molecules during the interactions. The molecular vibrations change the polarizability of the molecules. This induced electric dipole moment *P* appears as the polarizability of the deformed molecules due to the external electric field. The induced electric dipole moment can be shown to be

$$P = \alpha E \qquad (1)$$

where α is the polarizability and E is the electric field.[3,4] The polarizability is a measure of the deformability of the electron cloud in a molecule or an atom by an external electric field. This distortion of the molecules happens due to the positively charged nucleus being attracted by the negative pole and the electron being attracted towards the positive pole.[3] The vibration of the deformed molecules is what the Raman spectrum shows. Since *P* and *E* both are vectors, they have three components along the x, y and z directions so the equation 1 will be expanded to be[3]

$$\begin{aligned} P_x &= \alpha_{xx}E_x + \alpha_{xy}E_y + \alpha_{xz}E_z \\ P_y &= \alpha_{yx}E_x + \alpha_{yy}E_y + \alpha_{yz}E_z \\ P_z &= \alpha_{zx}E_x + \alpha_{zy}E_y + \alpha_{zz}E_z \end{aligned} \qquad (2)$$

In matrix form the above equation can be written as[3]

$$\begin{bmatrix} P_x \\ P_y \\ P_z \end{bmatrix} = \begin{bmatrix} \alpha_{xx} & \alpha_{xy} & \alpha_{xz} \\ \alpha_{yx} & \alpha_{yy} & \alpha_{yz} \\ \alpha_{zx} & \alpha_{zy} & \alpha_{zz} \end{bmatrix} \begin{bmatrix} E_x \\ E_y \\ E_z \end{bmatrix} \qquad (3)$$

The first matrix at the right-hand side of the equation 3 is known as polarizability tensor. Which vibrations are Raman-active or not depends on the selection rules. The vibration will be Raman active if any of the components of the polarizability tensor is changed during the vibrational motion.

Since each of the atoms has 3 degrees of freedom because it can move in x, y and z-direction, N atoms have 3N degrees of freedom to move. The rules of thumb for vibrational degrees of freedom for non-linear and linear molecules are 3N-6 and 3N-5, respectively.[4] For non-linear

molecules, this 3N includes the 3 translational motions and 3 rotational motions along the principal axes of rotations. For linear molecules, it is 3N-5 because there is no rotation around the axis parallel to the bond(s) axes.[3,4] For example H_2O is a bent molecule with 3*3-6=3 normal vibrations, and the linear molecule CO_2 has 3*3-5= 4 normal vibrations.[3,4] Symmetric vibrations and stretching vibrations of molecules tend to give strong Raman signals but bending vibrations are weaker in Raman.[3,4]

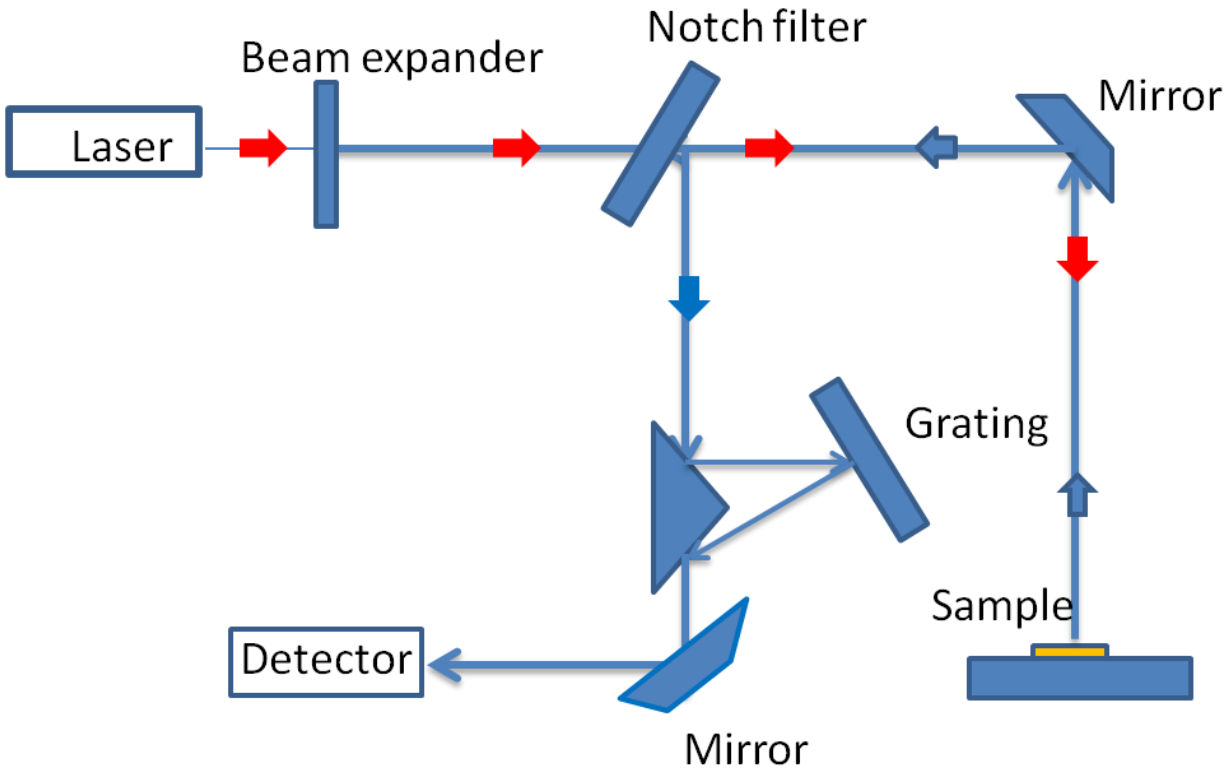

Figure 2-2. A schematic diagram of a Raman system.

Raman spectroscopy is a very powerful analytical tool. This method can very accurately determine the bonding and structure of molecules. As a result, it is used for molecularly fingerprinting not just in chemistry but also for biological materials. Raman spectra are

typically recorded in a range of 4000–10 cm^{-1} and are plotted as intensity *vs* wavelength shift. Raman spectroscopy can characterize molecules in wavenumber regions that are difficult for infrared spectroscopy (IR) to cover. For an example, metal-ligand bonds have an energy range from 100 to 700 cm^{-1}, which is in the commonly accessible Raman detection range.[5] Raman spectroscopy is also able to identify the distinct phonon modes of crystalline solid materials. This method requires no sample preparation time and experiments can be done even in a couple of seconds.

Raman scattering was discovered by C.V. Raman and K.S. Krishnan in 1928.[6] Progressively, Raman instrumentation has improved a great deal. The main components of a Raman spectrometer are excitation source (Laser), light collector, filter, monochromator, microscope and detector (Figure 2.2).

Excitation source: The laser source can be chosen based on the desired wavelength, sensitivity, and resolution required for the study.[7] Before laser sources were starting to be used, mercury arc lamps were the light source in early Raman spectrophotometers.[2] The most widely used laser sources nowadays are Argon ion lasers (488 and 514.5 nm), Krypton ion lasers (530.9 and 647.1 nm), Helium–Neon (He–Ne) lasers (632.8 nm), Near Infrared (IR) diode lasers (785 and 830 nm) and Neodymium–Yttrium Aluminum Garnet (Nd:YAG) and Neodymium–Yttrium Ortho-Vanadate (Nd:YVO_4) lasers (1064 nm).[8] Laser sources with short wavelengths (argon ion and krypton ion lasers) can cause photodecomposition of the sample and produce fluorescence whereas laser with longer wavelengths (diode or Nd:YAG lasers) can overcome those causes. On the other hand lasers with shorter wavelengths give a higher Raman

scattering probability because the intensity of the inelastically scattered light depends on the wavelength of the laser.

Filter and monochromator: Raman scattering is very weak comparing to the intense Rayleigh scattering. Various optical filters and monochromator are used to overcome that problem. In a dispersive instrument, a combination of the various notch filter and grating monochromator are most commonly used. To separate the intense Rayleigh scattered light, sometimes double or even triple monochromators can be used.[5] Among filters, holographic notch filters and dielectric edge filters are most popular. Edge filters only can filter the light wavelengths above the laser wavelengths. On the other hand, notch filters efficiently can filter the laser wavelength.[7,8]

Detector: To maximize the weak Raman signal a highly sensitive detector is required. The most commonly used detectors of the choice for Raman spectroscopy are multi-channel Charge-coupled device (CCDs) detectors. Comparing to Photomultiplier Tubes (PMT), CCD detectors show better quantum efficiencies and also lower signal to noise ratios.

2.2 MID – INFRARED SPECTROSCOPY

Infrared spectroscopy (IR) is based on the absorption of infrared light by molecules. The infrared portion of the electromagnetic spectrum can be divided into three frequency regions, the near-infrared (~14000–4000 cm^{-1}), the mid-infrared, (~4000–400 cm^{-1}) and the far-infrared (~400–10 cm^{-1}). When IR radiation passes through the sample, a part of that radiation is absorbed by the molecules at particular frequencies. Those frequencies correspond to the

characteristic vibrations of atoms or groups of atoms in those molecules.[9] Since different functional groups have their own characteristic IR peaks, IR has become a powerful tool to identify molecular compounds.

The two most important criteria for IR absorption to take place are that the frequency of light matches the energy difference between vibrational energy levels and a change in the overall molecular dipole moment during the vibration.[4] According to this selection rule, a vibration should be IR active if the rate of change of dipole moment with respect to the change of vibrational amplitude is greater than zero, $\left(\frac{\partial \mu}{\partial q}\right)_{\circ} \neq 0$, where μ is dipole moment and q is the vibrational amplitude.[3,4,10]

The IR absorption is based on the Bouguer Lambert-Beer law, [3,10]

$$I = I_{\circ} e^{-\varepsilon c d} \qquad (4)$$

Where, I and $I_{\circ}$ are the intensities of the incident and transmitted light, respectively. ε, c and d represent the molecular absorption coefficient, concentration and path length, respectively. The IR absorption spectra are commonly plotted as % transmittance (%T) (y-axis) vs wavenumber (cm^{-1}) (x-axis),

$$\%T = \frac{I}{I_{\circ}} \times 100 \qquad (5)$$

Absorbance can be obtained for quantitative analysis by the following equation.[3,10]

$$A = \log \frac{I}{I_{\circ}} = \varepsilon c d \qquad (6)$$

Two common types of vibrational modes are, stretching vibrations which involve a change in bond length and bending vibrations which are due to change in bond angle. Stretching can be symmetrical - increase or decrease in bond length simultaneously, or can be asymmetrical - where one bond length increases when another decreases. Bending vibrations can be further distinguished as scissoring, rocking, wagging, and twisting (Figure 2.3). The wagging and twisting are due to out of plane bending vibration and the other two (scissoring and rocking) are due to in-plane bending vibrations.[11]

Infrared spectroscopy is a versatile experimental technique which allows taking spectra from all sorts of samples in the liquid, solid or gaseous states. IR spectrometers have been commercialized since 1940, where dispersive elements (prism) were used to obtain spectra.[12]

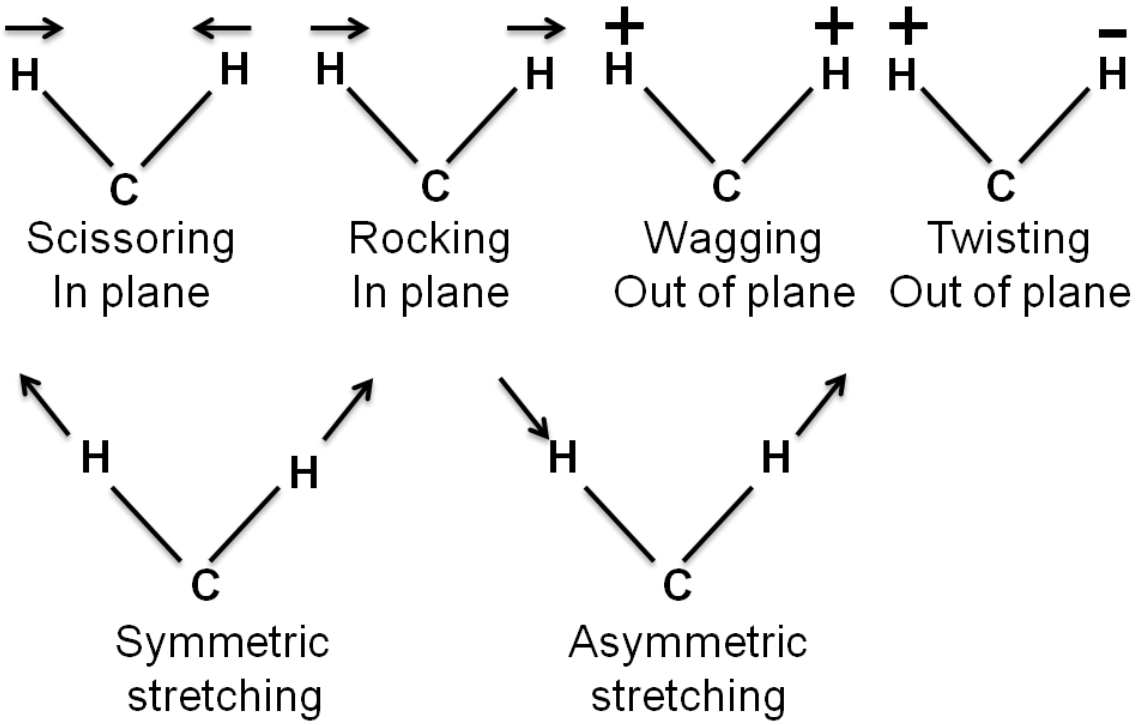

Figure 2-3. Different molecular vibrations including bending and stretching.

The second generation was introduced around the 1960s, replacing prisms with diffraction gratings as monochromators. Despite working better than prisms, they still suffered from low sensitivity and poor wavelength accuracy issues.[12] Most modern IR spectrometers are Fourier Transform Infrared Spectrometers (FTIR). They are built on the idea of a Michelson interferometer (invented by Michelson in 1891).[13] A typical FTIR spectrometer consists of a source, interferometer, sample slot, detector, amplifier and a computer. A Michelson interferometer consists of a beamsplitter, a fixed mirror, and a moving mirror as shown in Figure 2.4. When a collimated beam from the infrared radiation source is passed through the beam splitter of the interferometer, it splits the beam into two beams of nearly equal intensities. One-half of the beams are transmitted to the movable mirror and another half is reflected by the

fixed mirror. The two reflected beams from these two mirrors return to the beamsplitter and recombine. These recombined beams from the beamsplitter are then directed towards the detector through the sample. While passing through the sample, selective absorption takes place. In the detector, the difference of the intensity of these two beams is measured as a function of the path difference Figure 2.4.

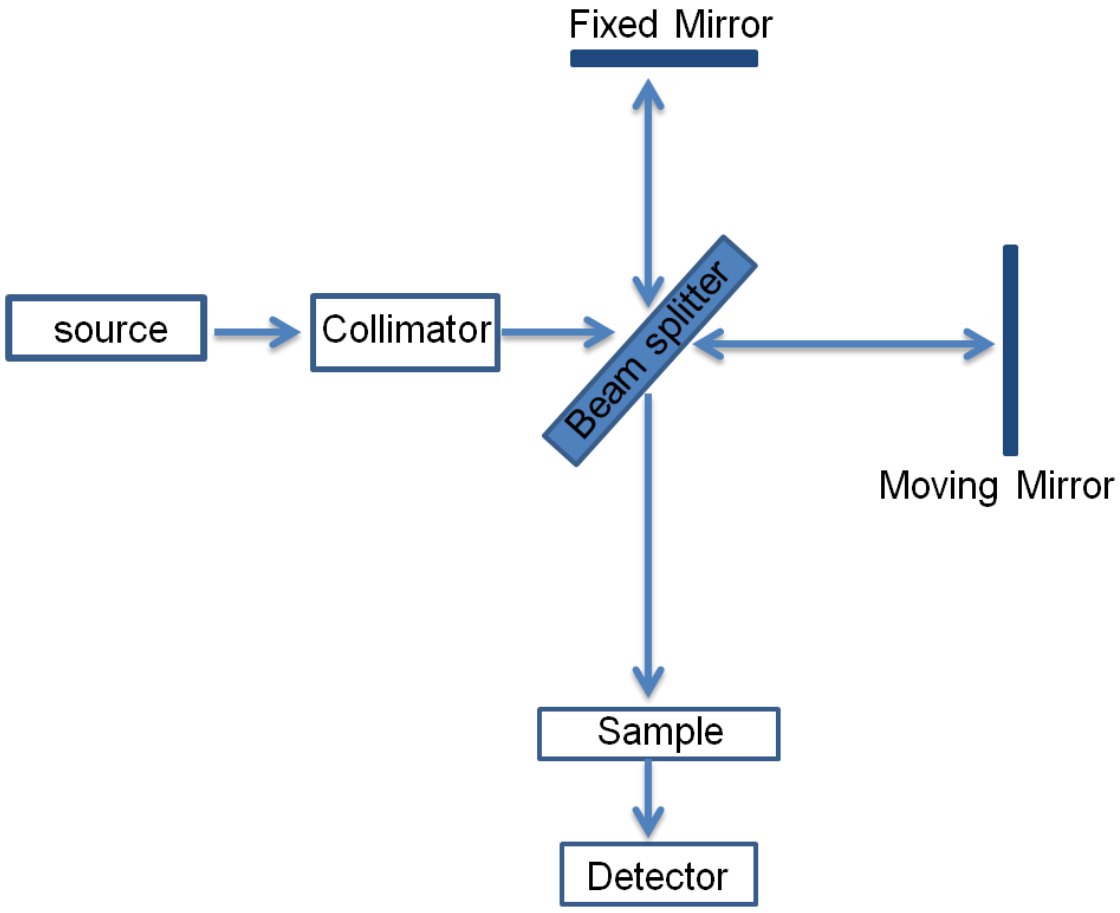

Figure 2-4. Block diagram of an FTIR spectrometer instrument.

A combination of IR spectroscopy with optical microscopy (FTIRM) makes this technique more versatile. This new technique yields microscopic detail together with chemical information. Using synchrotron light source with tunable high photon flux makes this technique makes it even more powerful. The high brilliance (i.e., flux density) of light allows measuring a sample with a spatial resolution (3-10 μm) and higher signal intensity than any globar source.[14] Using this synchrotron based IR spectromicroscopy one can detect very thin films (sub-monolayer – monolayer coverage) of organic molecules with higher signal to noise ratio.

2.3 ULTRAVIOLET (UV) -VISIBLE SPECTROSCOPY

Ultraviolet (UV) and visible spectroscopy deal with the light that occupies a narrow part of the total electromagnetic radiation spectrum. The UV light lies in the wavelength range 200-400 nm and visible light in the wavelength range 400– 800 nm.[15] When the light hits the sample molecules or atoms, the molecules absorb the energy from the UV or visible light causing an electronic transition in the molecule.[15] The amount of light absorbed in the process is the difference between the intensity of the incident ($I_\circ$) and transmitted light (I). UV and visible spectroscopy are also governed by the Bouguer Lambert-Beer law described in Section 2.2.[15] UV and visible spectroscopy can be used to quantitatively determine the concentration of species in a solution as well as the HOMO-LUMO gap and electronic structure of the molecules.[16]

The basic parts of a spectrophotometer to study absorbance are a light source, a monochromator, a sample holder and a detector. A commonly used light source for the UV

region is a deuterium lamp, and for the visible region is a tungsten lamp (tungsten- halogen). Prisms or gratings are commonly used as monochromators, which split up light into constituent wavelengths. Photomultipliers are most common as detectors.

In a typical spectrometer, a beam of light from a visible and/or UV light source is passed through the sample in the cuvette. The passed wavelength of the light will be scanned for ~ 30 sec across the ultraviolet and visible region. A beam with the same intensity and frequency will also pass through a reference solvent. The detector will then measure and compare the intensities of the two light beams.[15]

2.4 ATOMIC FORCE MICROSCOPY (AFM)

An atomic force microscope (AFM) is a 3D surface profiler which can give qualitative and quantitative surface information with sub-nanometer resolution. To construct a 3D image of an object it uses inter-atomic forces between the probe tip and the sample.[17] When the probe tip approaches closer to the surface during scanning the surface, forces (attractive or repulsive) between the surface and the probe tip cause deflection of the cantilever. [18]

Depending on the nature of the forces an AFM can function in one of three different imaging modes. One of the modes is the contact mode which is also known as static mode, the other two modes (non-contact and tapping) are known as dynamic modes (Figure 2.5). In the contact mode or static mode, the dominating force between the probe and the surface is repulsive, so it is in the repulsive regime of the inter - molecular force curve (Figure 2-5). During scanning in this mode, the probe directly touches the sample surface. The image of the surface is obtained

by maintaining a constant force (very low) and cantilever deflection by the feedback loop.[18,19] This mode is suitable for imaging rough and hard surfaces but can deform soft surfaces.[18] In the non-contact mode, the probe does not touch the sample surface but is brought within a few nanometers to the surface during scanning. In this mode, the cantilever oscillates in either amplitude mode or frequency mode in the attractive regime.[20] In this mode during the scanning of the sample surface laterally, the oscillation frequency of the cantilever deflection is kept constant by maintaining the average distance between the tip and sample by the feedback loop. By measuring the force derivative which is due to the shift in the resonant frequency of the cantilever, the topological image can be obtained in non-contact mode.[20] The non-contact mode is suitable for soft samples and the tip lifetime of the probe is better due to the low force applied on the surface. Also, the resolution is much better than contact mode, sub – atomic level resolution can be achieved by this mode. The drawback with this mode is that it requires a UHV chamber minimize contamination of the probe.[18]

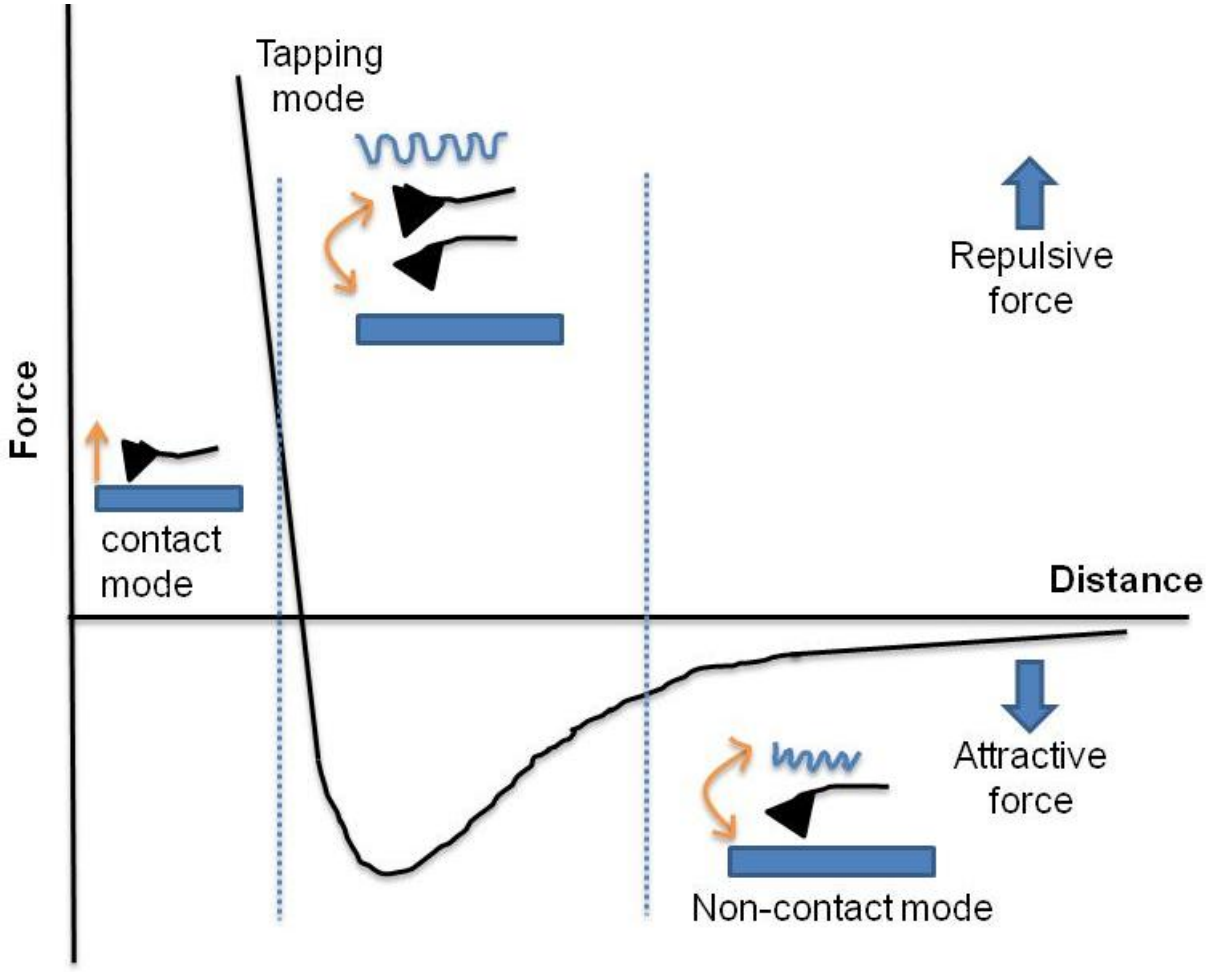

Figure 2-5. The force vs distance curve between the probe and the sample during AFM measurements.

In tapping mode or intermittent contact mode the probe oscillates up and down at its resonant frequency with a high amplitude (up to ~100 nm) while scanning the surface.[22] It operates in both on the repulsive and the attractive force regimes at the same time during scanning. In the attractive regime, it just slightly taps the surface during oscillation which prevents damaging any fragile sample.[19,21,22] In each cycle when the probe comes closer to the sample the oscillation of the cantilever decreases. By adjusting the height between the cantilever and

sample by the piezoelectric the oscillation amplitude can be kept constant. The height image of the sample can be obtained as a plot of the variation of z- position vs xy position of the probe.[21]

Figure 2.6, shows the basic components of an AFM instrument. A sharp tip commonly made out of silicon (Si) or silicon nitride (Si_3N_4) is attached to a cantilever.[19] The cantilever is connected to a piezoelectric actuator and the sample is situated on top of the piezoelectric scanner (PZT). For making the cantilever oscillate the PZT actuator applies force on the cantilever. By means of a PZT scanner, the sample can move in x, y and z-direction. During the scan, a laser beam is focused on the back of the cantilever which is reflected towards the photodetector. This reflected beam gives cantilever deflection information. By the PZT and feedback loop the constant height and constant force of the tip can be maintained. From the variation of the Z axis of the PZT scanner and the cantilever deflection information AFM topography image of a sample can be obtained.[18,21,22]

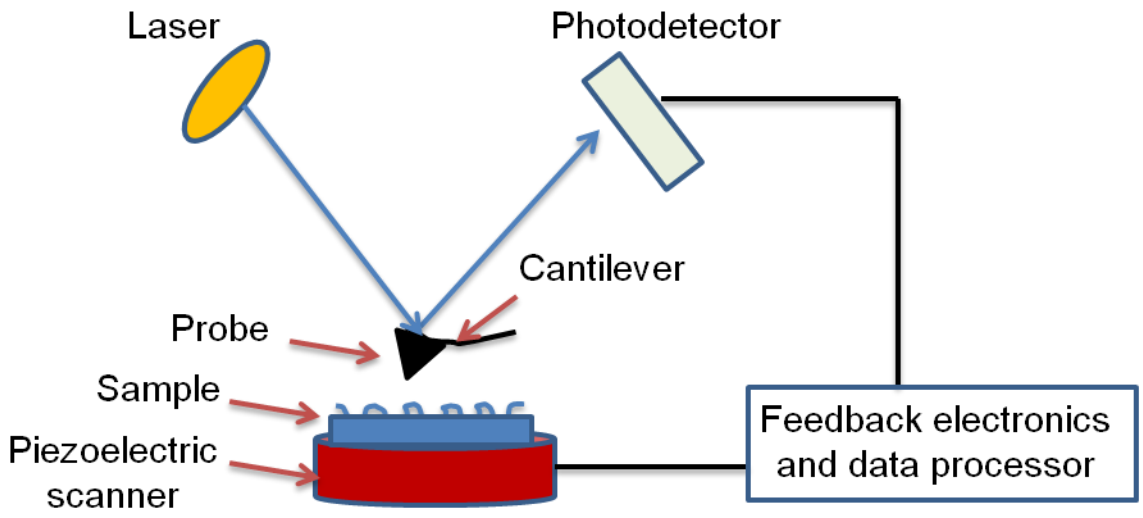

Figure 2-6. General components of an AFM instrument.

2.5 SCANNING ELECTRON MICROSCOPY (SEM)

The Scanning electron microscope (SEM) generates magnified images using a high energy electron beam instead of light. It can be used to obtain surface topography with resolutions down to ~ 1 nm.[23-25]

In SEM, the specimen is hit by an electron beam from an electron gun, which interacts with the specimen surface and results in a variety of signals. These signals are X-rays, cathodoluminescence, and three kinds of electrons: primary backscattered electrons (BSE), secondary electrons and Auger electrons.[25] These signals emerge from the different depths of the specimen surface. BSE is the elastically scattered signal and this gives useful information for imaging. The secondary electrons are emitted due to inelastic scattering and emerge from close to the specimen surface.[25] The secondary electrons can produce high-resolution images of a sample surface better than BSE. The secondary electrons are the most commonly used imaging mode.[23,25]

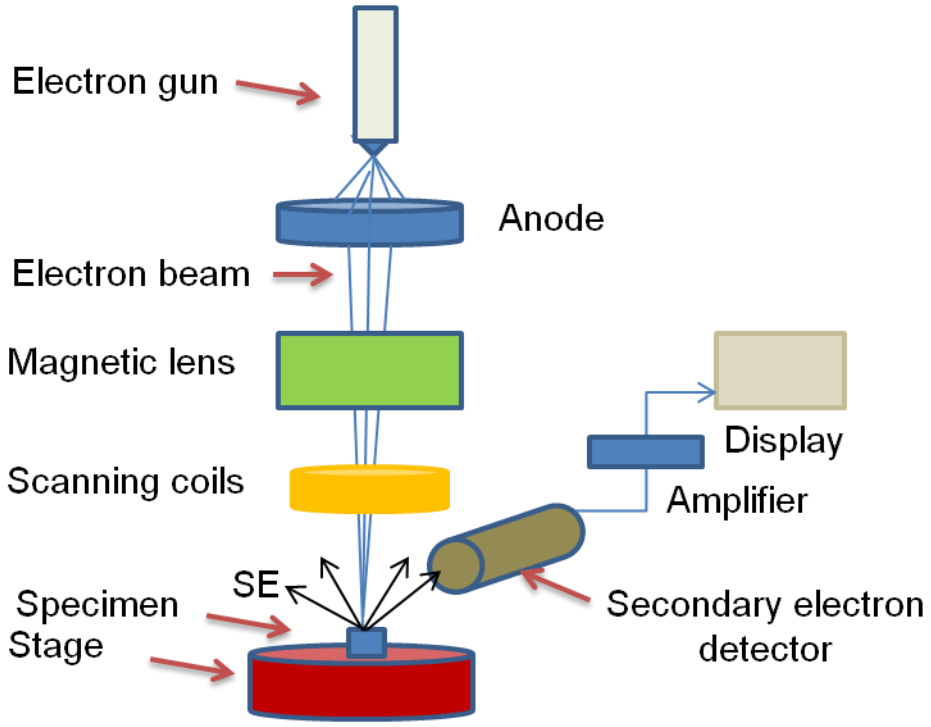

Figure 2-7. General components of a SEM instrument.

Figure 2.7 shows the instrumentation of a typical SEM. A field emission electron gun located at the top of the SEM expels electron towards the sample specimen by applying a powerful electric field. The electron beam then follows a vertical column through a series of magnetic lenses that are designed to reduce the diameter of the electron beam and focus it to a very small spot on the specimen.[22] At the bottom of the column there exist a set of scanning coils that are used to deflect the electron beam on the specimen surface in x and y-axis to scan the surface.[24] When the electron beam reaches the sample, secondary electrons are knocked out the specimen surface. These electrons are then counted by the detector.[24,25]

Some samples need special preparation before imaging in SEM. Wet samples must be fully dry because SEM utilizes a vacuum system. It also requires a conductive sample, so all non-conductive samples should be covered with a thin conductive layer.[23,24]

2.6 THERMAL GRAVIMETRIC ANALYSIS (TGA)

Thermal gravimetric analysis (TGA) is a method that measures the mass loss (or gain) of a substance as a function of temperature. In this technique, data can be plotted either directly as a mass loss (or gain) vs time or temperature or by taking the derivative of the TGA result as DTG data. DTG is a plot of change of rate of mass loss with respect to time or temperature.[26] The DTG method can be used to do a thermal analysis of molecules similar to the temperature programmed desorption (TPD) method. By using DTG as TPD, kinetic parameters such as activation energy, pre-exponential factor and order of reaction can be obtained for different organic materials.[27] TPD is a kind of technique in which the desorption of molecules is monitored while increasing the temperature linearly. At a certain temperature desorption prevails over adsorption and molecules return to the gas phase. The temperature at which desorption occurs depends on the strength of the adsorbate-surface interaction.

DTG results can be analyzed to calculate the activation energy of desorption using different methods but the Falconer-Madix method is among the most accurate.[28] In their method, they obtain the Polanyi-Wigner equation for non-negative order,[28]

$$N = -\frac{d\theta}{dt} = \nu g(\theta) \exp\left(-\frac{E}{RT_p}\right) \qquad (7)$$

Where, dθ/dt = desorption rate (molecules/cm^2.sec), ν = pre-exponential factor, g(θ) = arbitrary non-negative order expression for dependence of rate on the surface coverage and θ = surface coverage (molecule/cm^2). For dN/dt =0 at T_P equation (8) can be obtained.[28]

$$\frac{E}{RT_P^2} = \frac{\nu}{\beta}\left(\frac{dg(\theta)}{d\theta}\right)_{T_P} \exp\left(-\frac{E}{RT_P}\right) \qquad (8)$$

Taking ln on both sides of (8)

$$\ln\left(\frac{\beta}{T_P^2}\right) = \ln\left[\frac{R\nu}{E}\left(\frac{dg(\theta)}{d\theta}\right)_{T_P}\right] - \left(\frac{E}{R}\right)\left(\frac{1}{T_P}\right) \qquad (9)$$

For different heating rate plotting ln(β/T_P^2) vs (1/T) a straight with a slope (-E/R) can be obtained from where activation energy can be calculated.[28]

2.7 ELECTROCHEMICAL IMPEDANCE SPECTROSCOPY (EIS)

Electrochemical impedance spectroscopy (EIS) is a very useful method to study electrochemical systems. It has widespread applications in characterizing corrosion mechanisms, coatings, fuel cells and batteries.[29-32]

An electrochemical cell usually explores the interfacial charge transfer between a solid conductor (the working electrode) and an electrolyte. EIS is based on the AC current theory.[33] In this method a sinusoidal excitation potential (AC potential) of small amplitude is applied to the electrochemical system under investigation and in response a sinusoidal current is measured.[33] The applied excitation potential signal *E(t)* and the response current *I(t)* signal can be written as follows (Figure 2.8),

$$E(t) = E_0 \sin(\omega t) \qquad (10)$$

$$I(t) = I_0 \sin(\omega t + \theta) \qquad (11)$$

where E_0 *and* I_0 are the amplitude of the potential and current signal respectively, $\omega = 2\pi f$ is the radial frequency (radians/sec) and f the frequency (Hz) of the sine wave and θ is the phase shift between the potential and the current signal.[33,34]

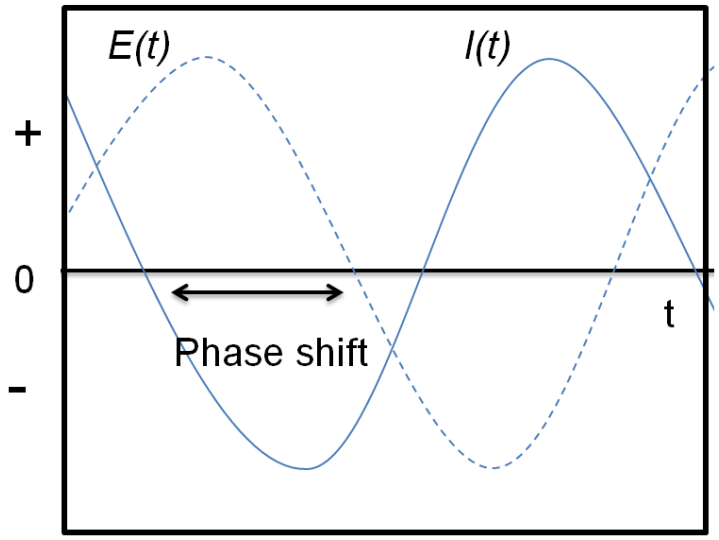

Figure 2-8. Sinusoidal potential excitation.

According to Ohm's law for AC theory where the frequency is non-zero, [33, 34]

$$Z(\omega) = \frac{E(t)}{I(t)} = \frac{E_0 \sin(\omega t)}{I_0 \sin(\omega t + \theta)} \qquad (12)$$

$Z(\omega)$ has a real Z' part and an imaginary Z'' part, $Z(\omega) = Z' + i\,Z''$ and $i = \sqrt{-1}$.

The plot of this real (x-axis) and imaginary (y-axis) components gives impedance spectra which are called complex plane or Nyquist plot ($-Z''$ vs. Z', the imaginary part is usually negative in the electrochemical systems).[35] This plot gives a semicircle on where the high-frequency intercept gives the solution resistance value and the lower frequency intercept or the

diameter of the semicircle gives the charge transfer resistance of the system (Figure 2.9). The advantage of this plot is that it gives a quick and qualitative understanding of the data. Another type of plot to represent impedance data is Bode plot [log|*Z*| and θ vs. log(*f*)] which gives more frequency information than Nyquist plot.[34,35] The logarithm of frequency axis gives wide range of frequency to be plotted. It can easily identify small impedances in the presence of large one which is difficult in Nyquist plot. Since, the Bode plot has frequency axis it is also possible to understand the frequency dependence of the impedance from this plot.

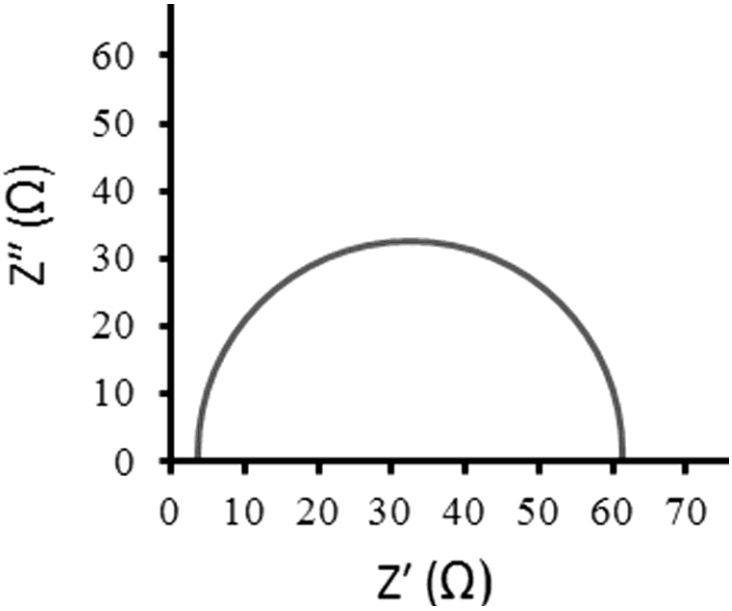

Figure 2-9. Nyquist plot for a simple electrochemical system.

2.8 OPTICAL SURFACE PROFILOMETRY (OSP)

Optical surface profilometry (OSP) is a non- contact surface measurement technique which gives surface topographic information as well as surface roughness to a very high accuracy.

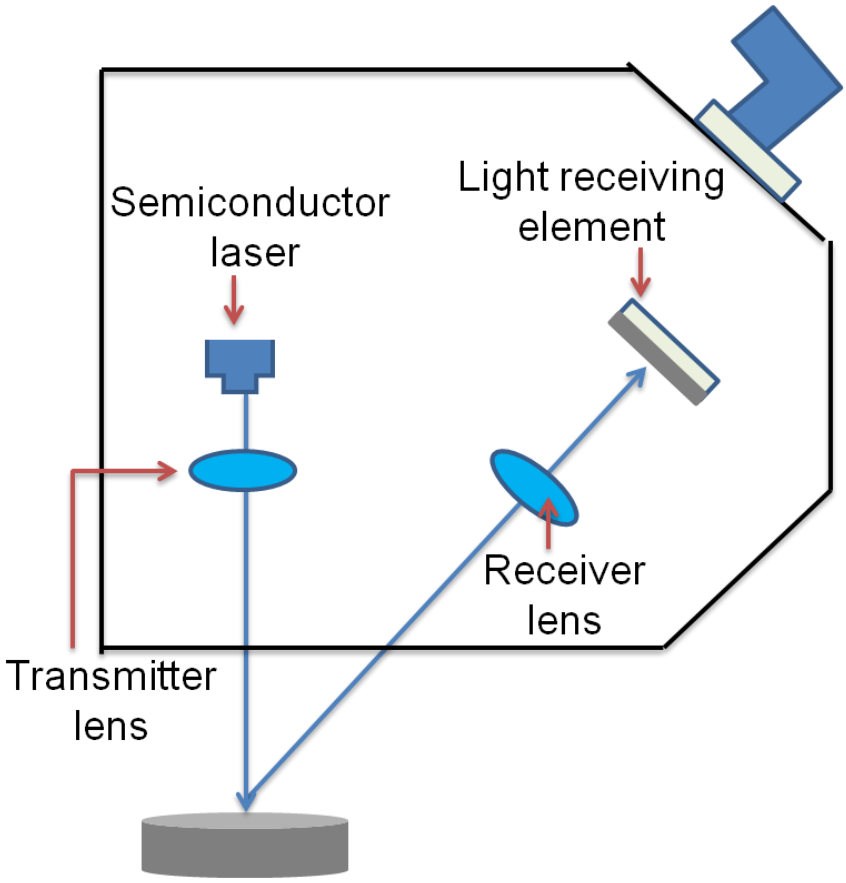

Figure 2-10. A schematic diagram of a OSP instrument.

In the OSP instrument during measurement, a small spot (~30 µm) of laser light is pointed towards the sample surface and the scattered light is focused onto the CCD displacement sensor which is attached to the scanning head of the system.[36] By measuring the displacement of the scattered light, surface topographic features are generated. During the measurement, a constant distance between the probe and the sample is maintained. This is technique has various applications such as coating thickness, smoothness, and damage analysis of the corroded sample.[36]

2.9 REFERENCES

(1) Schrader, B. Infrared and Raman Spectroscopy: Methods and Applications; *John Wiley & Sons,* **2008**.

(2) Bumbrah, G. S.; Sharma, R. M. Raman Spectroscopy Basic Principle, Instrumentation and Selected Applications for the Characterization of Drugs of Abuse. *Egypt. J. Forensic Sci*. 10.1016/j.ejfs.**2015**.06.001.

(3) Ferraro, J. R. Introductory Raman Spectroscopy; *Academic Press,* **2003**.

(4) Larkin, P. Infrared and Raman Spectroscopy: Principles and Spectral Interpretation; *Elsevier*, **2011**.

(5) Sharma, D. B. K. Instrumental Methods of Chemical Analysis; *Krishna Prakashan Media*, **2000**.

(6) Singh, R. C. V. Raman and the Discovery of the Raman Effect. *Phys. Perspect. PIP* **2002**, 4 (4), 399–420.

(7) Butler, H. J.; Ashton, L.; Bird, B.; Cinque, G.; Curtis, K.; Dorney, J.; Esmonde-White, K.; Fullwood, N. J.; Gardner, B.; Martin-Hirsch, P. L.; et al. Using Raman Spectroscopy to Characterize Biological Materials. *Nat. Protoc*. **2016**, 11 (4), 664–687.

(8) Chalmers, J. M.; Edwards, H. G. M.; Hargreaves, M. D. Infrared and Raman Spectroscopy in Forensic Science; John Wiley & Sons, **2012**.

(9) Stuart, B. Infrared Spectroscopy. In Kirk-Othmer Encyclopedia of Chemical Technology; *John Wiley & Sons, Inc*., **2000**.

(10) Smith, B. C. Fundamentals of Fourier Transform Infrared Spectroscopy, Second Edition; *CRC Press,* **2011**.

(11) Derrick, M. R.; Stulik, D.; Landry, J. M. *Infrared Spectroscopy in Conservation Science*; **1999**..

(12) Stuart, B. H. Infrared Spectroscopy: Fundamentals and Applications; *John Wiley & Sons*, **2004**.

(13) Griffiths, P. R.; Haseth, J. A. D. Fourier Transform Infrared Spectrometry; *John Wiley & Sons*, **2007**.

(14) Holman, H.-Y. N.; Bjornstad, K. A.; McNamara, M. P.; Martin, M. C.; McKinney, W. R.; Blakely, E. A. Synchrotron Infrared Spectromicroscopy as a Novel Bioanalytical Microprobe for Individual Living Cells: Cytotoxicity Considerations. J. Biomed. Opt. **2002**, *7* (3), 417–424.

(15) Perkampus, H.-H. UV-VIS Spectroscopy and Its Applications; *Springer Science & Business Media*, **2013**.

(16) Owen, T. Fundamentals of UV-Visible Spectroscopy; *Hewlett-Packard*, **1996**.

(17) Binnig, G.; Quate, C. F.; Gerber, C. Atomic Force Microscope. *Phys. Rev. Lett.* **1986**, 56 (9), 930–933.

(18) Oliveira, R. R. L. D.; Albuquerque, D. A. C.; Cruz, T. G. S.; Yamaji, F. M.; Leite, F. L. Measurement of the Nanoscale Roughness by Atomic Force Microscopy: Basic Principles and Applications, *InTech* **, 2012.**

(19) Blanchard, C. R. Atomic Force Microscopy. *Chem. Educ*. **1996**, 1 (5), 1–8.

(20) Bhushan, B.; Marti, O. Scanning Probe Microscopy- Principle of Operation, Instrumentation, and Probes. In Springer Handbook of Nanotechnology; Bhushan, P. B., Ed.*; Springer Berlin Heidelberg*, **2010**; pp 573–617.

(21) Mourougou-Candoni, N. Tapping Mode AFM Imaging for Functionalized Surfaces. In Atomic Force Microscopy Investigations into Biology - From Cell to Protein; Frewin, C., *Ed.; InTech,* **2012**.

(22) Leite, F. L.; Mattoso, L. H. C.; Oliveira, O. N.; Herrmann, P. S. P. The Atomic Force Spectroscopy as a Tool to Investigate Surface Forces: Basic Principles and Applications; Formayex, **2007**.

(23) Goldstein, J.; Newbury, D. E.; Echlin, P.; Joy, D. C.; Jr, A. D. R.; Lyman, C. E.; Fiori, C.; Lifshin, E. Scanning Electron Microscopy and X-Ray Microanalysis: A Text for Biologists, Materials Scientists, and Geologists; *Springer Science & Business Media*, **2012**.

(24) Zhou, W.; Apkarian, R.; Wang, Z. L.; Joy, D. Fundamentals of Scanning Electron Microscopy (SEM). In Scanning Microscopy for Nanotechnology; Zhou, W., Wang, Z. L., Eds.; *Springer New York*, **2006**; pp 1–40.

(25) Mehta, R. Interactions, Imaging and Spectra in SEM. In Scanning Electron Microscopy; Kazmiruk, V., *Ed.; InTech*, **2012**.

(26) Dunn, J. g. Thermogravimetric Analysis. In Characterization of Materials; *John Wiley & Sons, Inc.*, **2002**.

(27) El-Sayed, S. A.; Mostafa, M. E. Pyrolysis Characteristics and Kinetic Parameters Determination of Biomass Fuel Powders by Differential Thermal Gravimetric Analysis (TGA/DTG). *Energy Convers. Manag*. **2014**, 85, 165–172.

(28) Falconer, J. L.; Madix, R. J. Flash Desorption Activation Energies: DCOOH Decomposition and CO Desorption from Ni (110). Surf. Sci. **1975**, 48 (2), 393–405.

(29) Mansfeld, F. Use of Electrochemical Impedance Spectroscopy for the Study of Corrosion Protection by Polymer Coatings. *J. Appl. Electrochem.* **1995**, *25* (3), 187–202.

(30) Thenmozhi, G.; Arockiasamy, P.; Mohanraj, G.; R, J. S. Evaluation of Corrosion Inhibition of Mild Steel: Chemically Polymerized PpAP/ Al2O3 Composite in the Presence of Anionic Surfactants. *Port. Electrochimica Acta* **2014**, *32* (5), 417–429.

(31) He, Z.; Mansfeld, F. Exploring the Use of Electrochemical Impedance Spectroscopy (EIS) in Microbial Fuel Cell Studies. *Energy Environ. Sci.* **2009**, *2* (2), 215–219.

(32) Hjelm, A.-K.; Lindbergh, G. Experimental and Theoretical Analysis of LiMn2O4 Cathodes for Use in Rechargeable Lithium Batteries by Electrochemical Impedance Spectroscopy (EIS). *Electrochimica Acta* **2002**, *47* (11), 1747–1759.

(33) Perez, N. *Electrochemistry and Corrosion Science*; Springer Science & Business Media, **2004**.

(34) Zhang, X. (Sarah). Kinetics of O2 Reduction on Oxide- Covered Ni-Cr-Mo Alloys, The University of Western Ontario, **2012**.

(35) Lasia, A. Electrochemical Impedance Spectroscopy and Its Applications; Springer New York: New York, NY, **2014**.

(36) Scanning probe electrochemistry with high resolution and high modularity [Brochure]. (n.d.) CLAIX, France: Bio-Logic SAS.

CHAPTER -3
NATURE OF THE INTERACTION OF N,N'-DIPHENYL-1,4-PHENYLENEDIAMINE WITH IRON OXIDE SURFACES.

Tanzina Chowdhury, Enamul Hoque, Amirmasoud Mohtasebi and Peter Kruse[*]

Department of Chemistry and Chemical Biology, McMaster University, 1280 Main Street West, Hamilton, Ontario L8S 4M1, Canada.

ABSTRACT: Redox-active polymers and small molecules are of great interest in coatings, such as corrosion inhibitors for steel and other metals. In this work the interaction of the redox-active phenyl-capped aniline dimer (N,N'-Diphenyl-1,4-phenylenediamine, DPPD) with iron oxide surfaces was investigated with the aim to understand the corrosion inhibition and self-healing properties of polyaniline and aniline oligomers on iron oxide surfaces. Raman, mid-IR, and visible spectroscopy all show that reduced DPPD transforms into the semiquinone form by interacting with α-Fe_2O_3. Thermal gravimetric analysis (TGA) was used to quantify the strength of these interactions, clearly within the chemisorption range. TGA analysis, mid-IR spectroscopy and atomic force microscopy showed the DPPD molecules to be standing on their edge on the surface and changing their orientation to standing on end upon initiation of multilayer formation. DPPD – and hence other reduced oligoanilines or polyaniline – are therefore shown to strongly interact with iron oxide surfaces through hydrogen bonding and charge transfer to the surface. A full understanding of coatings will ultimately require the study

of all oxidation states and their surface interactions. Here we provide the most detailed understanding to date of the reduced state as a first step.

* To whom correspondence should be addressed. Email: pkruse@mcmaster.ca. Phone: +1 (905) 525-9140 ext. 23480. Fax: +1 (905) 522-2509

3.1 INTRODUCTION

An atomic-level understanding of the interactions of organic molecular films with inorganic oxides is of importance due to their applications in electronic devices, catalysis, and protective coatings. The rapid development of technologies such as organic light-emitting diodes,[1-2] organic thin film transistors,[3] organic solar cells,[4-6] water splitting[7] and smart coatings[8,9] requires efforts in interfacial engineering between organic thin films and inorganic metal oxides. Conducting polymers such as polyaniline (PANI) are one of the most prominent examples in the coating industry, with a proven ability to inhibit corrosion of iron and steel.[10]

Iron oxides and iron oxide surface chemistry, are widely studied for their photocatalytic properties, magnetic properties, and also in the area of corrosion.[11-13] When exposed to oxygen and water in ambient conditions, iron forms native oxides, which are believed to be composed of a partially oxidized inner layer (FeO and Fe_3O_4) and fully oxidized outer layer (Fe_2O_3, FeO(OH)).[13] This natively grown outer layer is neither passive nor mechanically stable. In order to prevent further oxidation of the metal surface, a sufficiently anodic potential needs to be applied to passivate the iron oxide surface.[11] In 1985 DeBerry[14] found that corrosion of iron or steel can be inhibited through the use of polyaniline (PANI) as a protective coating additive.[15]

More recently it has been found that PANI coatings can break down catastrophically due to their conductivity and long range interactions, which is the reason why their commercialization has failed.[16] There are some challenges to using long chain polymers such as poor solubility in benign solvents and the impossibility of using vacuum deposition to get well defined organic thin films.[17] These issues are not shared by short-chain aniline oligomers. Here we focus on the phenyl-capped dimer, which is the shortest redox active oligomer of polyaniline, and a simplified model of this class of corrosion inhibitors. This dimer has two oxidation states; a fully reduced form which is N,N'-Diphenyl-1,4-phenylenediamine (DPPD) and a fully oxidized phenyl terminated dimer or N,N'-Diphenyl-1,4-benzoquinonediimine (B2Q1). These molecules have fewer redox states than PANI because they have only two nitrogen atoms in the molecular chain, whereas at least four nitrogen atoms are needed to fully mimic polyaniline. For a detailed understanding of the interactions of PANI with iron oxide surfaces, investigation of these molecules is nevertheless an important first step. Previous work in our group showed evidence of electronic interactions between the leucoemeraldine (reduced) forms of the phenyl-capped aniline tetramer with native iron oxide surfaces.[18]

In this study, the nature of the interactions of DPPD with hematite (α-Fe_2O_3) and native oxide surfaces was investigated using Raman, Mid-IR, and visible spectroscopy. The strength of these interactions was quantified using thermo-gravimetric analysis (TGA). Polarized IR spectromicroscopy and atomic force microscopy (AFM) are used to determine the orientation of DPPD in the bulk of deposited films and directly at the oxide surface. The aim of this work is to step by step understand the interaction of aniline oligomers with iron oxide surfaces to reveal the corrosion inhibition mechanism of polyaniline and its oligomers.

3.2 EXPERIMENTAL DETAILS

The steel coupons (1 cm × 1 cm) used in this work were mechanically cut from sheets of low carbon steel (~0.002 weight% C, ~0.5 weight% Mn, balance α-Fe) obtained from ArcelorMittal Dofasco. Those coupons were mechanically polished for a minimum of 20 minutes by using coarse grit silicon carbide emery paper, followed by using 3 μm and 1 μm diamond particle emulsions combined with lubricating solution and colloidal silica (0.05 μm). All the samples were then washed with water and sonicated with acetone and methanol. The iron(III)oxide (α-Fe_2O_3) nanopowder (<50 nm particle size, surface area 16 mg/m^2), DPPD powder (98%), and the reducing agent ascorbic acid (reagent grade) were purchased from Sigma-Aldrich. Reduced DPPD powder was made by first mixing DPPD with ascorbic acid in a DPPD: the ascorbic acid molar ratio of 1:1.36. The mixture was then dissolved in methanol and stirred for 24 hours. Millipore grade water was used to dilute the methanolic solution, and the resulting precipitate was washed under vacuum suction with copious amounts of Millipore water to remove any residual ascorbic acid. The product was then dried in a desiccator. Ammonium persulfate (Sigma Aldrich, reagent grade) was used to obtain the oxidized form of the phenyl-capped dimer B2Q1), with a DPPD to ammonium persulfate molar ratio of 1 : 0.88, following otherwise the same procedure as for making the reduced form.

UV-Vis spectra were recorded using an Ultrospec-100pro spectrophotometer. DPPD and B2Q1 powders were initially dissolved in MeOH to about 1 mg/ml. For taking spectra the solutions were diluted until an acceptable absorptivity range of the spectra was achieved. Samples containing α-Fe_2O_3 powder were suspended by sonication in methanol and also diluted as required.

Raman spectra were obtained with a green laser excitation line (λ = 514.5 nm) on a Renshaw In Via Raman microscope. The objective used is a 20x lens, resulting in a spot size of ca. 1 μm. The maximum laser power that was used for DPPD was 0.07 mW to 0.1 mW at the sample. For ease of comparison, the Raman spectra presented in this work were normalized to the highest peak.

DPPD was vacuum deposited on steel coupons via thermal evaporation from a tantalum crucible. The home built stainless steel vacuum deposition chamber was pumped oil-free to a base pressure of about 3×10^{-6} Torr. The sample was mounted on a sample holder that could be cooled to less than 280 K and heated to above 600 K. The deposition coverage was measured using a quartz crystal microbalance. The substrate temperatures during deposition were 40 ˚C and 10 ˚C and the thickness of the films deposited was 1.6 nm and 5 nm of reduced DPPD, respectively. These two samples were studied by atomic force microscopy (AFM) for step height analysis. Another sample with a 15 nm thick film of DPPD was also deposited on one-half of a steel coupon using a tantalum shadow mask. The substrate temperature of this sample was ~12.5 ˚C. This sample was observed by IR spectromicroscopy at the mid-IR beamline at the Canadian Light Source, in Saskatoon, SK. The endstation used for the experiment is a Bruker Vertex 70v/S spectrometer with a Hyperion 3000 microscope. This endstation is equipped with both a 100-micron size single element MCT detector (Globar and beamline sources) and a 64x64 pixel focal plane array detector (beamline only). For observing the thin layer of DPPD on steel surface a grazing incidence of reflection (GIR) objective was used.

Thermal gravimetric analysis was performed using a Netzsch STA-409 'Luxx', which is a simultaneous thermal gravimetric analyzer (TGA) and a differential thermal analyzer (DTA).

Each coverage (powder mixture of DPPD and α-Fe_2O_3) was run for different heating rates at 2, 5, 10, 15 and 20 deg/min with a final temperature of 1200 ˚C. In TGA the samples were run in air using standard Al_2O_3 crucibles. The data was analyzed taking the derivative of the TGA (derivative thermogravimetric – DTG) curve. From the DTG analysis, the desorption energies for 0.14, 0.18, 0.19, 0.4, 0.49, 0.52, 0.54, 0.81 and 1.08 nm films of DPPD on α-Fe_2O_3 sample were analyzed using the Falconer and Madix method.[19,20] The average thickness of the molecular films was calculated using the volume and area of these molecules (unit cell dimensions of DPPD from XRD data are a = 2.5701 nm, b = 0.7482 nm, and c = 0.6967 nm).[21] The desorbed species were verified by using a Varian CP-3800 Gas chromatograph with a Varian 2200 ion trap mass selective detector over a temperature range 50-450˚C.

AFM was performed in a Veeco Enviroscope with a Nanoscope IIIa controller and Veeco RTESPA (Tapping Mode, resonance frequency nominally 300 kHz) phosphorus n-doped Si tips with nominal radii of 10 nm or less. Gwyddion data analysis software version 2.44 was used to analyze the AFM data.[22] Another kind of sample was made by drop casting reduced DPPD in methanolic solution on steel substrates. DPPD powder was dissolved in MeOH to 1mg/ml. During drop casting, MeOH was evaporated in air. Raman spectra were also taken for these samples to characterize the interaction of reduced DPPD with α-Fe_2O_3. SEM imaging was done using a JEOL-7000F at 3 kV beam energy, 6 mm sample distance in secondary electron detection mode at a base pressure of 5×10^{-5} Torr.

3.3 RESULTS AND DISCUSSION

Spectroscopic investigation of the interactions of different forms of DPPD with α-Fe_2O_3.

The interactions of different forms of DPPD with α-Fe_2O_3 were initially characterized using visible spectroscopy which can clearly distinguish between different oxidation states present in different samples. Figure 3.1 shows visible spectra of N,N'-diphenyl-p-phenylenediamine (DPPD) powder as purchased, N,N'-Diphenyl-1,4 benzoquinonediimine (B2Q1) powder, a ~0.19 nm film of DPPD on α-Fe_2O_3 (nanopowder), a ~0.28 nm film of B2Q1 on α-Fe_2O_3, and a ~0.54 nm film of DPPD on α-Fe_2O_3. The visible spectrum of the DPPD as purchased (Figure 3.1a) has a peak at 343 nm which corresponds to the π-π* transition in the benzenoid ring of the reduced DPPD[23,24] as well as a little feature at ~379 nm due to a small population of the semiquinone form. This indicates that as purchased the DPPD powder is mostly in the reduced (leucoemeraldine) form and includes traces of the semiquinone form. The visible spectrum of B2Q1 (Figure 3.1b) shows an absorption peak at ~361 nm due to the presence of the semiquinone form[23-25] and at ~531 nm due to the transition of the benzenoid ring to a fully oxidized quinoid ring.[26] In the visible spectra of a ~0.54 nm film DPPD film, the characteristic band of the π-π* transition is blue shifted to 337 nm (Figure 3.1d) and it is blue shifted to an even lower wavelength for a ~0.19 nm film of DPPD (Figure 3.1e). Both of these spectra show a trace of the peak assigned to the semiquinone form at ~367 nm (~0.54 nm film) and ~364 nm (~0.19 nm film), respectively. These two peaks (367 nm and 364 nm) arise from the interaction of the semiquinone ring of the DPPD with α-Fe_2O_3. There is no sign of B2Q1 (the peak from 500 - 800 nm) in these two spectra. Figure 3.1f shows a spectrum of the pure α-Fe_2O_3 powder for comparison, indicating that all discussed features indeed originate from the molecules. The

531 nm peak of B2Q1 is hardly visible in the spectrum of a ~0.28 nm film of B2Q1 on α-Fe_2O_3 (Figure 3.1c), indicating that upon interaction with α-Fe_2O_3 the B2Q1 transforms mostly into the semiquinone form.

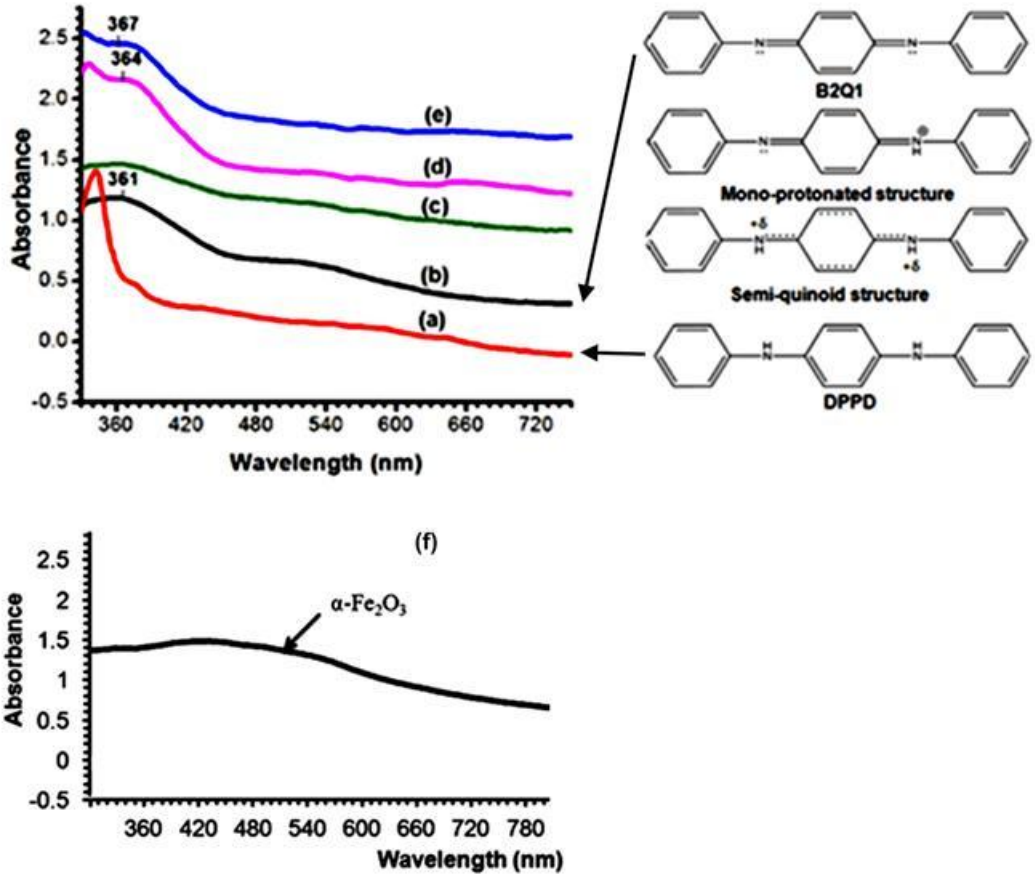

Figure 3-1. Visible spectra of (a) DPPD as purchased; (b) B2Q1 as prepared; (c) ~0.28 nm film of B2Q1 on α-Fe_2O_3; (d) ~0.54 nm film of DPPD on α-Fe_2O_3; (e) ~0.19 nm film of DPPD on α-Fe_2O_3; and (f) pure α-Fe_2O_3 powder for comparison.

Raman spectroscopy was also used to characterize the species that arise due to the interaction of DPPD with iron (III) oxides and identify if any change of oxidation states of DPPD during deposition is due to interaction with iron oxide, or due to interaction with methanol which was

used as a solvent. DPPD powder (fully reduced), shows intense Raman bands at 745, 816, 993, 1029, 1194, and 1616 cm^{-1} (Figure 3.2a). The bands at 1194 and 1616 cm^{-1} were attributed to C-C stretching and C-H bending vibration respectively,[27] and the bands at 993 and 1029 cm^{-1} arise due to ring breathing of the monosubstituted benzene.[28] The bands at 745 and 816 cm^{-1} are assigned to C-H out-of-plane wag of mono-substituted benzene.[29] For comparison, the Raman spectrum of as purchased DPPD powder was also taken (see Supporting Information 3.11) which shows the presence of some semiquinone species in purchased DPPD as indicated by the visible spectrum. The Raman spectrum of DPPD drop cast from methanol onto glass shows no sign of interaction (Figure 3.2b). This spectrum shows similar bands to the powder DPPD spectrum in Figure 3.2a.

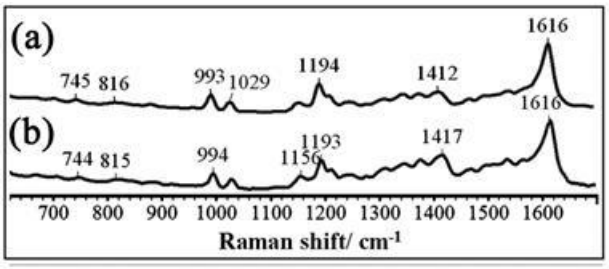

Figure 3-2. Raman spectra of (a) pure powder DPPD (b) DPPD dropcast onto glass from methanol.

To observe the interaction of DPPD with α-Fe_2O_3 nanopowder, Raman spectra are taken for different coverages of DPPD on α-Fe_2O_3 nanopowder, namely of ~0.54 nm and ~0.19 nm films of DPPD powder mixed with α-Fe_2O_3 nanopowder (Figure 3.3). The main characteristic peaks of DPPD, 1615, 1193, 1029 and 993 cm^{-1} (Figure 3.2a) are not present in those spectra, and instead, new bands arise. In Figure 3.3a the Raman band at 1398 cm^{-1} is assigned to the radical

cation or semiquinone forms of DPPD.[30,31] The bands at 1340 cm^{-1} (shifted) and 1231 cm^{-1} are consistent with C-$N^{+\bullet}$ stretching[32,33] and the band at 1448 cm^{-1} (shifted) is due to C-C stretching[30] of the semiquinone radical. In Figure 3.3b of the ~0.54 nm film, the intensity of the band 1448 cm^{-1} has decreased, and all the other bands are shifted to a higher wavelength. The other bands at 1152 cm^{-1} (Figure 3.3a) and 1156 cm^{-1} (Figure 3.3b) are consistent with a fully reduced powder spectrum. On the other hand, the bands at 1537 cm^{-1} (Figure 3.3a) and 1538 cm^{-1} (Figure 3.3b) belong to B2Q1 (fully oxidized dimer).[30] The band at 1631 cm^{-1} (shifted, Figure 3.3a), which is present in the thinner film (0.19 nm) is due to monoprotonated species of DPPD.[30] This indicates that DPPD transforms into mostly the semiquinone form and also to some degree into B2Q1 by interacting with α-Fe_2O_3, and also that a thin film of molecules has stronger bonding interactions with the surface than a thicker film. This phenomenon of strong bonding of the lower coverage species is also confirmed by the TGA results below.

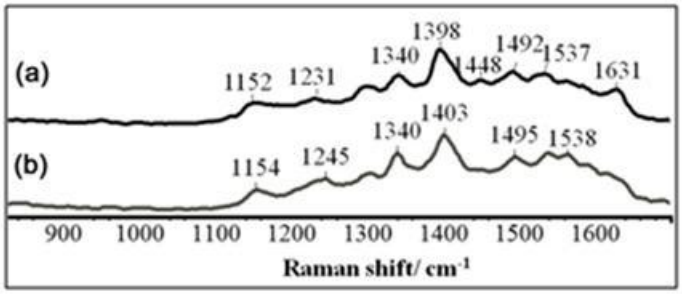

Figure 3-3. The interactions of DPPD with the α-Fe_2O_3 surface. Raman spectra of (a) ~ 0.19 nm film of DPPD and (b) ~ 0.54 nm film of DPPD on α-Fe_2O_3.

A DPPD in methanol solution was drop cast on a (1 cm × 1 cm) steel coupon, the interactions of the native oxides (the top layer consists of α-Fe_2O_3) with DPPD of this sample were then

observed by Raman spectroscopy. Figure 3.4a shows a Raman spectrum of a DPPD island with peaks at 1615, 994, 1028 and 1193 cm^{-1}, which are characteristic of pure DPPD. DPPD molecules near the interface to the native oxide of a steel substrate are converted into the fully oxidized (B2Q1) state as shown in Figure 3.4b. This result is different from the α-Fe_2O_3 and DPPD powder mixture, which showed that dry DPPD upon interaction with α-Fe_2O_3 turns into the semiquinone state. Hence methanol clearly plays a role in the interactions, likely due to hydrogen bonding.

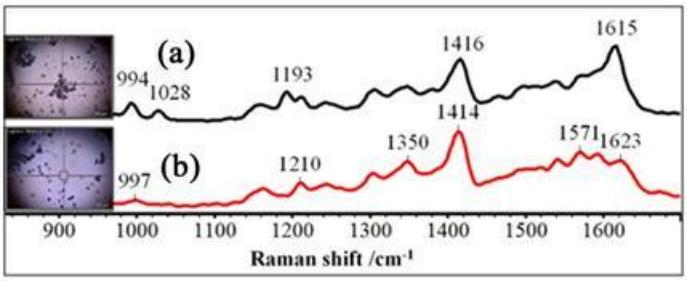

Figure 3-4. DPPD dropcast from methanol onto a steel substrate: (a) large DPPD island and (b) thin film of DPPD.

The effect of laser power in Raman spectroscopy on DPPD/α-Fe_2O_3 mixtures of different coverages was observed using a green laser (514.5 nm). The laser power used to identify the molecules on the α-Fe_2O_3 surface was 0.07 mW to 0.1 mW at the sample (Figures 3.5b, c). In the Raman spectrum at lower power (0.07 mW to 0.1 mW) it is not possible to identify the oxidation state of iron oxide in the powder mixture; if the laser power is increased to 1.04 mW at the sample it is possible to see α-Fe_2O_3 (Figure 3.5d). The Raman spectrum of a ~0.54 nm film of DPPD on α-Fe_2O_3 in Figure 3.5a shows the impact of laser power on the mixture. In the top spectrum the intensity of each band of DPPD is very low at 1.04 mW laser power (Figure

3.5a), but new bands characteristic of hematite (α-Fe_2O_3) arise at this laser power. The Raman bands at 219, 285, 398, 490 and 592 cm^{-1} are assigned to hematite (α-Fe_2O_3).[34] It is possible that at lower laser power there was magnetite (Fe_3O_4) on the surface but because of noise and higher intensity of the DPPD, it was not visible. Figure 3.5d shows the Raman spectrum of pure α-Fe_2O_3 nanopowder for comparison. This experiment shows that by Raman spectroscopy it is difficult to identify the real oxidation states of DPPD and iron oxide same time in the mixture of those two compounds, even though that would have been desirable for the study of their interactions.

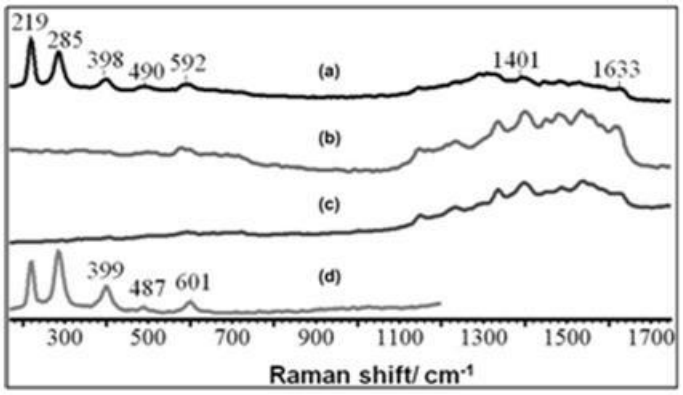

Figure 3-5. Raman spectra with 514 nm green laser of ~0.54 nm film of DPPD on α-Fe_2O_3 (powder mix). (a) At a laser power at the sample of 1.04 mW; (b) At a laser power of 0.1 mW; (c) At a laser power of 0.07 mW; (d) Pure α-Fe_2O_3 powder at a laser power of 1.04 mW at the sample.

The orientation of DPPD on a native iron oxide surface.

The orientation of DPPD on native iron oxide surfaces was studied by synchrotron-based mid-IR spectromicroscopy. A 15 nm thick film of DPPD was vacuum deposited on one-half of a steel coupon using a tantalum shadow mask. This sample had no contact with methanol. Figure 3.6 shows the IR mapping spectra of DPPD from the organic film portion of the sample towards the clean portion at $\theta_E = 90^\circ$. The location where each spectrum was taken on the sample is shown in the bottom image of Figure 3.6. In this image it can be seen that points (a) and (b) are taken on the deposited film, points (c) and (d) are taken on the edge of the film and just after the edge on the clean side, respectively and point (e) is further away from the film edge. The spectra were measured in reflection geometry with a grazing incidence ($\theta = 80^\circ$) objective. The electric field of the polarized light was parallel to the substrate surface with polarizer $\theta_E = 0^\circ$ and perpendicular to the substrate surface at $\theta_E = 90^\circ$. The IR bands of this molecule were divided into two regions, the low-frequency range < 1000 cm^{-1} (mostly out-of-plane ring vibrations) and the medium frequency range > 1000 cm^{-1} (in plane ring vibrations). From the intensity ratio between prominent bands of out-of-plane and in-plane vibration, it is possible to obtain orientation information of DPPD. In the IR mapping spectra, the bands at 1494 cm^{-1} and 1313 cm^{-1} correspond to C-H in-plane bending vibrations.[35,36] The intensity of these bands increases when moving along the film towards the film edge (as the coverage of the molecules gets lower), which corresponds to the benzenoid ring transforming into a semiquinone structure (Figures 3.6a–e).[37] As only the molecules in immediate proximity to the surface remain (lower coverage), another band arises as a shoulder at 1295 cm^{-1} (Figure 3.6e) which correspond to the C-N stretching vibration of the semiquinone ring.[37] The band at 1534

cm^{-1} (shifted) is attributed to the C-H in-plane bending vibration of the benzenoid ring. The bands at 744 cm^{-1} and 819 cm^{-1} are attributed to the C-H out-of-plane wags of mono and para-substituted benzene rings, respectively.[38]

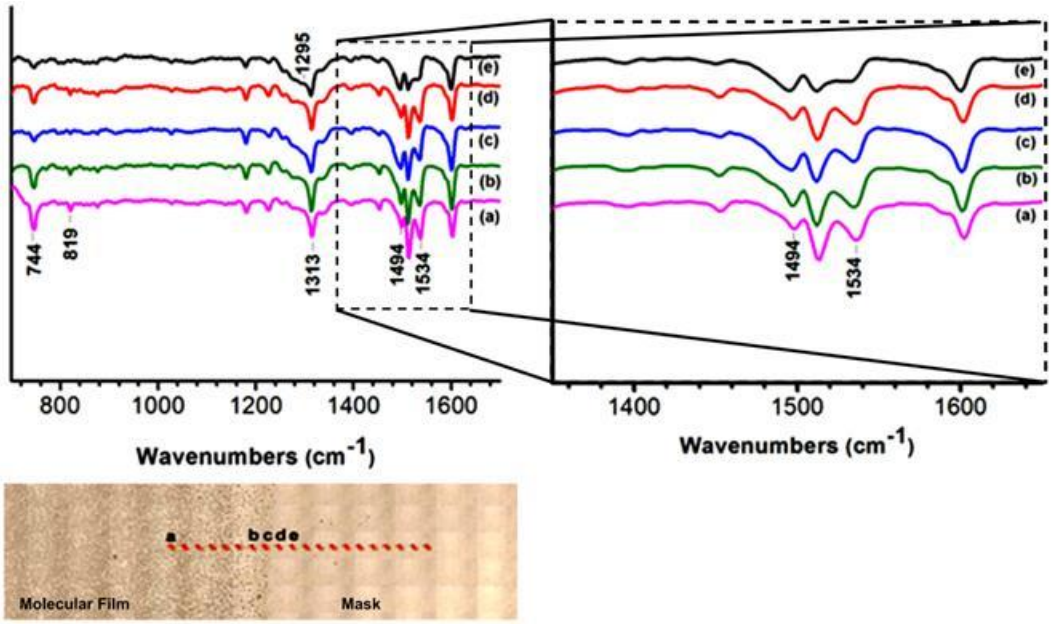

Figure 3-6. Mid-IR mapping spectra of DPPD on a steel substrate at $\theta_E = 90^\circ$. A zoom-in of the region between 1300 and 1700 cm^{-1} is shown on the right. In the IR spectra, spectra (a) – (e) represent the points from the molecular film side to the clean side. These points are shown in the optical image map at the bottom. The spacing between sample points (red marks) is 100 µm, for a total cross-section length of about 2 mm.

Table 3.1 shows the intensity ratio for $\theta_E = 90^\circ$ between the band at 744 cm^{-1} (out-of-plane wag of mono-substituted benzene) and three in-plane vibrational bands at 1534 cm^{-1}, 1494 cm^{-1} and 1313 cm^{-1} for all the points (Figures 3.6a-e). Table 2 shows the intensity ratio for $\theta_E = 90^\circ$ between the band at 819 cm^{-1} (out-of-plane wag of para-substituted benzene) and the same three

in-plane vibration bands for all the same points (Figures 3.6a-e). As the ratio decreases there is a greater chance for the molecules to be aligned with the field. It can be seen from Table 3.1 that the ratio gradually decreases as the surface coverage of the molecules is getting lower (Figures 3.6a, b, d and e), except point (c) (Figure 3.6c). Point (c) corresponds to the molecules at the edge of the deposited side. Table 3.2 shows the decrease in the intensity ratio except for a very low ratio at point (c) comparing to other two. This decrease in intensity ratio results from molecules in the first monolayer tending to lie flat on the surface (low coverage of molecules). To compare these characteristics of the DPPD molecules we took IR mapping spectra on those same points for $\theta_E = 0^\circ$ (Figures 3.7a-d).

Table 3-1: Intensity ratio between IR absorption band 744 cm^{-1} and three bands 1534, 1494, 1313 cm^{-1} for $\theta_E = 90^\circ$.

	744 cm^{-1} / 1534 cm^{-1}	744 cm^{-1} / 1494 cm^{-1}	744 cm^{-1} / 1313 cm^{-1}
1st point (a) of the mapping image.	0.76	1.1	0.78
7th point (b)	0.55	0.57	0.48
8th point (c), at the film edge	0.35	0.28	0.25
9th point (d)	0.47	0.53	0.38
10th point (e)	0.42	0.29	0.24

Table 3-2: Intensity ratio between IR absorption band 819 cm^{-1} and three bands 1534, 1494, 1313 cm^{-1} for $\theta_E = 90^\circ$.

	819 cm^{-1} / 1534 cm^{-1}	819 cm^{-1} / 1494 cm^{-1}	819 cm^{-1} / 1313 cm^{-1}
1st point (a) of the mapping image.	0.25	0.35	0.26
7th point (b)	0.23	0.24	0.20
8th point (c), at the film edge	0.12	0.10	0.09
9th point (d)	0.23	0.26	0.19
10th point (e)	0.17	0.12	0.10

Table 3.3 shows the intensity ratio for $\theta_E = 0^\circ$ between band 744 cm^{-1} (out-of-plane wag of mono-substituted benzene) with three in-plane vibration bands 1534 cm^{-1}, 1494 cm^{-1} and 1313 cm^{-1} for all the points (Figures 3.7a-d) and Table 3.4 shows the intensity ratio for $\theta_E = 0^\circ$ between band 823 cm^{-1} (shifted) (out-of-plane wag of para-substituted benzene) with the same three in-plane vibration bands for all the same points in Figures 3.7a-d. Tables 3.3 and 3.4 show the increase in intensity ratio as the coverage of molecules gets lower, except for the point (b) (Figure 3.7b), due to the same reason as mentioned above that some of the molecules are twisted or lying at an angle to the surface. This is also why the band at 823 cm^{-1} is not visible in the IR spectrum in Figure 3.7c (Table 3.4 point (c)). Comparing each of the points in Tables 3.1 & 3.3 and Tables 3.2 & 3.4 it can be seen that the intensity ratio is higher at $\theta_E = 0^\circ$ for each point. This indicates that the molecules are standing up on edge or on end on the iron oxide surface as the coverage gets lower.

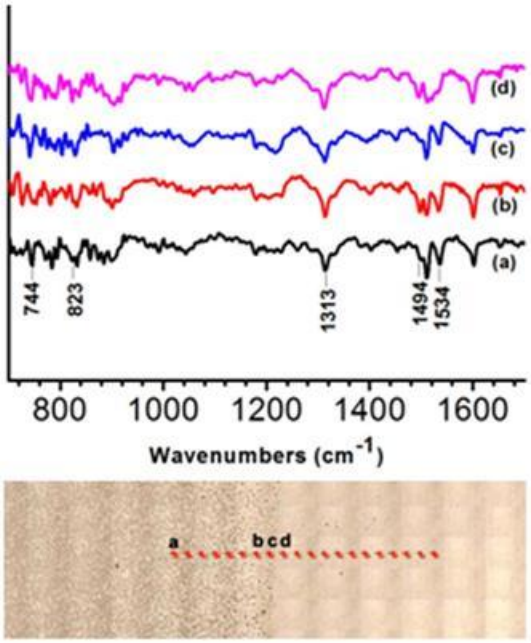

Figure 3-7. Mid-IR mapping spectra of DPPD on a steel substrate at $\theta_E = 0^\circ$. The IR spectra (a-d) represent the points from the molecular film side to the clean side. These points are shown in the optical image map at the bottom. The spacing between sample points (red marks) is 100 µm, for a total cross-section length of about 2 mm.

Table 3-3: Intensity ratio between IR absorption band 744 $cm^{-1}$and three bands 1534, 1494,1313 cm^{-1} for $\theta_E = 0^\circ$, Figure 3.6.

	744cm^{-1}/ 1534 cm^{-1}	744cm^{-1}/ 1494 cm^{-1}	744cm^{-1}/ 1313 cm^{-1}
1st point (a) of the mapping image.	1	1.3	0.82
7th point (b)	0.59	0.54	0.46
8th point, at the film edge (c)	1.8	2.5	0.82
9th point (d)	1.64	1.14	0.77

Table 3-4: Intensity ratio between IR absorption band 823 $cm^{-1}$and three bands 1534,1494, 1313 cm^{-1} for $\theta_E = 0^\circ$, Figure 3.6.

	823cm^{-1}/ 1534 cm^{-1}	823cm^{-1}/ 1494 cm^{-1}	823cm^{-1}/ 1313 cm^{-1}
1st point (a) of the mapping image.	0.9	1	0.68
7th point (b)	0.57	0.52	0.44
8th point (c), at the film edge	-	-	-
9th point (d)	1.75	1.18	0.81

Scanning electron microscopy (SEM) was used to observe the large-scale morphology of the DPPD film on the native oxide of a steel surface. Figures 3.8a and 3.8b show SEM images of oxidized DPPD on a steel substrate. This sample (steel substrate) was sonicated for ~1 hour in a solution of DPPD in methanol. Figure 3.8 shows that DPPD forms dendritic islands on the steel surface. By forming dendritic islands these molecules show their bonding attraction towards each other and also to the iron oxide surface. The spectroscopic measurements (Raman and

mid-IR) already provided evidence of the charge transfer interaction of DPPD molecules with the iron oxide surface. IR rules out the possibility of molecules lying flat on the surface, but leave open the possibilities of edge-on and end-on orientations. The question remains in which direction specifically these molecules are orientated and how strongly they are bonded to each other and with the surface.

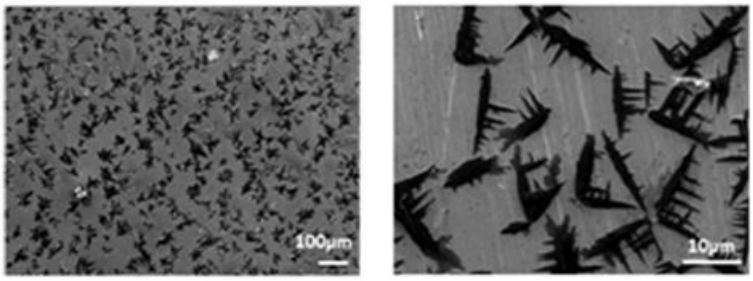

Figure 3-8. SEM images of DPPD sonicated ~1h on the steel surface. Both right and left images are showing dendritic islands of DPPD.

Step height analysis of DPPD films on α-Fe_2O_3 surfaces.

Mid-IR spectroscopy showed that DPPD molecules have preferred orientations on iron oxide surfaces. Atomic force microscopy was used as a complimentary technique to define the orientation of these molecules via layer thickness (step height). The AFM images of DPPD were analyzed to determine the thickness of the first layer formed on the surface. AFM images show that the molecules from ribbon-like islands for a 1.6 nm thick layer of molecules that was vacuum-deposited onto a substrate held at 40°C (Figure 3.9a). In contrast, the sample with a 5 nm film deposited at 10˚C substrate temperature shows islands of molecules (Figures 3.9b, c). This sample was used for step height analysis. A histogram of step heights (Figure 3.9e) was prepared from line profiles of the AFM image (Figure 3.9c). Figure 3.9d shows an example of a

line profile for the histogram. The histogram shows that most of the DPPD islands have a step height of ~0.5 nm in the first layer, with the second most probable step height being ~0.3 nm. The 0.3 nm steps are due to molecules lying flat on the surface. Due to the limited z-resolution (0.06 nm) of the AFM used in this work, it is not practical to distinguish between smaller step sizes (0.35, 0.45…etc.) which would introduce an error of ± 0.05 nm in the step calculation. The 0.5 nm step height is less than the expected thickness of about 0.7 nm for DPPD molecules standing on their edge.[21] We conclude that these molecules are standing on their edge but are tilted at an estimated angle of 45° in order to accommodate this discrepancy. Our IR results suggested that a majority of the DPPD molecules are standing either on edge or on end in the first layer but AFM rules out the on-end orientation possibility. Further confirmation of this orientation comes from thermal gravimetric analysis (TGA).

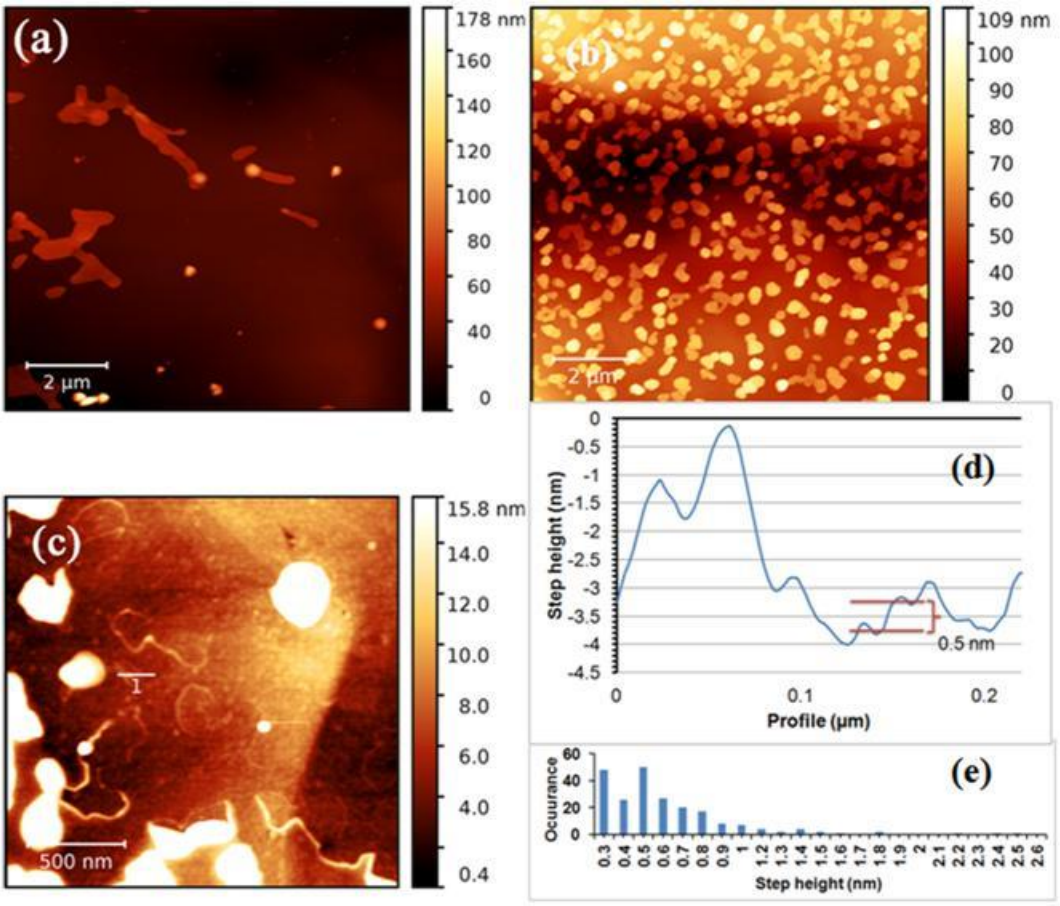

Figure 3-9. AFM height image of reduced DPPD vacuum deposited (a) at 40˚C substrate temperature (10 µm × 10 µm), (b) at 10˚C substrate temperature (10 µm × 10 µm), (c) an example of cross-section of AFM image for 10˚C substrate temperature sample (zoomed in), (d) is an example of the line profile of the AFM image (c) and (e) is the histogram of the step height from the line profiles.

Coverages and desorption energies of DPPD on Fe_2O_3 surfaces.

To complement the AFM results of orientation and to quantify the strength of the bonding between the DPPD on α-Fe_2O_3, Thermal Gravimetric Analysis (TGA) was performed for different film thicknesses of DPPD on α-Fe_2O_3 (Figure 3.10). In normal TGA analysis, the mass of the substance is monitored over time, i.e. as a function of the temperature ramp. In this work the derivative of the TGA curve was taken, known as differential thermal gravimetric analysis (DTGA). These DTGA results gave the specific temperatures for the maximum molecular desorption rates. Using the peak temperature data the desorption energy of different coverage of DPPD on iron oxide surface was calculated following the Falconer and Madix method.[20] A mass spectrometer was used to verify that DPPD molecules came of the surface intact and without decomposition at the desorption temperatures reached in DTGA (Figures S2, S3). The different film thicknesses such as, 0.14, 0.18, 0.19, 0.4, 0.49, 0.52, 0.54 ,0.81 and 1.08 nm of DPPD on α-Fe_2O_3 gave desorption energies 131, 139, 141, 161, 166, 121, 120, 136 and 155 kJ/mol, respectively for the DPPD binding with α-Fe_2O_3 as shown in Table 3.5. The film thickness was estimated using the unit cell parameters mentioned in the literature.[21] The energies correspond to the molecules being chemisorbed on the surface. The multilayer peak starts to emerge from the ~0.54 nm film and the desorption energies for multilayer peak are 106, 90 and 97 kJ/mol for the 0.54, 0.81 and 1.08 nm films, respectively.

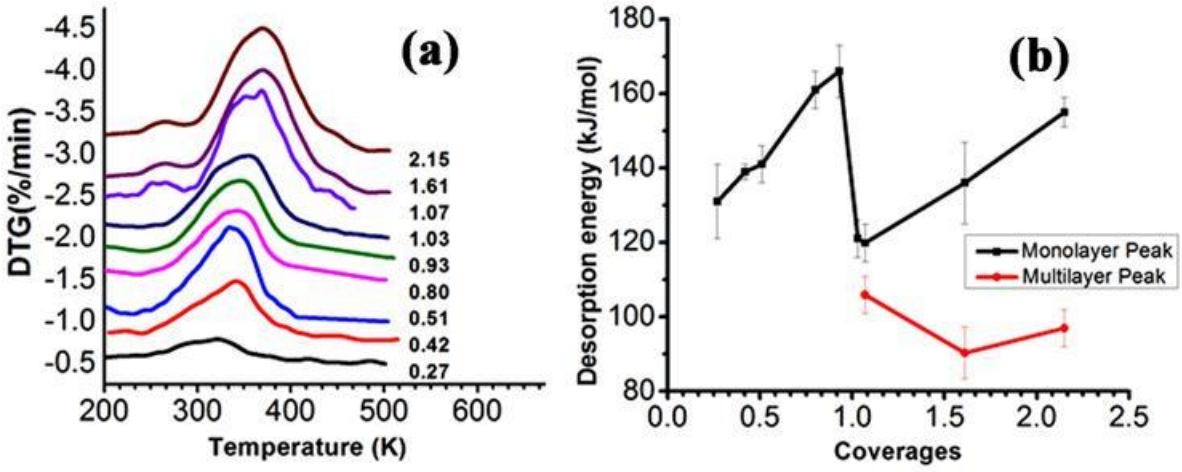

Figure 3-10. (a) DTG spectra of different coverage of DPPD on α-Fe_2O_3 (powder) mix at heating rate 20˚C/min and (b) Desorption energy *vs.* coverage, black line for monolayer peak and red line for multilayer peak.

The step height analysis of the AFM images showed that the first layer or monolayer (ML) of DPPD film has a thickness of ~0.5 nm. Assuming, from AFM data, that ~0.5 nm film thickness corresponds to 1 ML of DPPD molecules, the respective coverages for all films are listed in Table 3.5. According to this estimation, the multilayer peak starts to show its trace at 0.54 nm film (= 1.07 ML). ıf the molecules were standing on edge then the thickness of the first monolayer of molecules would be 0.7 nm.[21] Comparing the step height results of AFM image (0.5 nm) and at which coverage the multilayer peak of the DPPD molecules coming off (at 0.54 nm or 1.07 ML) it can be concluded that the DPPD molecules are standing on edge, tilted by a 45˚ angle from the surface normal.

Table 3-5: Desorption energies of DPPD.

Film thickness (nm)	coverage (ML)	desorption energy of monolayer peak (kJ/mol)	desorption energy of multilayer peak (kJ/mol)
0.14	0.27	131 ± 10	
0.18	0.42	139 ± 2	
0.19	0.51	141 ± 5	
0.4	0.80	161 ± 5	
0.49	0.93	166 ± 7	
0.52	1.03	121 ± 5	
0.54	1.07	120 ± 5	106 ± 5
0.81	1.61	136 ± 11	90 ± 7
1.08	2.15	155 ± 4	97 ± 5

The activation energy for the monolayer peak tends to increase with coverage but there is a sudden drop in energy at 1.03 ML. The validity of this result was confirmed by another experiment with similar coverage (1.07 ML). This drop in energy must be the result of a change in molecular arrangement on the surface, resulting in weaker interactions of these molecules with the iron oxide surface. It is important to note that the molecules are not splitting into several sub-populations, but rather still desorb at a uniform (but lower) energy. The emerging multilayer peak at these coverages (see last column in Table 3.5) does not represent any significant fraction of the molecules. We have established via Raman spectroscopy (Figures 3.3, 3.4) that there is charge transfer taking place between the molecular film and the iron oxide

surface. The charge transfer is facile for molecules in immediate contact with iron oxide at submonolayer coverages, but becomes more difficult to accomplish for higher coverages. The molecules could re-arrange their orientation from standing on edge to standing on end, but that would mean breaking the direct surface contact of the amino groups. The strongest interactions between the molecules and the oxide are expected to be hydrogen bonding interactions between oxygen atoms or hydroxyl groups at the oxide surface and the amino groups of the molecules. They are only accessible in the most space-consuming face-on or twisted orientations. Higher coverages force the molecules into edge-on or partially standing-up configurations, which reduce the opportunities for hydrogen bonding possibly from up to two per molecule to only one per molecule, significantly reducing the strength of surface interactions, as witnessed by the drop of desorption energy. It is remarkable that it happens uniformly and abruptly for the entire monolayer of molecules, rather than gradually. The desorption energy for the multilayer peak starts to decrease at the beginning and then becomes almost steady, shown in Figure 3.10b, due to molecules aggregating with each other rather than interacting with the α-Fe_2O_3 surface.

3.4 CONCLUSION

We have investigated the interactions of DPPD molecules with iron oxide surfaces. Raman and visible spectroscopy show that charge transfer takes place between DPPD and α-Fe_2O_3, with DPPD molecules transforming into their semiquinone form when interacting with α-Fe_2O_3. Mid-IR spectroscopy reveals that the DPPD molecules are interacting with the surface by standing either on edge or on end. AFM step height analysis points towards molecules in the first layer standing on their edge (with a minority lying face-on). DTGA analysis confirms the

AFM results and allows us to quantify the strength of the bonding interaction, which is in the chemisorption range. A chemisorbed state of DPPD on iron oxide is consistent with the charge transfer between the molecules and the surface that was observed in Raman spectroscopy. It is a result of the (hydrogen) bonding interactions of the amine groups with surface oxygen and hydroxide. The DTGA analysis shows that the chemisorption energies of these species tend to increase with coverage until a complete monolayer coverage has been achieved. From the coverage at which multilayers are first detected, we can confirm that the first layer of DPPD is standing tilted by 45° on its edge. Due to molecules re-arranging their orientation during the second layer formation the chemisorption energy drops and rise again afterward. The obtained results about the interaction and orientation of DPPD (as a representative of the reduced form or oligoanilines and polyaniline) with iron oxide surfaces are a first step towards a better understanding of the physical chemistry of oligoaniline and polyaniline interfaces with metal oxide surfaces. The specific case of iron oxide pertains to the understanding of the corrosion inhibition mechanisms of redox active aniline oligomers on steel surfaces.

Acknowledgments

We acknowledge Dr. Kirk Green from the McMaster regional mass spectrometry facility for his technical assistance and helpful discussions and also Dr. Steve Kornic (CAOS), and Frank Gibbs (BIMR) for assistance with Raman spectroscopy and thermal analysis, respectively. *Some of the research described in this paper was performed at the Canadian Light Source, which is supported by the Canada Foundation for Innovation, Natural Sciences and Engineering Research Council of Canada, the University of Saskatchewan, the Government of*

Saskatchewan, Western Economic Diversification Canada, the National Research Council Canada, and the Canadian Institutes of Health Research. We want to thank Dr. Ferenc Borondics, Dr. Scott Rosendahl, and Dr. Xia Liu at CLS for their assistance with mid-IR spectroscopy. Thanks to our group members for their kind support: Stephen Yue Wang, Alan Awez, Allen Pauric, Alexander Imbault. Financial support was provided by the National Science and Engineering Research Council of Canada through the Discovery Grant program.

Supporting information: Additional data (mass spectrometry, Raman spectroscopy, atomic force microscopy, details on thermogravimetric analysis). This material is available free of charge via the Internet at http://pubs.acs.org.

3.5 SUPPORTING INFORMATION

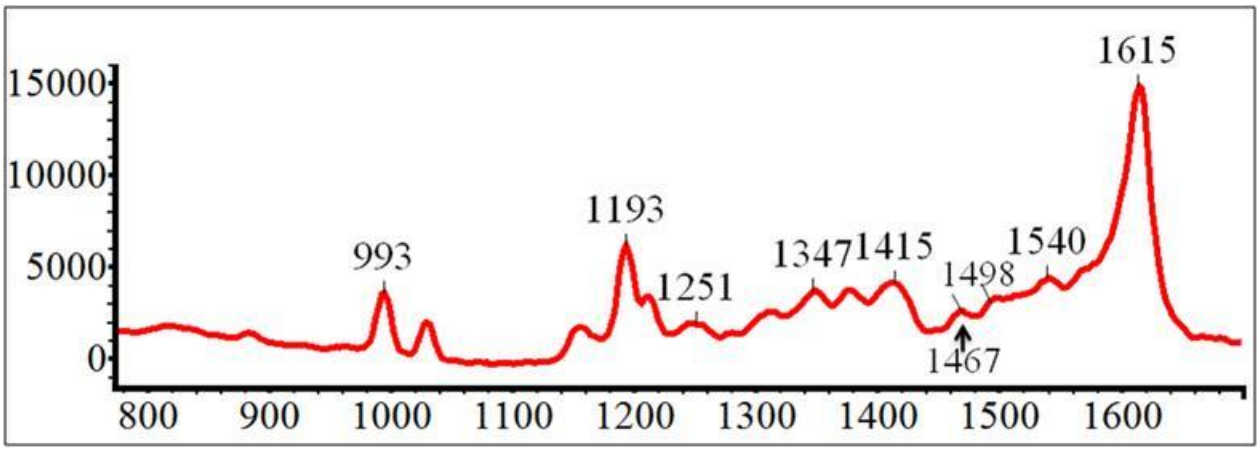

Figure 3-11. Raman spectrum of DPPD as purchased.

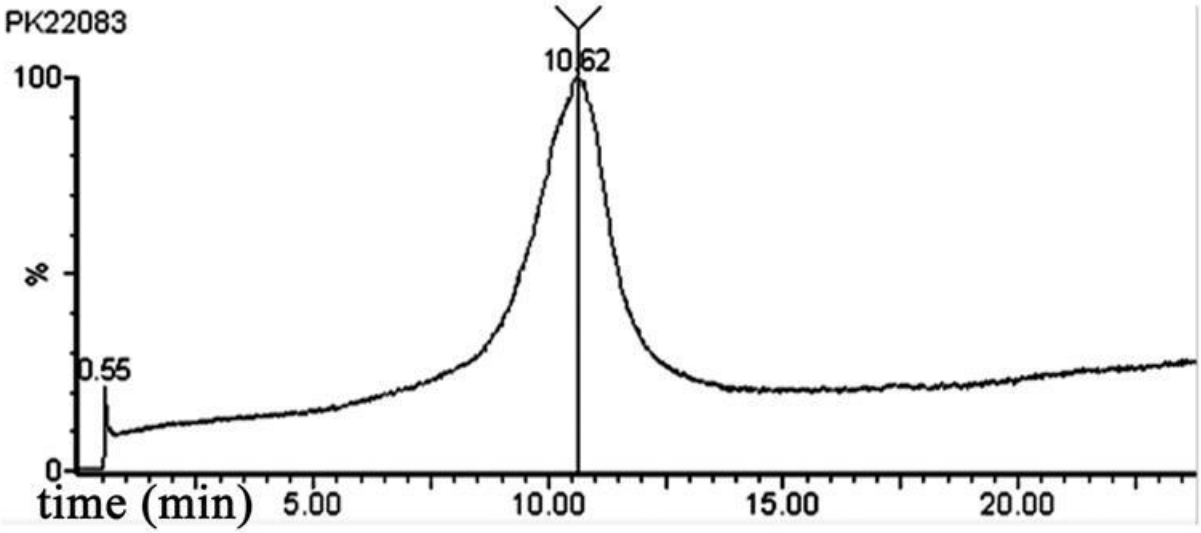

Figure 3-12. Temperature programmed desorption (TPD) chromatogram (total ions) of DPPD on hematite at a heating rate of 20 K/min.

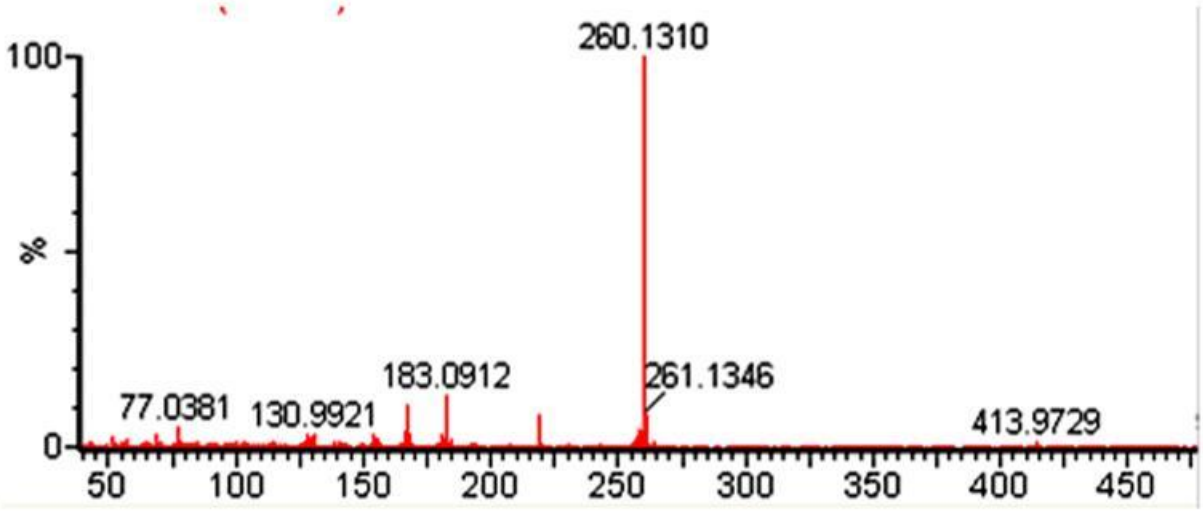

Figure 3-13. The mass spectrum at the peak point of the chromatogram in Fig 3.12 shows that DPPD desorbs from the hematite surface intact, and no decomposition is taking place.

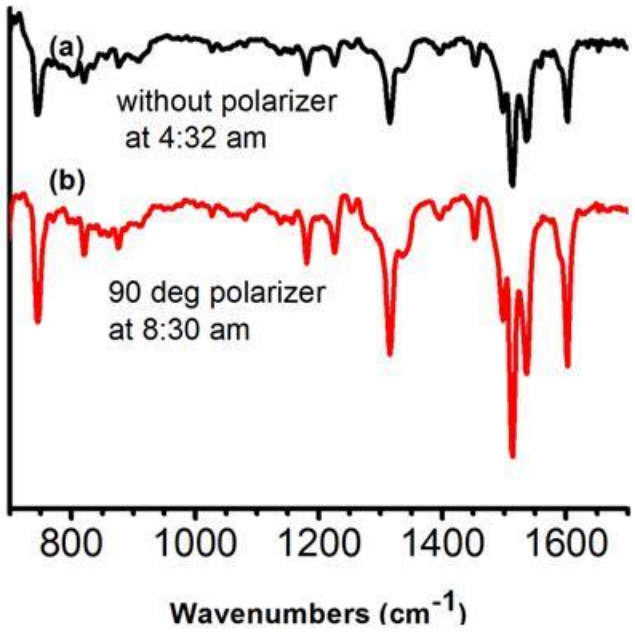

Figure 3-14. The first spectrum was taken without using any polarizer. The second spectrum was taken later the same day on the same spot using a 90˚ polarizer. There is clearly no structural change using the synchrotron source for the mid-IR.

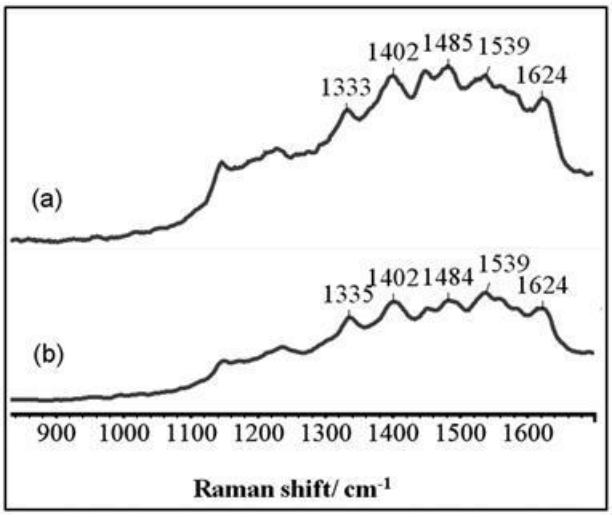

Figure 3-15. Raman spectra of a ~0.54 nm film of DPPD on a native oxide covered steel surface. (a) The first spectrum was taken with the green laser at 0.1 mW at the sample; (b) The

second spectrum was taken on the same spot using the same parameters. There is clearly no structural change.

Analysis of main desorption peak DTG Data for 1.08 nm film (2.15 ML)

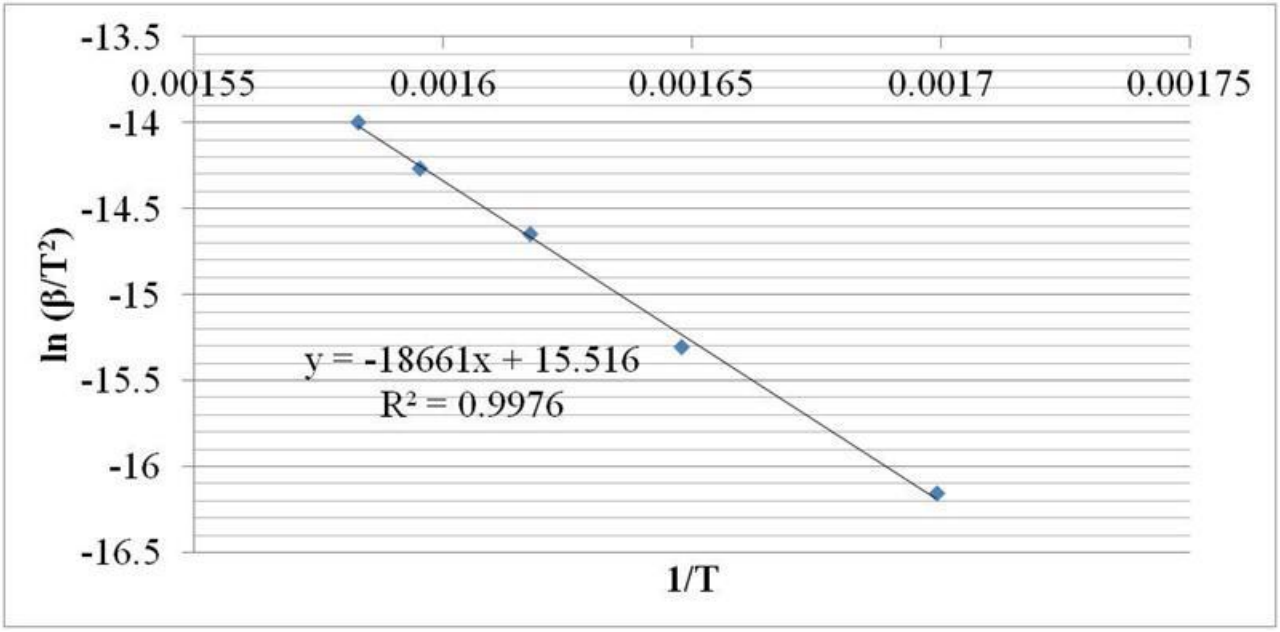

Figure 3-16. Graph $\ln(\beta/ T_p^2)$ versus $1/ T_p$ using the Peak temperature from each rate of a 1.08 nm film on hematite. From the slope, Ed/R was calculated.

Heating rate β (deg/min)	Peak temperature (˚C)	Peak temperature T(K)	T^2	T^2*60	1/T	ln (β/T^2)
2	315.5536	588.5536	346395.3401	20783720.4	0.001699081	-16.15653338
5	333.88778	606.88778	368312.7775	22098766.65	0.001647751	-15.30159444
10	345.21567	618.21567	382190.6146	22931436.88	0.001617558	-14.64543422
15	353.8277	626.8277	392912.9655	23574777.93	0.001595335	-14.26763777
20	358.74423	631.74423	399100.7721	23946046.33	0.001582919	-13.99558151

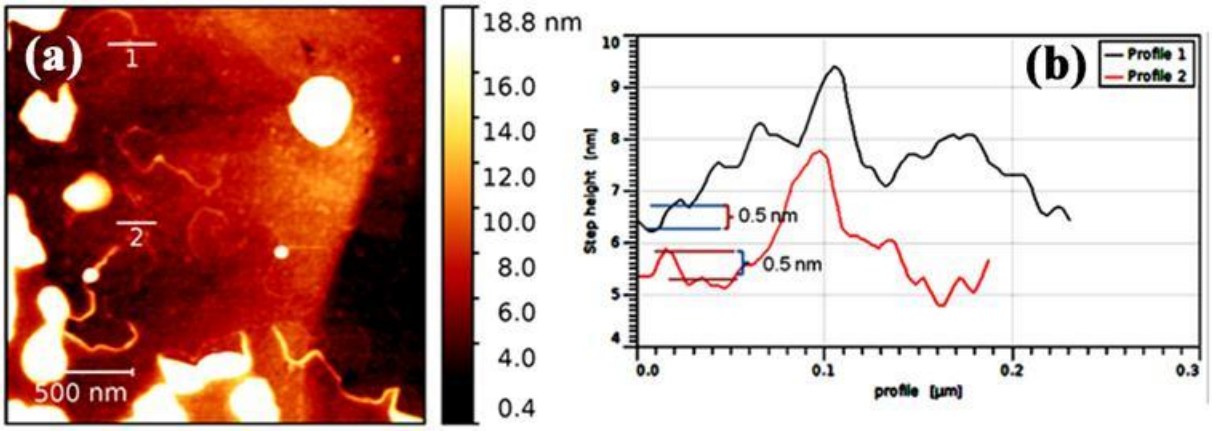

Figure 3-17. (a) An example of cross-sections in an AFM image for the 10˚C substrate temperature sample (zoomed in), (b) Examples of line profiles of the AFM image.

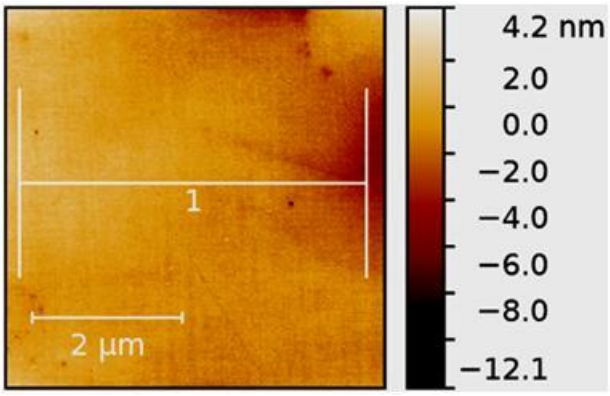

Figure 3-18. Native oxide covered clean steel. Roughness parameters are shown in the table below.

Roughness Parameters

Selected line: (8, 118) to (245, 118) px

(0.17, 2.31) to (4.79, 2.31) Â µm

Amplitude			
Roughness average	(Ra):	0.05	nm
Root mean square roughness	(Rq):	0.065	nm
Maximum height of the roughness	(Rt):	0.469	nm
Maximum roughness valley depth	(Rv):	0.266	nm
Maximum roughness peak height	(Rp):	0.203	nm
Average maximum height of the roughness	(Rtm):	0.276	nm
Average maximum roughness valley depth	(Rvm):	0.147	nm
Average maximum roughness peak height	(Rpm):	0.129	nm
Average third highest peak to third lowest valley height	(R3z):	0.286	nm
Average third highest peak to third lowest valley height	(R3z ISO):	0.083	nm
Average maximum height of the profile	(Rz):	0.267	nm
Average maximum height of the roughness	(Rz ISO):	0.276	nm
Kurtosis	(Rku):	4.364	
Waviness average	(Wa):	0.887	nm
Root mean square waviness	(Wq):	1.093	nm
	(Wy=Wmax) :	4.629	nm
Maximum height of the profile	(Pt):	4.803	nm
Spatial			
Average wavelength of the profile	(Î»a):	0.18	Âµm
Root mean square (RMS) wavelength of the profile	(Î»q):	0.18	Âµm
Hybrid			
Average absolute slope	(Î”a):	1.78	4 10^-3
Root mean square (RMS) slope	(Î”q):	2.28	7 10^-3
Length	(L):	4.65	Âµm
Developed profile length	(L0):	4.65	Âµm
Profile length ratio	(lr):	1	

3.6 REFERENCES

(1) Tokito, S.; Noda, K.; Taga,Y. Metal Oxides as a Hole-Injecting Layer for an Organic Electroluminescent Device. *J. Phys. D: Appl. Phys.* **1996***, 29*, 2750-2753.

(2) Matsushima, T.; Jin, G.-H.; Murata, H. Marked Improvement in Electroluminescence Characteristics of Organic Light-Emitting Diodes Using an Ultrathin Hole-Injection Layer of Molybdenum Oxide. *J. Appl. Phys.* **2008**, *104*, 054501.

(3) Chu, C. W.; Li, S. H.; Chen, C. W.; Shrotriya, V.; Yang, Y. High-Performance Organic Thin-Film Transistors with Metal Oxide/Metal Bilayer Electrode. *Appl. Phys. Lett.* **2005**, *87*, 193508.

(4) Nattestad, A.; Mozer, A. J.; Fischer, M. K. R.; Cheng, Y.-B.; Mishra, A.; Bäuerle, P.; Bach, U. Highly Efficient Photocathodes for Dye-Sensitized Tandem Solar Cells. *Nat. Mater.* **2010**, *9*, 31–35.

(5) Kinoshita, Y.; Takenaka, R.; Murata, H. Independent Control of Open-Circuit Voltage of Organic Solar Cells by Changing Film Thickness of MoO_3 Buffer Layer. *Appl. Phys. Lett.* **2008**, *92*, 243309.

(6) Rowell, M. W.; Topinka, M. A.; McGehee, M. D.; Prall, H.-J.; Dennler, G.; Sariciftci, N. S.; Hu, L.; Gruner, G. Organic Solar Cells with Carbon Nanotube Network Electrodes. *Appl. Phys. Lett.* **2006**, *88* (23), 233506.

(7) Sheehan, S. W.; Thomsen, J. M.; Hintermair, U.; Crabtree, R. H.; Brudvig, G. W.; Schmuttenmaer, C. A. A Molecular Catalyst for Water Oxidation That Binds to Metal Oxide Surfaces. *Nat. Commun.* **2015**, *6*, 6469.

(8) de Souza, S. Smart Coating Based on Polyaniline Acrylic Blend for Corrosion Protection of Different Metals. *Surf. Coat. Technol.* **2007**, *201* (16–17), 7574–7581.

(9) Radhakrishnan, S.; Siju, C. R.; Mahanta, D.; Patil, S.; Madras, G. Conducting Polyaniline–nano-TiO_2 Composites for Smart Corrosion Resistant Coatings. *Electrochim. Acta* **2009**, *54 (4),* 1249–1254.

(10) Wessling, B. Passivation of Metals by Coating with Polyaniline: Corrosion Potential Shift and Morphological Changes. *Adv. Mater.* **1994**, *6,* 226–228.

(11) Ramachandran, S.; Tsai, B.-L.; Blanco, M.; Chen, H.; Tang, Y.; Goddard, W. A. Self-Assembled Monolayer Mechanism for Corrosion Inhibition of Iron by Imidazolines. *Langmuir* **1996**, *12*, 6419–6428.

(12) Faust, B. C.; Hoffmann, M. R.; Bahnemann, D. W. Photocatalytic Oxidation of Sulfur Dioxide in Aqueous Suspensions of α-Iron Oxide (Fe_2O_3). *J. Phys. Chem.* **1989**, *93*, 6371.

(13) Cornell, R. M.; Schwertmann, U. The Iron Oxides - Structure, Properties, Occurrences and Uses, 2nd ed.; Wiley: Weinheim, **2003**.

(14) DeBerry, D. W. Modification of the Electrochemical and Corrosion Behavior of Stainless Steels with an Electroactive Coating. *J. Electrochem. Soc.* **1985**, *132*, 1022–1026.

(15) Spinks, G.; Dominis, A.; Wallace, G.; Tallman, D. Electroactive Conducting Polymers for Corrosion Control. *J. Solid State Electrochem.* **2002**, *6*, 85–100.

(16) Rohwerder, M.; Duc, L. M.; Michalik, A. In Situ Investigation of Corrosion Localized at the Buried Interface Between Metal and Conducting Polymer Based Composite Coatings. *Electrochim. Acta* **2009**, *54*, 6075–6081.

(17) Uvdal, K.; Lögdlund, M.; Dannetun, P.; Bertilsson, L.; Stafström, S.; Salaneck, W. R.; MacDiarmid, A. G.; Ray, A.; Scherr, E. M.; Hjertberg, T.; et al. Vapor Deposited Polyaniline. *Synth. Met.* **1989**, *29*, 451–456.

(18) Greiner, M. T.; Festin, M.; Kruse, P. Investigation of Corrosion-Inhibiting Aniline Oligomer Thin Films on Iron Using Photoelectron Spectroscopy. *J. Phys. Chem. C* **2008**, *112*, 18991–19004.

(19) De Almeida, M. P.; Carabineiro, S. A. C. The Best of Two Worlds from the Gold Catalysis Universe: Making Homogeneous Heterogeneous. *ChemCatChem* **2012**, *4*, 18–29.

(20) Falconer, J. L.; Madix, R. J. Flash Desorption Activation Energies: DCOOH Decomposition and CO Desorption from Ni (110). *Surf. Sci.* **1975**, *48*, 393–405.

(21) Gawlicka-Chruszcz, A.; Stadnicka, K. A Comparative Study of Intermolecular Interactions in the Crystal Structures of Phenyl/Phenyl End-Capped Oligoanilines. *Acta Crystallogr. C* **2002**, *58* (7), 0416–0420.

(22) Nečas D.; Klapetek, P. Gwyddion: An Open-Source Software for SPM Data Analysis, *Open Phys.* **2012,** *10,* 181-188.

(23) Chen, L.; Yu, Y.; Mao, H.; Lu, X.; Zhang, W.; Wei, Y. Synthesis of Phenyl-Capped Aniline Heptamer and Its UV–Vis Spectral Study. *Synth. Met.* **2005**, *149*, 129-134.

(24) Boyer, M.; Quillard, S.; Cochet, M.; Louarn, G.; Lefrant, S. RRS Characterization of Selected Oligomers of Polyaniline In Situ Spectroelectrochemical Study. *Electrochim. Acta* **1999**, *44*, 1981-1987.

(25) Monkman, A. P.; Bloor, D.; Stevens, G. C.; Stevens, J. C. H.; Wilson, P. Electronic Structure and Charge Transport Mechanisms in Polyaniline. *Synth. Met.* **1989**, *29 (1),* 277–284.

(26) Jelle, B. P.; Hagen, G.; Hesjevik, S. M.; Ødegård, R. Reduction Factor for Polyaniline Films on ITO from Cyclic Voltammetry and Visible Absorption Spectra. *Electrochim. Acta* **1993**, *38*, 1643-1647.

(27) Quillard, S.; Corraze, B.; Boyer, M. I.; Fayad, E.; Louarn, G.; Gerard, F. Vibrational Characterisation of a Crystallised Oligoaniline: A Model Compound of Polyaniline. *J. Molec. Struc.* **2001**, *596*, 33-40.

(28) Quillard, S.; Louarn, G.; Lefrant, S.; Macdiarmid, A. G. Vibrational analysis of polyaniline: A Comparative Study of Leucoemeraldine, Emeraldine, and Pernigraniline Bases. *Phys. Rev. B* **1994**, *50*, 12496-12508.

(29) Cochet, M.; Louarn, G.; Quillard, S.; Boyer, M. I.; Buisson, J. P.; Lefrant, S. Theoretical and Experimental Vibrational Study of Polyaniline in Base Forms: Non-Planar Analysis. Part I. *J. Raman Spectrosc.* **2000**, *31* (11), 1029–1039.

(30) de Santana, H.; Quillard, S.; Fayad, E.; Louarn, G. In Situ UV–Vis and Raman Spectroscopic Studies of the Electrochemical Behavior of N,N'-Diphenyl-1,4-Phenylenediamine. *Synth. Met.* **2006**, *156*, 81-85.

(31) Harada, I.; Furukawa, Y.; Ueda, F. Vibrational Spectra and Structure of Polyaniline and Related Compounds. *Synth. Met.* **1989**, *29*, 303–312.

(32) Lindfors, T.; Ivaska, A. Raman Based pH Measurements with Polyaniline. *J. Electroanal. Chem.* **2005**, *580*, 320–329.

(33) Lindfors, T.; Kvarnström, C.; Ivaska, A. Raman and UV–vis Spectroscopic Study of Polyaniline Membranes Containing a Bulky Cationic Additive. *J. Electroanal. Chem.* **2002**, *518*, 131–138.

(34) de Faria, D. L. A.; Venâncio Silva, S.; de Oliveira, M. T. Raman Microspectroscopy of some Iron Oxides and Oxyhydroxides. *J. Raman Spectrosc.* **1997**, *28*, 873-878.

(35) Kellenberger, A.; Dmitrieva, E.; Dunsch, L. Structure Dependence of Charged States in "Linear" Polyaniline as Studied by In Situ ATR-FTIR Spectroelectrochemistry. *J. Phys. Chem. B,* **2012**, *116*, 4377–4385.

(36) Kostić, R.; Raković, D.; Davidova, I. E.; Gribov, L. A. Vibrational Spectroscopy of the Leucoemeraldine Form of Polyaniline: Theoretical Study. *Phys. Rev. B* **1992**, *45* (2), 728 –733.

(37) Ping, Z.; Nauer, B. G. E.; Neugebauer, H.; Theiner, J.; Neckel, A. Protonation and Electrochemical Redox Doping Processes of polyaniline in Aqueous Solutions: Investigations Using Insitu FTIR-ATR Spectroscopy and a New Doping System. *J. Chem. Soc. Faraday Trans.* **1997**, *93* (1), 121–129.

(38) Boyer, M.-I.; Quillard, S.; Rebourt, E.; Louarn, G.; Buisson, J. P.; Monkman, A.; Lefrant, S. Vibrational Analysis of Polyaniline: A Model Compound Approach. *J. Phys. Chem. B* **1998**, *102*, 7382–7392.

Table of Contents (TOC) Graphic

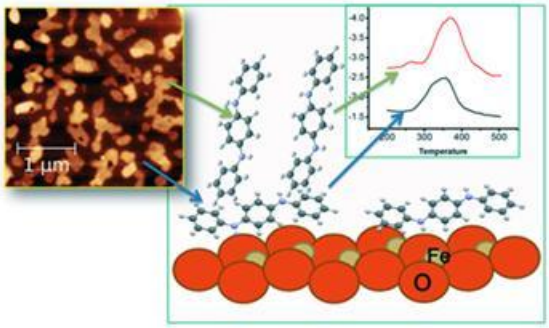

CHAPTER -4
NATURE OF THE INTERACTION OF N'N-DIPHENYL-1,4- BENZOQUINONEDIIMINE WITH IRON OXIDE SURFACES AND ITS MOBILITY ON THE SAME SURFACES

Tanzina Chowdhury, Amirmasoud Mohtasebi, and Peter Kruse[*]

Department of Chemistry and Chemical Biology, McMaster University, 1280 Main Street West, Hamilton, Ontario L8S 4M1, Canada.

ABSTRACT: Short chain aniline oligomers are of interest for applications in organic electronics and as corrosion inhibitors for steel, requiring an improved understanding of their interactions with metal oxide films. Here we investigate the interactions of N,N'-Diphenyl-1,4-benzoquinonediimine (B2Q1, oxidized form of an aniline dimer) with iron (III) oxides. B2Q1 transforms into its semiquinone form when interacting with α-Fe_2O_3. The resulting charge transfer between B2Q1 and α-Fe_2O_3 is demonstrated with mid-IR, visible and Raman spectroscopy. Atomic force microscopy shows the first layer of B2Q1 to be oriented face-on. Thermal analysis also confirms this orientation for sub-monolayer coverage, whereas molecules start standing up on their edges upon multilayer formation. Thermal analysis shows that the first monolayer of B2Q1 is chemisorbed on the α-Fe_2O_3 surface, and the following multilayers are strongly interacting with each other. The behavior of the oxidized aniline dimer B2Q1 is in stark contrast to its reduced counterpart (DPPD), which also undergoes charge transfer to iron oxide (in opposite direction). B2Q1 interacts more weakly with the surface, causing it to be

more mobile. The mobility of B2Q1 provides a clue towards understanding the self-healing behavior of polyaniline corrosion-inhibiting films on steel.

* To whom correspondence should be addressed. Email: pkruse@mcmaster.ca. Phone: +1 (905) 525-9140 ext. 23480. Fax: +1 (905) 522-2509

4.1 INTRODUCTION

Thin films of conducting polymers have become a very active field of research because of their potential applications in electronic devices such as sensors,[1] light-emitting diodes,[2,3] solar cells,[4] and thin film transistors.[5-6] Another commonly explored application of conducting polymers is as coatings for the corrosion protection of oxidizable metals.[7,8] Polyaniline (PANI) is one of the most popular polymers to study because of its high conductivity, ease of synthesis and unique redox properties.[9,10] PANI coatings were reported to inhibit corrosion of iron or steel in acidic media by DeBerry over 30 years ago.[7] These coatings are claimed to continue to protect even after sustaining mechanical damage.[8,11,12] Despite the obvious benefits of self-healing coatings, little is known about the origin of this phenomenon in the case of PANI. To understand the mechanism of corrosion inhibition it is important to understand how the molecules interact with the underlying metal oxides.

A problem with PANI coatings is that they can break down catastrophically due to their high conductivity and long range interactions, rendering these coatings unsuitable for commercial applications.[13] PANI oligomers do not share the same drawbacks but have been shown to have the same redox properties as PANI.[14] They may therefore be suitable alternatives to replace

PANI for applications in corrosion inhibition.[15] The shorter chain length of oligomers also has the advantage of making them well defined and suitable for vacuum deposition. Moreover, previous research in our group suggested that the phenyl-capped aniline tetramer (PCAT) can travel hundreds of microns along the substrate surface.[16] Here we focus on the phenyl-capped dimer (Figure 4.1), the shortest oligomer of polyaniline, as a simplified model of a corrosion inhibitor. Previous work in our group examined the interactions of N'N-Diphenyl-1,4-phenylenediamine (DPPD), the fully reduced form of the phenyl-capped dimer with iron oxide surfaces. Charge transfer was observed to take place between iron oxide surfaces and DPPD molecules standing on their edge in the first layer.[17] Because charge transfer impacts the redox state of the molecules, it is important to also consider the interaction of N,N'-Diphenyl-1,4-benzoquinonediimine (B2Q1), the fully oxidized phenyl-capped dimer, with iron oxide surfaces. This species has two hydrogen atoms less than DPPD. This imine form of the phenyl-end capped-dimer can mimic the same constituting units as the pernigraniline base or fully oxidized form of PANI.

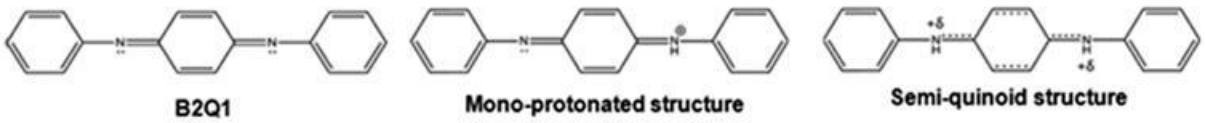

Figure 4-1. The structure of B2Q1 in mono-protonated and semiquinone form.

Here we investigate the nature of the interactions of B2Q1 with iron oxide surfaces using Raman and mid-IR spectroscopy. The strength of these interactions was investigated through thermo-gravimetric analysis (TGA). Atomic force microscopy (AFM) and IR spectromicroscopy were used to determine the orientation of B2Q1 on iron oxide surfaces.

These investigations also gave us insight into the ability of B2Q1 to migrate along iron oxide surfaces. Detailed knowledge of the interactions in the B2Q1-iron oxide system can now be applied to the understanding of more complex oligoaniline and polyaniline systems.

4.2 EXPERIMENTAL DETAILS

Iron (III) oxide (α-Fe_2O_3) nanopowder (<50 nm particle size, surface area 16 mg/m^2) was obtained from Sigma-Aldrich and low carbon steel (α-Fe, ~0.5% Mn) was obtained from Dofasco. The steel sheets were cut into 1 cm × 1 cm coupons and mechanically polished first using coarse grit silicon carbide emery paper followed by 3 μm and 1 μm diamond particle emulsion. The final polishing step was 0.05 μm colloidal silica. Each of the samples was then washed with water and ultrasonically cleaned with acetone and methanol.

B2Q1 powder was prepared by first mixing DPPD (Sigma-Aldrich) (DPPD : ammonium persulfate molar ratio of 1 : 0.88) with ammonium persulfate (reagent grade 98%, Sigma-Aldrich), then dissolving the mixture in methanol and stirring for 24 hours. Methanol was evaporated and the residue was washed several times with de-ionized water to remove residual ammonium persulfate, and then vacuum suctioned and dried in a desiccator. Ascorbic acid was used to obtain the reduced form of the phenyl-capped dimer, with a DPPD to ascorbic acid molar ratio of 1:1.36, following otherwise the same procedure as for making the oxidized form.

Raman spectroscopy is performed using a Renshaw InVia Raman microscope with a 514.5 nm green laser (laser power 0.07-0.1 mW at the sample). The laser beam was focused on the sample by a 20× lens to give a spot size of ca. 1 μm. Raman spectroscopy was used to

characterize pure B2Q1 as well as a B2Q1/Fe_2O_3 powder mixture, and also drop cast B2Q1 on a steel coupon.

In order to examine the orientation of the molecules, B2Q1 was vacuum deposited onto steel coupons in a home-built vacuum deposition chamber (base pressure better than 2×10^{-6} Torr) with a variable temperature sample mount. Three substrate temperatures were chosen (6˚C, 25˚C and 40˚C) as measured by a thermocouple attached next to the sample. Three different thicknesses (1.8 nm at 6˚C, 10 nm at 25 ˚C and 3 nm at 40˚C) of B2Q1 were deposited, monitored by a quartz crystal microbalance. B2Q1 was also deposited in a sublimation apparatus connected to a sorption pump in which the steel coupon was attached using a double-sided tape underneath the flat bottom of the cold finger. For the sample designated as "half & half" below, a glass slide was mounted over one half the sample as contact mask to yield a clean division between coated and uncoated halves of the sample without introducing additional contaminations.

Several sublimated samples were mapped by mid-IR spectromicroscopy at the Canadian Light Source, Saskatoon, SK. The two endstations are Bruker Vertex 70v/S spectrometers with a Hyperion 3000 microscope (online system) and a IFS 66v/S spectromicroscope (offline system). The first one is equipped with a 100-micron size single element MCT detector and a 64x64 pixel focal plane array detector (used with beamline). The second one has only a MCT detector. For observing the thin layer of B2Q1 on a steel surface both grazing incidence of reflection (GIR) and attenuated total reflection (ATR) objectives were used. GIR was used in the online system and ATR in the offline system. The online system was also used with a GIR

objective and 90˚ and 0˚ polarizer orientations for investigating the orientation of B2Q1 on the iron oxide surface. The sample deposited at 25˚C (10 nm film) was used for this purpose.

Thermal gravimetric analysis (TGA) was performed on different thicknesses of B2Q1 on α-Fe_2O_3 surfaces with heating rates of 2, 5, 10, 15 and 20 deg/min using a Netzsch STA-409 'Luxx', which is a simultaneous thermal gravimetric analyzer and a differential thermal analyzer (DTA). In TGA the samples were run in air using standard Al_2O_3 crucibles with a temperature range of 0-1200˚C. The derivative of the TGA (DTG) curve was taken to analyze the data. From the DTG analysis, the desorption energies of 0.28, 0.42, 0.56 and 1.12 nm films of B2Q1 on α-Fe_2O_3 were analyzed using the Falconer and Madix method.[17,18] The desorbed species were verified by mass spectrometry (Figure S1) over a temperature range of 50-450˚C in a Varian CP-3800 Gas chromatograph with a Varian 2200 ion trap mass selective detector. The sample used for both TGA and temperature programmed desorption (TPD) was a mixture of B2Q1 and α-Fe_2O_3 nanoparticle powder in different ratios. It was mixed manually with a pestle in a ceramic mortar to achieve homogeneity.

AFM was performed using a Veeco Enviroscope with a Nanoscope IIIa controller and Veeco RTESPA phosphorus (n-doped) Si tips with nominal radii of 10 nm or less. The AFM images were analyzed using Gwyddion data analysis software version 2.44.[19] Scanning electron microscopy (SEM) was used to complement the AFM data. Another three kinds of sample were prepared on clean steel to observe the interaction of B2Q1 with α-Fe_2O_3 such as (i) sonicating the steel substrate in B2Q1 and methanol solution, (ii) sonicating the steel substrate in reduced DPPD and methanol solution, (iii) drop casting B2Q1 and methanol solution on the steel

substrate. Raman spectra are also taken of these samples to characterize the interaction of B2Q1 with α-Fe_2O_3.

4.3 RESULTS AND DISCUSSION

Characterization of Different Forms of the Phenyl-Capped Dimer

Raman spectra were obtained to characterize the species that arise from the interactions of different forms of the phenyl-capped aniline dimer with iron (III) oxides. This technique was also used to detect and distinguish between different oxidation states of aniline oligomers. Spectra were taken on the fully oxidized (B2Q1) and fully reduced (DPPD) dimer powder as shown in Figures 4.2a and 4.2b, respectively. The Raman bands of B2Q1 (Figure 4.2a) at 1623, 1591, 1569, 1528, 1416, 1217, 1155, and 998 cm^{-1} compare well to literature reports.[20,21] All of these bands are characteristic of the quinoid structure. The Raman spectrum of DPPD (Figure 4.2b) shows intense bands at 1616 and 1193 cm^{-1}, corresponding to C-C stretching and C-H bending vibration, repectively[20] and also strong bands at 994 and 1029 cm^{-1} which arise due to ring breathing of the monosubstituted benzene.[21] All of these intense bands are characteristic of the reduced form of DPPD.

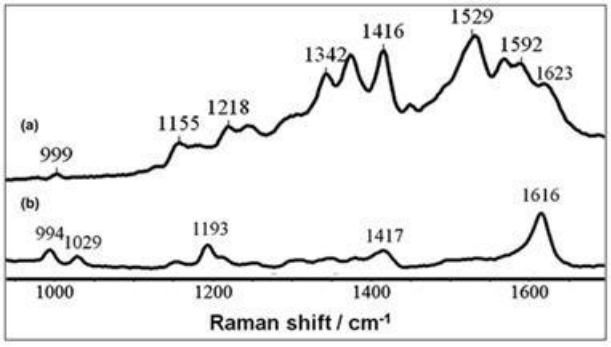

Figure 4-2. Raman spectra of (a) B2Q1 powder and (b) pure DPPD powder.

Interaction of B2Q1 with the Iron Oxide Surface

The interactions of B2Q1 with iron oxide and with methanol were observed using Raman spectroscopy in order to better understand their nature. Figure 4.3b shows a Raman spectrum of B2Q1 drop cast from methanol onto a glass substrate. The Raman bands at 1408 and 1495 cm^{-1} in this spectrum are assigned to radical cation formation in DPPD.[22] The Raman spectrum of B2Q1 drop cast from methanol onto a steel substrate in Figure 4.3a shows the same features with a slight shift. The feature still remains the same even if the molecular island is very thin on the steel surface (native oxide, α-Fe_2O_3) (See Supporting Information Figures S2a, b).

Figure 4.3c shows the Raman spectrum of a 0.28 nm film of B2Q1 on α-Fe_2O_3 in a powder mixture which had no contact with methanol. This spectrum also has Raman bands at 1401 and 1491cm^{-1} (shifted) and almost the same feature as Figures 4.3a and 4.3b except for a new band arising at 1336 cm^{-1}. This band is commonly assigned to C-$N^{+\bullet}$ stretching.[23,24] The nature of the interaction of B2Q1 with methanol and α-Fe_2O_3 appears to be similar but in the absence of methanol the molecules bond more strongly to the surface. These results suggest that B2Q1 is hydrogen bonding with the hydroxyl groups on the iron oxide surface to produce semiquinone species. It can bond with methanol in the same fashion, competing with the strong interactions with the surface. To observe the interactions of this molecule in more detail, IR and Raman spectroscopies were used to map out the deposited B2Q1 molecules on a steel coupon as shown in the next section.

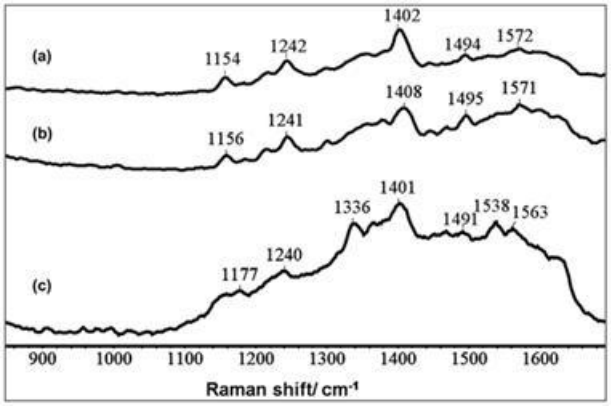

Figure 4-3. Similarities in the interactions of B2Q1 with α-Fe_2O_3 and MeOH. Raman spectra of (a) drop-cast B2Q1 from MeOH on a steel substrate (b) drop cast B2Q1 from MeOH on a glass substrate and (c) powder mixture equivalent to a 0.28 nm film of B2Q1 on α-Fe_2O_3.

The morphology of B2Q1 on the native oxide of a steel surface was also observed using scanning electron microscopy (SEM). Figure 4.4a shows the SEM image of B2Q1 on a steel substrate after sonicating the substrate for one hour in a methanolic solution of B2Q1. This image shows no trace of B2Q1 on the surface, which indicates that B2Q1 does not deposit easily on the steel surface from methanol. Raman spectra of this sample also could not identify any trace of B2Q1 or related molecules on the surface, meaning that the deposited film thickness (if any) is below the detection limit (<10 nm) of Raman spectroscopy. In contrast, DPPD (fully reduced dimer, Fig. 4.4b) attached to the surface easily and the film is thick enough to be clearly identified by Raman and SEM.

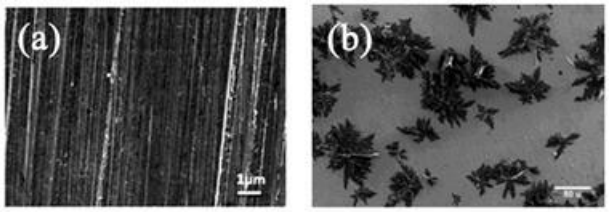

Figure 4-4. SEM images of B2Q1 sonicated ~1h on steel surface (a) and (b) image of DPPD sonicated ~1h on the steel surface.

Mapping the Interactions of B2Q1 with the Native Iron Oxide

B2Q1 was sublimed onto one-half of a steel coupon while the other half was kept clean (half & half sample). This sample was used to study the impact of ambient conditions on the evolution of the molecular film. The interaction was mapped by Raman and mid-IR spectroscopy. Some aggregates of the deposited molecules are visible as spots under the optical microscope but some aggregates are too small to be seen. Some of those small islands of molecules were picked up by Raman spectroscopy and some undetectable by Raman spectroscopy were picked up by IR spectroscopy. Figure 4.5a shows Raman bands of the very thin film of the molecules. The bands at 1580 and 1446 cm^{-1} are attributed to C-C stretching [22] and the bands at 1373, 1301 [25] and 1246 [23,24] cm^{-1} are due to $C\text{-}N^{+\bullet}$ stretching of the semiquinone radical cation. The part of the B2Q1 film that is barely visible by optical microscopy (Figure 4.5b, e) has almost the same spectral features as the semiquinone radical cation of the thin film except for the band 1580 cm^{-1}. New bands appear which are characteristic of oxidized molecules such as 998, 1033, 1416 cm^{-1} and 1624 cm^{-1}. In the thicker film (Figures 4.5c, d), most of the identifiers of the radical cation are not present and it is mainly showing B2Q1 molecules at that thickness. This observation also shows that B2Q1 transforms into the

semiquinone form only within in a thin layer in close contact with iron oxide. The signal from the interfacial layer is overwhelmed by the bulk B2Q1 film signal in thicker films, illustrating the importance of performing spectroscopy on thin films.

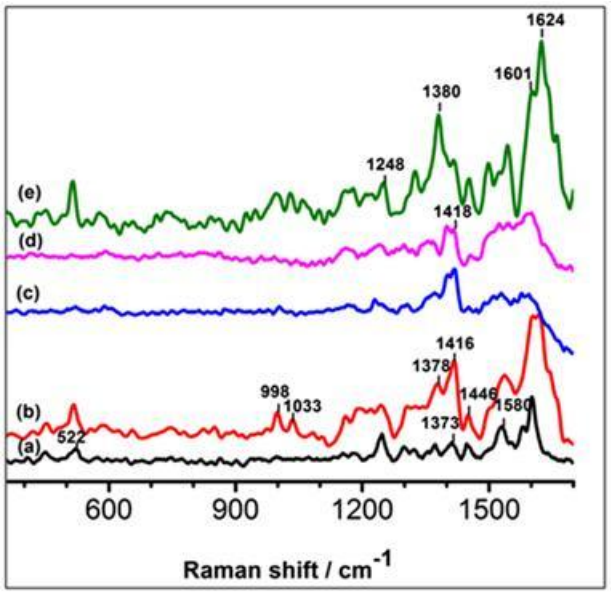

Figure 4-5. Vacuum deposited B2Q1 on a steel surface (half & half sample). Raman spectra of (a) thin film of B2Q1 on the α-Fe_2O_3 surface, (b) and (e) are B2Q1 film of intermediate thickness and (c) and (d) are a very thick film of B2Q1.

Synchrotron-based mid-IR spectroscopy was used to study a vacuum deposited B2Q1 sample because Raman spectroscopy is not sensitive enough to detect sub-monolayer or monolayer coverage, or surface water and hydroxyl groups. Figure 4.6a shows an ATR mid-IR spectrum of a clean iron oxide surface (different sample). The spectrum in Figure 4.6b was taken ~500 μm away from the deposition edge on the vacuum deposited half & half sample. Figures 4.6c-f show mid-IR spectra, mapping the B2Q1 layer in an order of further away from the deposited edge towards the deposited edge of the vacuum deposited half & half sample.

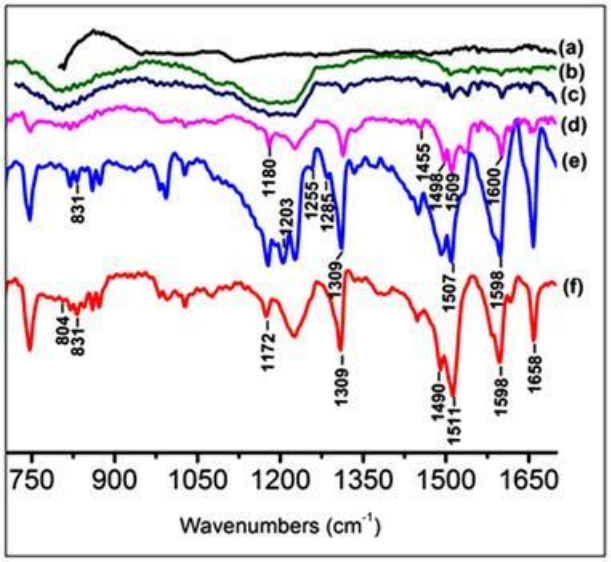

Figure 4-6. Vacuum deposited B2Q1 on an iron oxide surface. (a) ATR mid-IR spectra of clean steel substrate (different sample). GIR mid-IR spectra (b) very far (~500 µm away) from the deposited edge of the vacuum deposited half & half sample, (c) - (f) are in an order of towards the B2Q1 deposited edge.

The film of B2Q1 is shown to become gradually thicker towards the deposited edge in the map of mid-IR spectra. The spectra in Figures 4.6c-d are indicative of a very thin film of molecules. For the film in Figure 4.6c which may be thinner than that of Figure 4.6d, the IR bands at 1309, 1455, 1498, 1509 and 1600 cm^{-1} belong to B2Q1 molecules. The bands at 1309 and 1498 cm^{-1} are attributed to semiquinone ring stretching of the molecules[26] whereas the band at 1600 cm^{-1} is due to reduced DPPD,[27] which indicates that some of the oxidized molecules convert into the fully reduced form when interacting with the iron oxide surface. Some of the semiquinone bands such as 1498, 1509 cm^{-1} and the reduced DPPD band 1600 cm^{-1} are very faintly visible in Figure 4.6b, where the molecules first start to show their signature (~ 500 µm

away from the deposited edge). The intensity of all of these bands increases with film thickness (Figures 4.6c-f). It also can be seen that some new bands arise in Figure 4.6e (intermediate thickness), such as 1203, 1255 and 1285 cm^{-1}. The bands at 1255 and 1285 cm^{-1} are attributed to the semiquinone species.[26] These bands disappear as the film becomes thicker, likely due to the molecules having different orientations in the intermediate thickness film which gives rise to these bands. The band at 1658 cm^{-1} (Figure 4.6a-f) – visible on the clean iron oxide surface – increases in intensity as the film grows thicker, indicating an increase in the amount of water on the iron oxide surface.[28] AFM images of this half & half sample show the change of the molecular island shape and size with decreasing distance to the B2Q1 deposited edge (Figs. 4.7a-d). These oxidized molecules can first be observed ~700 μm away from the deposited edge in the AFM images, in contrast to the IR spectra where they were observed up to ~500 μm away. The B2Q1 molecules migrated ~500 μm from the deposited area between the time they were deposited and the IR spectrum (Figure 4.6b) was taken (~2-3 weeks). The AFM shows (Figure 4.7a) the presence of molecules even ~700 μm away from the deposited edge. This could be due to the gradual migration of B2Q1 molecules from the time of deposition (~5-6 weeks), or because IR spectroscopy was not sensitive enough to detect the molecules that migrated ~700 μm away. In order to fully characterize the interactions of the molecules with the iron oxide surface, we now focus on the molecular orientation as a function of distance from the deposited film edge.

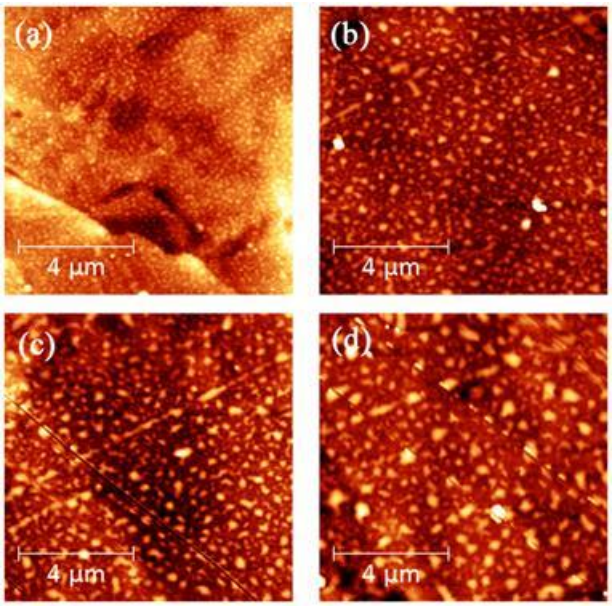

Figure 4-7. Vacuum deposited B2Q1 on a steel surface (half & half sample). (a) – (d) are AFM images in an order of towards the B2Q1 deposited edge. The image in figure (a) was taken ~700 µm away from the deposited edge which has ~ 0.3- 3 nm islands height. The images in figures (b-d) show wider islands in a height range of ~2- 15 nm.

Orientation of B2Q1 on Native Iron Oxide Surfaces

Information about the orientation of B2Q1 molecules on the iron oxide surface can be obtained from synchrotron-based mid-IR spectromicroscopy using polarized light. For this experiment, B2Q1 was vacuum deposited onto one half of the steel coupon using a tantalum mask. Figures 4.8a-g show a map of IR spectra of B2Q1 from the deposited film towards the clean part at $\theta_E = 90^\circ$.

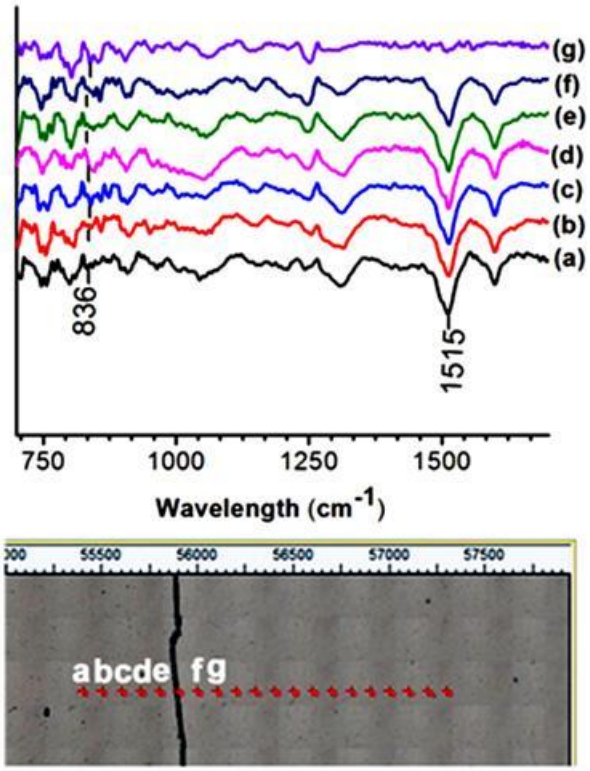

Figure 4-8. Mid-IR mapping spectra of the B2Q1 on a steel substrate at $\theta_E = 90^\circ$. The IR spectra (a-g) represent the points from the molecular film side to the clean side. These points on the sample are shown in the bottom image. The spacing between sample points (red marks) is 100 μm, for a total length of about 2 mm.

These spectra (a-g) correspond to the points (a-g) shown on the optical image of the sample in Figure 4.8. The black line in Figure 4.8 is due to a scratch made on the sample to denote the separation of deposited area and clean part. The points on the left side (Figures 4.8a-e) are on the deposited area. The spectra were taken using a grazing incident ($\theta = 80^\circ$ from the surface normal) objective in reflection geometry. Two polarizer orientations, $\theta_E = 0^\circ$ and $\theta_E = 90^\circ$ were used. With the polarizer at $\theta_E = 0^\circ$, the electric field was parallel to the substrate surface, while it was perpendicular to the substrate surface in the case of a polarizer orientation of $\theta_E = 90^\circ$.

Depending on different vibrational modes of the molecules, the IR bands can be divided into two regions: Out-of-plane ring vibrations which are mostly in the frequency range below 1000 cm^{-1}, and in-plane ring vibrations which are mostly in the medium frequency range above 1000 cm^{-1}. By taking the intensity ratio between the out-of-plane and in-plane vibration bands one can obtain orientation information about the molecules. Here we use the ratio of the two IR bands at 1515 cm^{-1} and 836 cm^{-1}. The band at 1515 cm^{-1} corresponds to the C-H in-plane bending vibration,[27] and the band at 836 cm^{-1} is attributed to the C-H out of plane wag of mono-substituted benzene. [27,29]

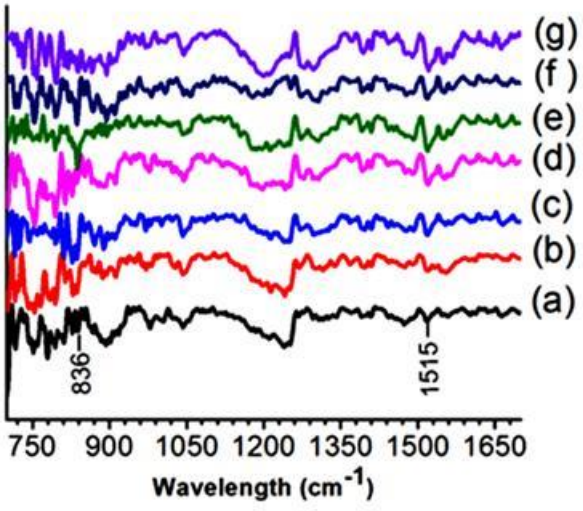

Figure 4-9. Mid-IR spectra of the DPPD on steel substrate at $\theta_E = 0^\circ$. The IR spectra (a-g) represent the points deposited film clean substrate.

IR spectra on those same points for $\theta_E = 0^\circ$ are shown in Figures 4.9a-g. Table 4.1 shows the intensity ratio for $\theta_E = 90^\circ$ and $\theta_E = 0^\circ$ between the bands at 836 cm^{-1} and 1515 cm^{-1}. The band at 836 cm^{-1} is very faintly visible for $\theta_E = 90^\circ$ for the points (a-f) in Figure 4.8 but becomes more prominent at point (g) of Figure 4.8 which is a little further away from the deposited film.

The other band at 1515 cm^{-1} shows a gradual decrease as the film is getting thinner (Figures 4.8a-g). The opposite trend can be seen for the same two bands at $\theta_E = 0^\circ$, as shown in Figures 4.9a-g. As shown in Table 4.1, the intensity ratio for $\theta_E = 90^\circ$ is low in comparison to the ratio for $\theta_E = 0^\circ$ but the overall ratio for $\theta_E = 90^\circ$ stays approximately in the same range (points (a) through (f)). The lower intensity ratio at $\theta_E = 90^\circ$ and higher intensity ratio at $\theta_E = 0^\circ$ correspond to B2Q1 molecules that are standing on their edge or upright due to their interactions with each other in the area of high coverage. The presence of the molecules past the deposited area means that molecules migrated during or after deposition [points (f-g) in Figures 4.8, 4.9], The intensity ratio shows that at the point (g) the film is thinner than at the point (f).

Table 4-1: Intensity ratio of the selected IR absorption bands for $\theta_E = 0^\circ$ and $\theta_E = 90^\circ$.

	$836cm^{-1}$ / $1515\ cm^{-1}$ for $\theta_E = 0^\circ$	$836cm^{-1}$ / $1515\ cm^{-1}$ for $\theta_E = 90^\circ$
1st point (a) of the mapping image.	2	0.22
2nd point (b)	2.4	0.12
3rd point (c)	2.3	0.35
4th point (d)	1	0.34
5th point (e)	1.6	0.25
7th point, after the molecular edge (f)	2.3	0.28
9th point (g)	1.1	2.97

The increase in intensity ratio at $\theta_E = 90^\circ$ and drop of intensity ratio at $\theta_E = 0^\circ$ for point (g) corresponds to face-on oriented molecules in a very thin film. These conclusions for the orientation of the B2Q1 molecules are drawn from the intensity ratios for $\theta_E = 90^\circ$ and $\theta_E = 0^\circ$.

Step Height Analysis of B2Q1 Films on Iron Oxide Surfaces

Atomic force microscopy (AFM) was used to analyze the step height of the B2Q1 islands on the iron oxide surface in order to be able to derive the orientation within the molecular layers. The step height analyses of B2Q1 molecules was done on both steel coupons (native oxide) and on α-Fe_2O_3(0001) single crystals in order to determine whether the orientation of B2Q1 molecules depends on the nature of the substrate. A 20 μm × 20 μm AFM height image of a steel coupon with a 3 nm vacuum deposited B2Q1 film is shown in Figure 4.10a. Figure 4.10b shows an AFM image (4 μm × 4 μm) of a hematite single crystal sample with a vacuum deposited 2 nm film of B2Q1. The AFM height images of single crystal samples show maximum island heights of around 2-10 nm. The steel coupon sample shows maximum island heights of around 4-5 nm. AFM images and corresponding line profiles are shown in Figures 4.10c, d and Figures 4.10e, f for both samples. A representative histogram of step heights from AFM images of a single crystal sample is shown in Figure 4.10g. It shows that the majority of the steps in the first layer is about ~ 0.3 nm high, very close to the expected thickness of 0.35 nm for the DPPD molecules lying face down.[30] This implies that the majority of the oxidized molecules in the first layer are lying down flat on the surface. Since the resolution of the AFM is 0.06 nm, the bin size of the histogram was set to 0.1 nm since we cannot reliably detect variations in step height that are smaller than 0.1 nm. The second largest population is at a step

height of about 0.5 nm, very close to the width of the molecules of ~0.7 nm[30] which would correspond to these molecules standing upright on their edges. We estimate the 0.5 nm film thickness to be the result of a ~45° tilt angle. According to the histogram, most of the B2Q1 molecules prefers lying down orientations during close contact with the iron oxide surface, with a sub-population in a twisted geometry or at a 45° tilt angle.

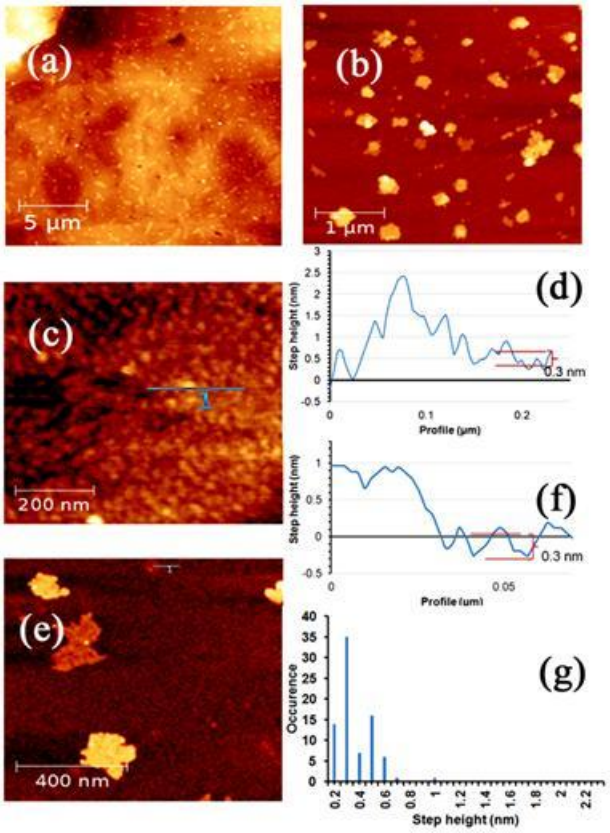

Figure 4-10. B2Q1 vacuum deposited (a) at 40˚C substrate temperature on a steel coupon, AFM height image (20 µm × 20 µm); (b) at 25˚C substrate temperature, AFM height image of a hematite single crystal (4 µm × 4 µm); (c) AFM height image of molecules on a steel coupon (700 nm × 700 nm) showing the location of the line profile; (d) line profile of AFM image; (e)

AFM height image of molecules on α-Fe_2O_3 single crystal (1 μm × 1 μm) showing the location of the line profile; (f) line profile of the AFM image (e); (g) histogram of step heights from B2Q1 on a α-Fe_2O_3 single crystal.

Desorption Energies of B2Q1 from the α-Fe_2O_3 Surface

To quantify the strength of the bonding interactions of the oxidized species with α-Fe_2O_3, Thermal Gravimetric Analysis (TGA) was performed for different thickness B2Q1 films (0.28, 0.42, 0.56 and 1.12 nm) on α-Fe_2O_3 nanoparticle surfaces (Figure 4.11). The desorption energies were calculated to be 136, 125, 144 and 149 kJ/mol respectively for the monolayer peak of powder mixtures corresponding to 0.28, 0.42, 0.56 and 1.12 nm films of B2Q1 on α-Fe_2O_3. These energies correspond to molecules being chemisorbed on the α-Fe_2O_3 surface.

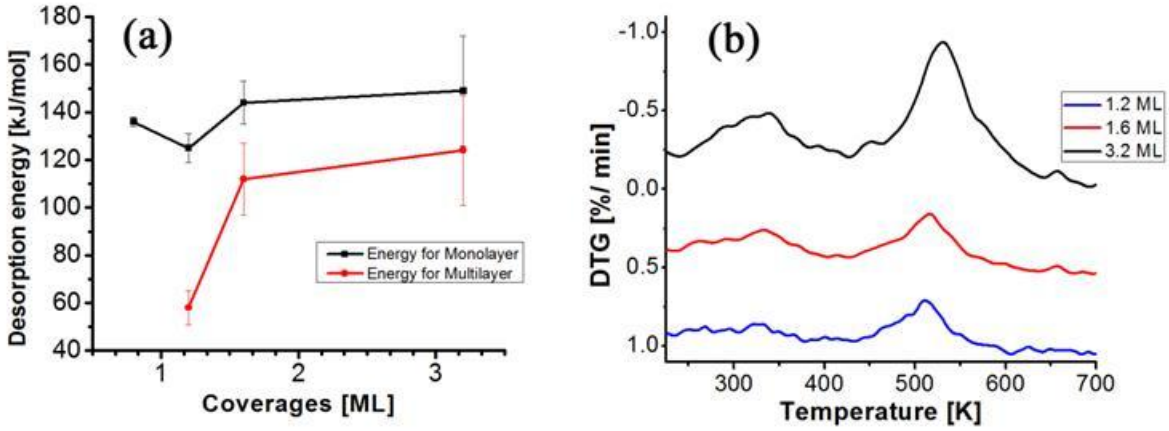

Figure 4-11. Desorption energy *vs.* coverage of B2Q1 (a) black line for monolayer peak and red line for multilayer peak. DTG spectra (b) of different coverages of B2Q1 for a 20 deg/min heating rate.

The multilayer peak first arises for the 0.42 nm film and the energies for multilayer peaks are 58, 112 and 124 kJ/mol for 0.42, 0.56 and 1.12 nm film, respectively. As discussed earlier, AFM step height analysis results show the first layer of B2Q1 to have a thickness of around 0.35 nm. Comparing AFM results with the different film thicknesses of the TGA experiment, one can see that the ~0.42 nm film corresponds to 1.2 monolayers (ML) coverage (Table 4.2) and the multilayer peak shows its trace at this coverage. The TGA result is consistent with the AFM result that the ML of B2Q1 molecules has ~0.35 nm thickness and these molecules are interacting with the iron oxide surface by lying down on the surface. The activation energy of the monolayer peak drops when the multilayer peak starts to show its trace at 0.42 nm film thickness. The drop could be due to molecules rearranging their orientation as the multilayer films start to form. The starting energy of the multilayer peak is 58 kJ/mol which shows molecules in the 2nd layer to be strongly physisorbed and in the following multilayer molecules to be strongly interacting with each other. The mass spectrometry results show that these molecules come off intact without decomposition (Figure S1).

Table 4-2: Desorption energies of B2Q1 as a function of coverage**.**

Film thickness [m]	Coverage [ML]	Desorption energy of monolayer peak [kJ/mol]	Desorption energy of multilayer peak [kJ/mol]
0.28	0.8	136 ± 2	
0.42	1.2	125 ± 6	58 ± 7
0.56	1.6	144 ± 9	112 ± 15
1.12	3.2	149 ± 23	124 ± 23

Time Evolution of B2Q1 Films on Iron Oxide Surfaces

At low temperature, vacuum deposited B2Q1 films change their morphology over a time scale observable by AFM. AFM height images (5 μm × 5 μm) of a B2Q1 film vacuum deposited at 6˚C substrate temperature (Figures 4.12a-c, e-f) show the change in molecular surface features over time. Cross-sections indicate a uniform film thickness of around 2 nm (Fig. 4.12d). It took 9 minutes to record a 5 μm × 5 μm AFM image of B2Q1. The time between Figures 4.12a and 4.12b is 18 min, between Figures 4.12b and 4.12c is 9 min, Figures 4.12a–e is 162 minutes and Figures 4.12e–f is 103 minutes. The process is observed for 265 minutes. The changes in the film slow down after 163 minutes Figures 4.12e–f and became almost imperceptible at around 265 minutes after deposition. This kind of change of the molecules was not observed for the sample deposited at 40˚C substrate temperature. Figures 4.13a-b show AFM height images of B2Q1 vacuum deposited at 40˚C. This sample shows that at higher substrate temperature during deposition the molecules immediately migrate and

aggregate into islands instead of sticking to the surface as the molecules do at lower temperature.

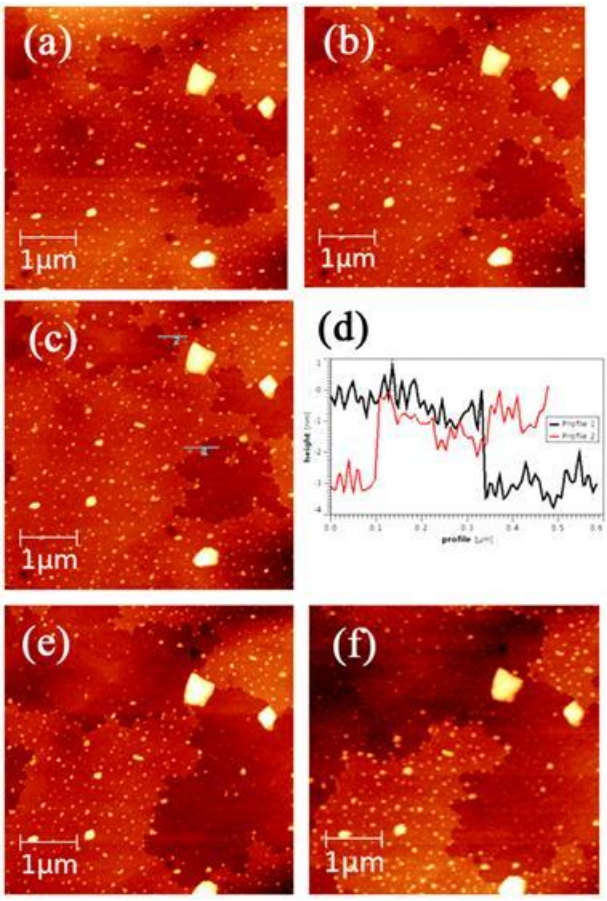

Figure 4-12. AFM height images (5 µm × 5 µm) of the B2Q1 vacuum deposited at 6˚C substrate temperature (a) – (c) and (e), the height image (5 µm × 5 µm) (zoomed in) (f) after 4 hours and 25 minutes and (d) Is the profile graph of AFM image (c).

The barrier to lateral diffusion along the surface is commonly estimated to be $1/10^{th}$ of the desorption energy. From the desorption energies calculated in the previous section, the barrier to diffusion of B2Q1 molecules on iron oxide will be ~12 to 15 kJ/mol for the first monolayer, but barely 6 kJ/mol for some molecules at the onset of multilayer formation. The product of

molar gas constant R and temperature T can be used as an approximate measure of average thermal energy, which for 6°C is about 2.3 kJ/mol and 2.6 kJ/mol at 40°C, hence coming close in magnitude to the estimate for the diffusion barrier. With increasing temperature, the thermal (kinetic) energy of the molecules increases, and as a result molecules can migrate and overcome the activation barrier. Conversely, at lower temperature molecules stick to the surface because they cannot cross the barrier.

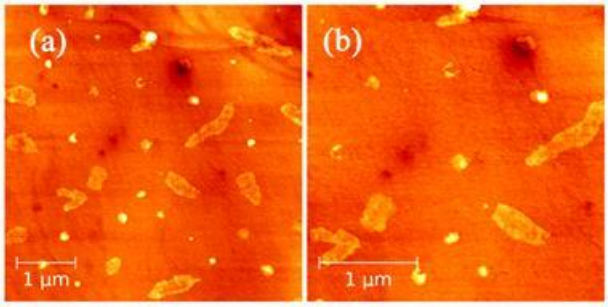

Figure 4-13. AFM height image of the B2Q1 vacuum deposited at 40˚C substrate temperature (a) 5 µm × 5 µm image and (b) zoom in at 3 µm × 3 µm.

Molecular Mobility and Oxidation State

We can also follow the mobility of aniline dimers by AFM for several days on a sample which was made by drop casting DPPD (as purchased, possibly containing small amounts of B2Q1) on a steel surface covered in native oxide (as confirmed by Raman spectroscopy). Figures 4.14a-d show the morphology of the molecules on the same spot from day 1 to day 6. There is no visible change from the first to the third day (Figures 4.14a, b). Significant changes are apparent by comparing the area in the white circle from the third day to the fourth day and also the area in a black circle on both of those days. In some areas the molecules are migrating

further apart from each other and in some areas they are filling up gaps. The induction period can be explained by the time it took for some of the DPPD to get oxidized to B2Q1 in ambient conditions, since reduced DPPD by itself is not mobile. Once the oxidized form of the molecule (B2Q1) is reduced again through surface interactions, it once again gets immobile.

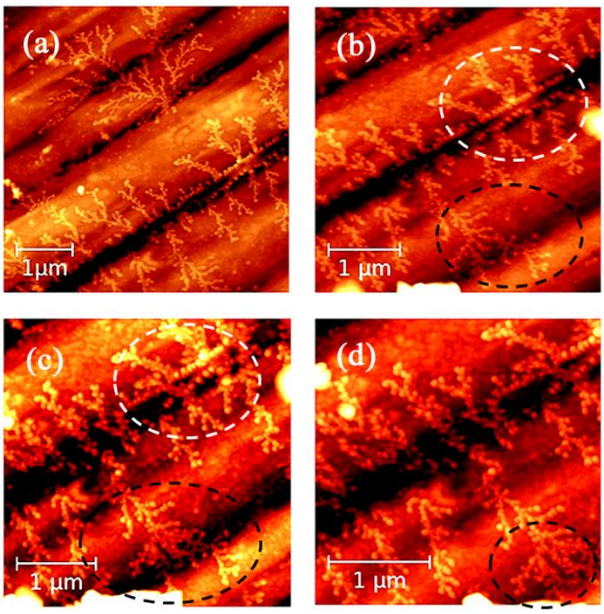

Figure 4-14. Evidence of molecular migration: DPPD on the steel sample (a) AFM image of the molecules on the 1st day. (b) 3rd day (c) 4th day and (d) 6th day.

It is very likely that both forms of the dimer (reduced and oxidized) do not possess mobility to the same extent. We have demonstrated here that B2Q1 (oxidized form) has weaker interactions with iron oxide surfaces than its reduced counterpart, and there is also evidence of dewetting by these molecules after low-temperature deposition. In our previous work, we showed evidence of DPPD (reduced form) having stronger bonding interactions with the iron oxide surface,[17] indicating that the mobile molecules on the iron oxide surface are likely the oxidized form (B2Q1) of the molecules, not DPPD.

The mobility of molecules across surfaces is key to a wide variety of processes, including catalysis, molecular self-assembly and the formation of supermolecular structures.[31,32] Many studies have been done to understand the molecular mobility on the surface, including the role of hydrogen, hydrogen bonding, and hydroxyl groups on metal oxide surfaces under ambient conditions.[32] For example, an investigation of the role of surface water on the diffusion of pyridine through MgO powder showed that presence of water significantly increases the pyridine surface diffusion coefficient by displacement of the pyridine from strong adsorption sites (Lewis acid sites) to weaker hydrogen bonded sites.[33] A study of the growth kinetics of tetracene films on silicon dioxide for molecular electronics applications concluded that the films are unstable due to continued surface diffusion.[34] All these studies showed that mobility of molecules on oxide surfaces is actually quite common. A previous study by our group had also provided indirect evidence of molecular mobility of aniline oligomers on native oxide covered steel surfaces,[16] which we were now able to confirm.

4.4 CONCLUSIONS

We have shown that B2Q1 molecules transform into the semiquinid form as the result of interacting with iron oxide surfaces. These species are chemisorbed on the iron oxide surface at monolayer or sub-monolayer coverage. As the multilayer starts to form, the multilayer species are initially strongly physisorbed and then start to interact strongly with each other. Analysis of the height of the thinnest island formation of B2Q1 on iron oxide surfaces by AFM reveals that the first layer of the oxidized molecules is lying down (face-on). Mid-IR also confirms that the orientation of the B2Q1 molecules closer to the surface is lying down but molecular multilayers

are either standing on their edge or standing up. TGA results confirm the orientation of these molecules and show that they are less strongly bound to the surface than reduced aniline dimers.

The interactions of oligonanilines with iron oxide surfaces are dominated by two effects: (1) Charge transfer due to redox-interactions, resulting in Coulomb attraction between molecules and surface; (2) Hydrogen bonding of the amine or imine groups to the iron oxide, surface hydroxide groups or surface water. Reduced oligoanilines (all amine groups) are partially oxidized on the surface and gain a positive charge (causing local reduction of Fe^{3+} to Fe^{2+}) while retaining their ability to strongly hydrogen bond through their amino groups. They are stationary on the surface. Oxidized oligoanilines (all imine groups) on the other hand are partially reduced on the surface into the semiquinoid form. They may be able to cause local oxidation of Fe^{2+} to Fe^{3+} where such defects had existed on the surface, thus creating a passive oxide film, but no localized charges in the oxide film. Therefore the opportunities for Coulomb interactions are diminished, while hydrogen bonding of imine groups to the surface is also not as strong as that of the amine groups. Hence oxidized oligoanilines easily dewet from iron oxide surfaces and show signs of mobility over long distances. Our findings about mobility and charge transfer of aniline dimers also have consequences for the study of longer oligoanilines and polyaniline, be it for molecular electronics, or self-healing corrosion inhibiting coatings.

Supporting Information: The supporting information is available free of charge on the ACS publications website at http://pubs.acs.org.

Acknowledgments

We thank Dr. Kirk Green from the McMaster regional mass spectrometry facility for his technical assistance and helpful discussions and also Dr. Steve Kornic (CAOS), and Frank Gibbs (BIMR) for assistance with Raman spectroscopy and thermal analysis, respectively. Part of the r*esearch described in this paper was performed at the Canadian Light Source, which is supported by the Canada Foundation for Innovation, Natural Sciences and Engineering Research Council of Canada, the University of Saskatchewan, the Government of Saskatchewan, Western Economic Diversification Canada, the National Research Council Canada, and the Canadian Institutes of Health Research.* We thank Dr. Ferenc Borondics, Dr. Scott Rosendahl and Dr. Xia Liu at CLS for their assistance in the mid-IR spectroscopy. Thanks to our group members for their kind support: Enamul Hoque, Stephen Yue Wang, Alan Awez, Allen Pauric, Alexander Imbault. Financial support was provided by the National Science and Engineering Research Council of Canada through the Discovery Grant program.

4.5 SUPPORTING INFORMATION

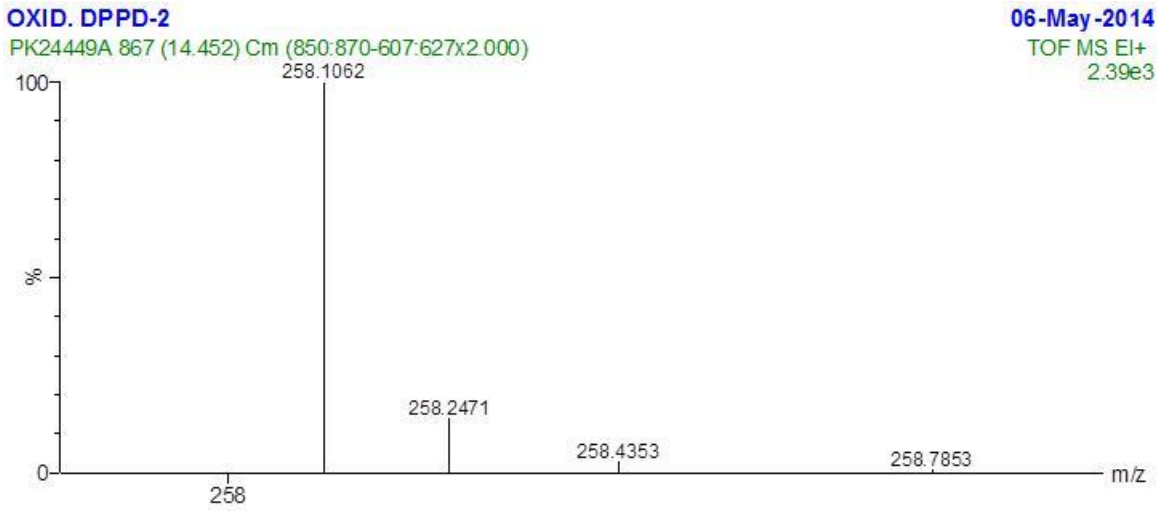

Figure 4-15. The mass spectrum of B2Q1 molecules.

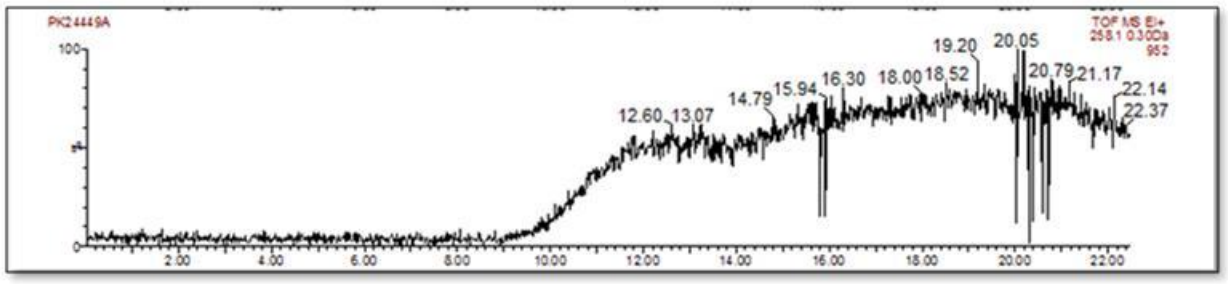

Figure 4-16. The chromatograme of B2Q1 molecules.

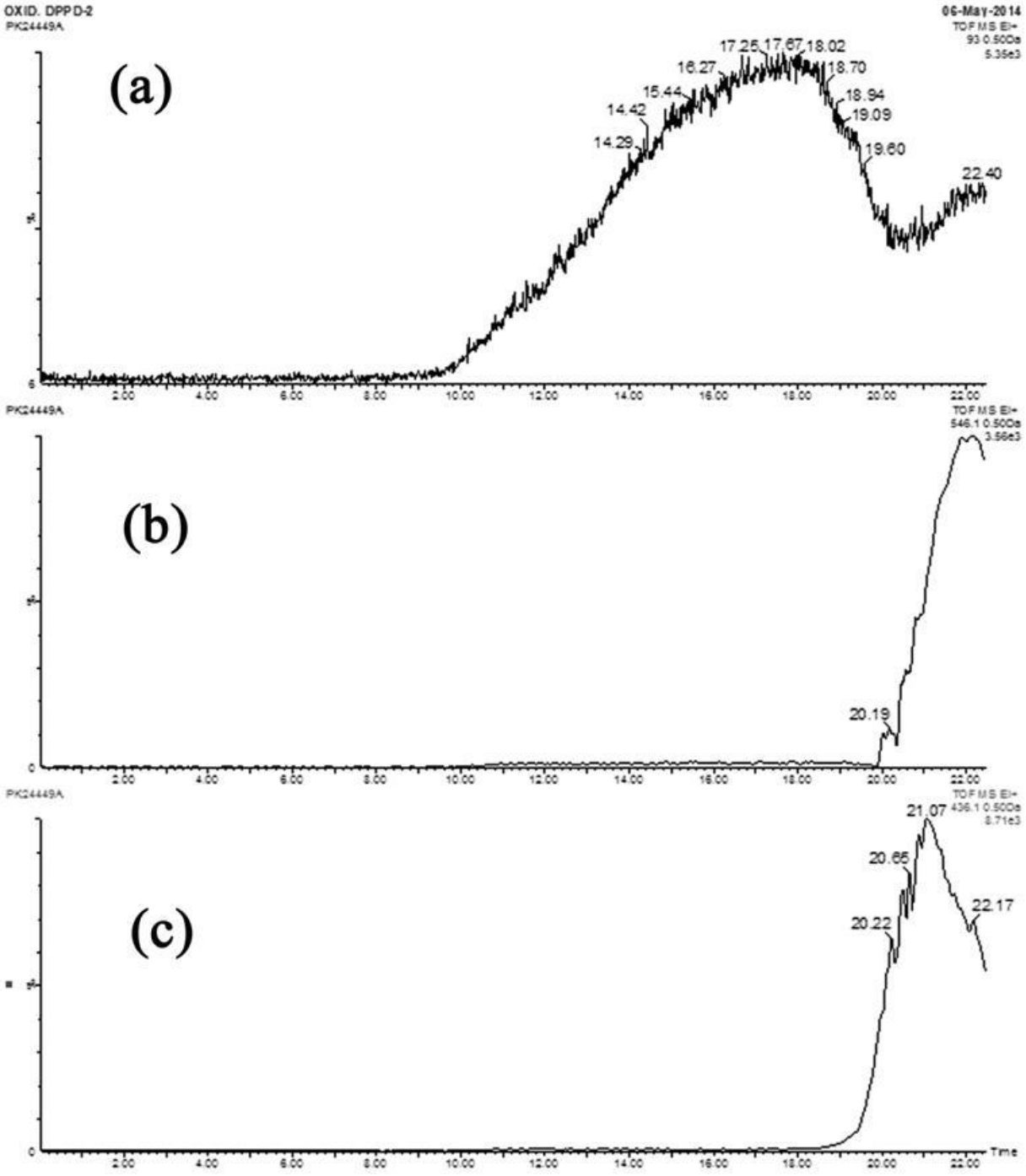

Figure 4-17. The chromatograme of B2Q1 molecules (a) overall chromatograme, (b) and (c) are chromatograme of species at higher temperature.

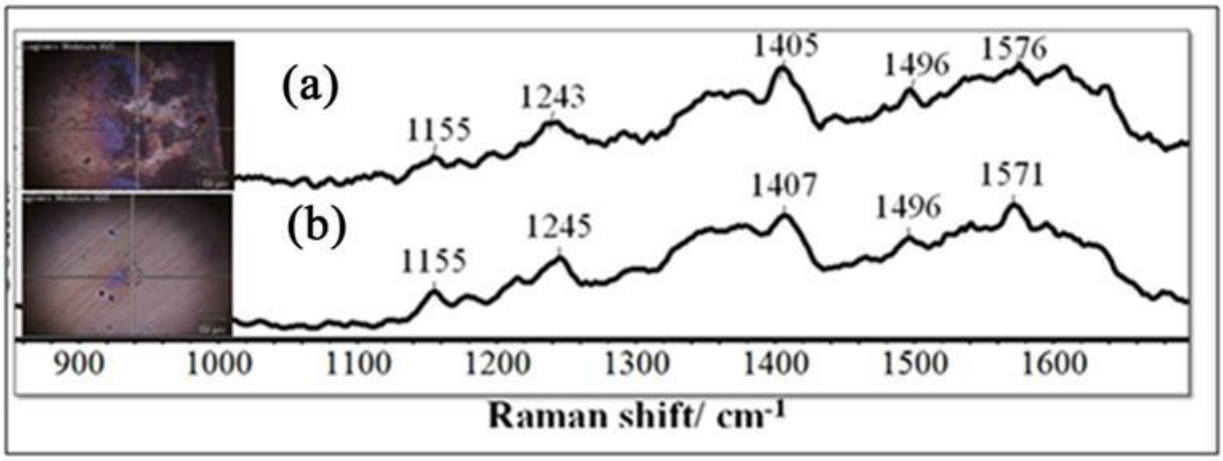

Figure 4-18. Raman spectra of B2Q1 on a steel substrate with corresponding optical image, (a) very thick molecular film on iron oxide surface and (b) very thin film of molecules.

4.6 REFERENCES

(1) Hsu, L. H. H.; Hoque, E.; Kruse, P.; Selvaganapathy, P. R. A Carbon Nanotube Based Resettable Sensor for Measuring Free Chlorine in Drinking Water. *Appl. Phys. Lett.* **2015**, *106* (6), 63102.

(2) Kabra, D.; Lu, L. P.; Song, M. H.; Snaith, H. J.; Friend, R. H. Efficient Single-Layer Polymer Light-Emitting Diodes. *Adv. Mater.* **2010**, *22* (29), 3194–3198.

(3) Matsushima, T.; Jin, G.-H.; Murata, H. Marked Improvement in Electroluminescence Characteristics of Organic Light-Emitting Diodes Using an Ultrathin Hole-Injection Layer of Molybdenum Oxide. *J. Appl. Phys.* **2008**, *104* (5), 054501.

(4) Kim, S.-S.; Na, S.-I.; Jo, J.; Kim, D.-Y.; Nah, Y.-C. Plasmon Enhanced Performance of Organic Solar Cells Using Electrodeposited Ag Nanoparticles. *Appl. Phys. Lett.* **2008**, *93* (7), 073307.

(5) Lin, Y.Y.; Gundlach, D. J.; Nelson, S. F.; Jackson, T. N. Stacked Pentacene Layer Organic Thin-Film Transistors with Improved Characteristics. *IEEE Electron Device Lett*. **1997**, *18* (12), 606–608.

(6) Katz, H. E.; Bao, Z.; Gilat, S. L. Synthetic Chemistry for Ultrapure, Processable, and High-Mobility Organic Transistor Semiconductors. *Acc. Chem. Res*. **2001**, *34* (5), 359–369.

(7) DeBerry, D. W. Modification of the Electrochemical and Corrosion Behavior of Stainless Steels with an Electroactive Coating. *J. Electrochem. Soc.* **1985**, *132*, 1022–1026.

(8) Spinks, G.; Dominis, A.; Wallace, G.; Tallman, D. Electroactive Conducting Polymers for Corrosion Control. *J. Solid State Electrochem.* **2002**, *6*, 85–100.

(9) John, A.; Palaniappan, S.; Djurado, D.; Pron, A. One-Step Preparation of Solution Processable Conducting Polyaniline by Inverted Emulsion Polymerization Using Didecyl Ester of 4-Sulfophthalic Acid as Multifunctional Dopant. *J. Polym. Sci. Part Polym. Chem.* **2008**, *46* (3), 1051–1057.

(10) Han, J. A Novel Templateless Method to Nanofibers of Polyaniline Derivatives with Size Control. *J. Polym. Sci. Part Polym. Chem.* **2008**, *46* (2), 740–746.

(11) Wessling, B. Passivation of Metals by Coating with Polyaniline: Corrosion Potential Shift and Morphological Changes. *Adv. Mater.* **1994**, *6*, 226–228

(12) Lu, W.-K.; Elsenbaumer, R. L.; Wessling, B. Corrosion Protection of Mild Steel by Coatings Containing Polyaniline. *Synth. Met.* **1995**, *71*, 2163–2166.

(13) Rohwerder, M.; Michalik, A. Conducting Polymers for Corrosion Protection: What Makes the Difference between Failure and Success? *Electrochim. Acta* **2007**, *53* (3), 1300–1313.

(14) Chen, F.; Nuckolls, C.; Lindsay, S. In Situ Measurements of Oligoaniline Conductance: Linking Electrochemistry and Molecular Electronics. *Chem. Phys.* **2006**, *324*, 236–243

(15) Wei, Y.; Jamasbi, H.; Cheng, S.; Jansen, S. A.; Sein, L. T.; Zhang, W.; Wang, C. Corrosion Protection Properties of Coating of the Epoxy-Cured Aniline Oligomers Based on Salt Spray and UV-Salt Fog Cyclic Tests. *ACS Symp. Ser.* **2003**, *843*, 208–227.

(16) Greiner, M. T.; Festin, M.; Kruse, P. Investigation of Corrosion-Inhibiting Aniline Oligomer Thin Films on Iron Using Photoelectron Spectroscopy. *J. Phys. Chem. C* **2008**, *112*, 18991–19004.

(17) Chowdhury, T.; Mohtasebi, A; Kruse, P. Nature of the Interaction of N'N-Diphenyl-1,4 Phenylenediamine with Iron Oxide Surfaces. *J. Phys. Chem. C* **2016**, *121*, in revision.

(18) Falconer, J. L.; Madix, R. J. Flash Desorption Activation Energies: DCOOH Decomposition and CO Desorption from Ni (110). *Surf. Sci.* **1975**, *48*, 393–405.

(19) Nečas D.; Klapetek, P. Gwyddion: An Open-Source Software for SPM Data Analysis, *Open Phys.* **2012,** *10*, 181-188.

(20) Quillard, S.; Corraze, B.; Boyer, M. I.; Fayad, E.; Louarn, G.; Gerard, F. Vibrational Characterisation of a Crystallised Oligoaniline: A Model Compound of Polyaniline. *J. Molec. Struc.* **2001**, *596*, 33-40.

(21) Quillard, S.; Louarn, G.; Lefrant, S.; Macdiarmid, A. G. Vibrational Analysis of Polyaniline: A Comparative Study of Leucoemeraldine, Emeraldine, and Pernigraniline Bases. *Phys. Rev. B* **1994**, *50*, 12496-12508.

(22) de Santana, H.; Quillard, S.; Fayad, E.; Louarn, G. In Situ UV–Vis and Raman Spectroscopic Studies of the Electrochemical Behavior of N,N'-Diphenyl-1,4-Phenylenediamine. *Synth. Met.* **2006**, *156*, 81-85.

(23) Lindfors, T.; Ivaska, A. Raman Based pH Measurements with Polyaniline. *J. Electroanal. Chem.* **2005**, *580*, 320–329.

(24) Lindfors, T.; Kvarnström, C.; Ivaska, A. Raman and UV–vis Spectroscopic Study of Polyaniline Membranes Containing a Bulky Cationic Additive. *J. Electroanal. Chem.* **2002**, *518*, 131–138.

(25) Jain, M.; Annapoorni, S. Raman Study of Polyaniline Nanofibers Prepared by Interfacial Polymerization. *Synth. Met.* **2010**, *160*, 1727–1732.

(26) Kellenberger, A.; Dmitrieva, E.; Dunsch, L. Structure Dependence of Charged States in "Linear" Polyaniline as Studied by In Situ ATR-FTIR Spectroelectrochemistry. *J. Phys. Chem. B* **2012**, *116*, 4377–4385.

(27) Boyer, M.-I.; Quillard, S.; Rebourt, E.; Louarn, G.; Buisson, J. P.; Monkman, A.; Lefrant, S. Vibrational Analysis of Polyaniline: A Model Compound Approach. *J. Phys. Chem. B* **1998**, *102*, 7382–7392.

(28) Paredes-García, V.; Toledo, N.; Denardin, J.; Venegas-Yazigi, D.; Cruz, C.; Spodine, E.; Luo, Z. One Pot Solvothermal Synthesis of Organic Acid Coated Magnetic Iron Oxide Nanoparticles. *J. Chil. Chem. Soc.* **2013**, *58*, 2011–2015.

(29) Cochet, M.; Louarn, G.; Quillard, S.; Boyer, M. I.; Buisson, J. P.; Lefrant, S. Theoretical and Experimental Vibrational Study of Polyaniline in Base Forms: Non-Planar Analysis. Part I. *J. Raman Spectrosc.* **2000**, *31* (11), 1029–1039.

(30) Gawlicka-Chruszcz, A.; Stadnicka, K. A Comparative Study of Intermolecular Interactions in the Crystal Structures of Phenyl/phenyl End-Capped Oligoanilines. *Acta Crystallogr. C* **2002**, *58* (7), 0416–0420.

(31) Barth, J. Transport of Adsorbates at Metal Surfaces: From Thermal Migration to Hot Precursors. *Surf. Sci. Rep.* **2000**, *40*, 75-149.

(32) Li, S.; Chu, L.; Gong, X.; Diebold, U. Hydrogen Bonding Controls the Dynamics of Catechol Adsorbed on a TiO2(110) Surface. *Science* **2010**, *328*, 882-884.

(33) Wang, X.; Kim, S.; Buda, C.; Neurock, M.; Koper, O. B.; Yates, J. T. Jr. Direct Spectroscopic Observation of the Role of Humidity in Surface Diffusion through an Ionic Adsorbent Powder. The Behavior of Adsorbed Pyridine on Nanocrystalline MgO. *J. Phys. Chem. C* **2009**, *113*, 2228-2234.

(34) Shi, J.; Qin, X. R. Nucleation and Growth of Tetracene Films on Silicon Oxide. *Phys. Rev. B* **2008**, *78*, 115412.

Table of Contents (TOC) Graphic

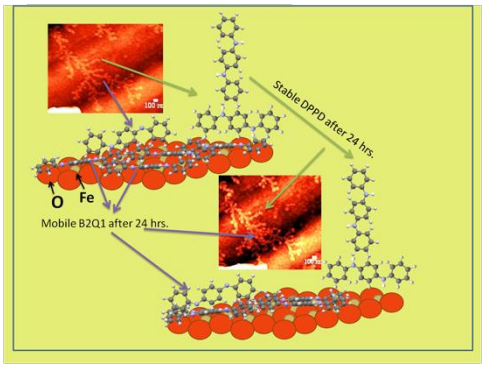

CHAPTER -5
INTERACTIONS OF DIFFERENT REDOX STATES OF PHENYL-CAPPED ANILINE TETRAMERS WITH IRON OXIDE SURFACES AND CONSEQUENCES FOR CORROSION INHIBITION.

Tanzina Chowdhury,[1] *Amirmasoud Mohtasebi,*[1] *Svetlana Kostina,*[1] *Xiangrong Zhang,*[2] *Joseph R. Kish*[2] *and Peter Kruse*[1,*]

[1]Department of Chemistry and Chemical Biology, McMaster University, 1280 Main Street West, Hamilton, Ontario L8S 4M1, Canada.

[2]Department of Materials Science and Engineering, McMaster University, 1280 Main Street West, Hamilton, Ontario L9H 4L7, Canada.

ABSTRACT: The phenyl capped aniline tetramer (PCAT) is known for its redox properties and is being studied for its ability to inhibit corrosion of iron and steel in addition to being of interest for sensors and molecular electronics. Here we investigate the interactions, orientation and corrosion inhibition ability of the fully reduced or leucoemeraldine base, the half oxidized or emeraldine base, and the fully oxidized or pernigraniline base forms of PCAT with iron oxide surfaces. Raman spectroscopy demonstrates interconversion of these molecules to one another due to charge transfer to the surface. Polarized mid-IR spectroscopy and atomic force microscopy were used to elucidate the molecular orientations on the surface. Electrochemical impedance spectroscopy shows the corrosion resistance of a B5 coating on low carbon steel to be higher than that for B4Q1 and B3Q2 coatings. A weight loss test, laser line measurements

and Raman spectroscopy reveal that even though B4Q1 initially shows a lower corrosion resistance due to transformation into B3Q2, with time it transforms back into B4Q1 and protects the surface. B3Q2 molecules show opposite behavior, causing the degradation of the surface over time. We thus attained a deeper insight into the interplay of the different oxidation states for corrosion control.

* To whom correspondence should be addressed. Email: pkruse@mcmaster.ca. Phone: +1 (905) 525-9140 ext. 23480. Fax: +1 (905) 522-2509.

5.1 INTRODUCTION

Polyaniline (PANI) is a prominent member of the conducting polymer family because of its diverse application in biosensors,[1] electrochromic devices,[2] fuel cells,[3,4] etc. One of the most studied applications of this polymer is corrosion inhibition of metals. DeBerry showed in 1985 that PANI can inhibit corrosion of iron and steel by passivating the surface in acidic media.[5,6,7] Similarly to the native oxides, the passive oxides on iron or steel maintain a layered structure of a fully oxidized outer layer, followed by an intermediate mixed iron (II) and iron (III) oxide layer transitioning to a very thin inner iron (II) oxide layer next to the bulk metal. PANI is mainly found in three different stable oxidation states (fully reduced or leucoemeraldine, half-oxidized or emeraldine, and fully oxidized or pernigraniline) and several protonation states. The complete mechanism behind the corrosion inhibition ability of this polymer is still unclear due to its complex chemistry. PANI coatings can break down catastrophically, which is the reason why their commercialization has failed. Recent work demonstrated that this breakdown happens

due to a high conductivity and long-range electronic interactions, which are therefore undesirable for a corrosion inhibiting coating, even though they were originally thought to be germane to the inhibition mechanism.[8] Oligoanilines do not share certain drawbacks intrinsic to PANI coatings (e.g. catastrophic failure, poor solubility). Very little work has been done on oligoanilines which have related physical and chemical properties.

We have chosen the phenyl-capped aniline tetramer (PCAT, 4-(phenylamino)phenyl-1,4-benzenediamine) for a detailed investigation of its interactions with iron oxide surfaces because it is the simplest aniline oligomer to fully mimic the redox properties of PANI. PCAT coatings have been shown to improve the corrosion resistance of steel with the remarkable property of withstanding mechanical damage to the coating.[9,10] PCAT fully mimics the electronic behavior of PANI in that it can also exist in three different oxidation states [B5 (fully reduced), B4Q1 (half oxidized) and B3Q2 (fully oxidized)] (Figure 5.1) and several protonation states (unprotonated, semiquinone and monoprotonated). It has been suggested that the inter-conversion between different oxidation states is at the core of corrosion inhibition by PCAT.[9] Moreover, the self-healing properties of PCAT also make it more interesting than a simple barrier protector like a conventional coating (i.e. paint) but the nature of the interactions of these molecules with the (hydrated, native) iron oxide surface is not entirely clear. We have previously looked at the interactions of the reduced base form of PCAT with native iron oxide films, but an understanding of the interplay between the oxidation states was lacking.[11] Recently we have demonstrated that the oxidation state of PCAT has an impact on the amount of charge transfer to underlying substrates, but the molecular orientation at the interface and the impact of interfacial structure on corrosion inhibition performance remained unclear.[12,13]

Here we investigate the interactions of B5, B3Q2, and B4Q1 with iron oxide surfaces using Raman, mid-IR, and visible spectroscopy. Atomic force microscopy (AFM) and mid-IR spectroscopy are used to investigate the orientations of all these forms of PCAT on the iron oxide surface. The corrosion inhibition properties were studied using electrochemical impedance spectroscopy (EIS) and weight loss measurements. Our focus is to elucidate the nature of the interaction of the different oxidation states of these oligomers with iron oxide surfaces and determine their capability for corrosion inhibition. The results of our work will aid in the establishment of rational design criteria for smart protective coatings.

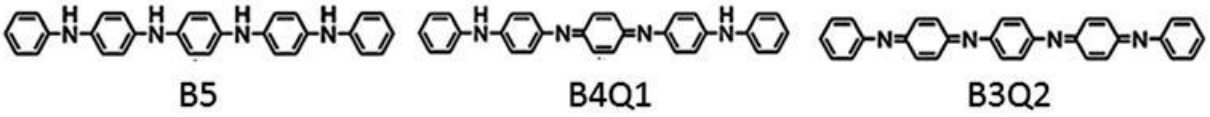

Figure 5-1. Fully reduced (B5), half oxidized (B4Q1) and fully oxidized (B3Q2) form of Phenyl capped aniline tetramer.

5.2 EXPERIMENTAL DETAILS

Low carbon steel (~0.05% Mn, ~0.07% Cr, ~0.01% Si, ~0.05% Al, balance Fe) was obtained from ArcelorMittal Dofasco. The steel sheet was cut into coupon sizes of 1 cm × 1 cm, except for 2.5 cm × 2.5 cm sample coupons for electrochemical impedance spectroscopy. These steel coupons were mechanically polished with an automatic polisher by first using coarse grit silicon carbide emery paper then followed by 3 µm and 1 µm diamond particle emulsion combined with lubricating solution (25% propylene glycol and 75% ethanol). The final polishing step for all samples except those for the EIS test was 0.05 µm colloidal silica. All samples were then

washed with water and ultrasonically cleaned with acetone and methanol. Iron (III) oxide (α-Fe_2O_3) nanopowder was obtained from Sigma-Aldrich. Its particle size is below 50 nm, with a surface area of 16 mg/m^2.

B5 powder was synthesized according to a literature procedure.[14] The fully oxidized form of PCAT (B3Q2) powder was prepared by first mixing reduced B5 powder with ammonium persulphate (reagent grade 98%, Sigma-Aldrich) (B5 : ammonium persulphate molar ratio of 1:2.1), then dissolving in methanol and stirring for 24 hours. After evaporation of the methanol, the dried product was washed with DI water several times to remove ammonium persulphate and vacuum suctioned. The wet powder is then dissolved in 0.1 M NH_4OH and again stirred for 24 hours to obtain the free base of B3Q2. The residue was then washed with 0.05 M of NH_4OH and dried in a desiccator. To obtain the half-oxidized form of PCAT (B4Q1), a B5 : ammonium persulphate molar ratio of 1:1.04 was used, following the same procedure as for preparation of the oxidized form. To obtain the fully reduced form of the PCAT, ascorbic acid was used, with a B5 : ascorbic acid molar ratio of 1:3.2, following otherwise the same procedure as for making the oxidized form.

Raman spectroscopy is performed using a Renshaw InVia Raman microscope with a 514.5 nm green laser (1 μm spot size, 5-10% laser power). Raman spectroscopy was used to characterize all forms of pure PCAT powder, powder mixtures of all individual three forms of PCAT with α-Fe_2O_3 powder and drop cast samples of all three forms from methanol onto steel coupons.

The interactions with the surface, as well as the orientations of these different forms of PCAT molecules, were mapped by mid-IR spectroscopy at the Canadian Light Source in

Saskatoon. The endstation used for this purpose was a Bruker Vertex 70v/S spectrometer with a Hyperion 3000 microscope (online system), equipped with a 100 micron size single element MCT detector and a 64x64 pixel focal plane (with beamline) array detector. A grazing incidence of reflection (GIR) objective was used to observe thin films of these molecules on steel surfaces. 90˚ and 0˚ polarizers were used with the GIR objective to study molecular orientations. For mapping, the molecules were vacuum deposited on one-half of the steel coupon and the other half was kept clean using a tantalum shadow mask. The deposition temperatures for B5 (25 nm film), B3Q2 (16.2 nm film) and B4Q1 (10.5 nm film) were 10˚C, 24˚C and 11˚C, respectively.

In a home built stainless steel vacuum deposition chamber molecules were evaporated from a glass crucible onto the steel coupons. The chamber was pumped oil-free to a base pressure better than 2×10^{-6} Torr. The deposition coverage was measured using a quartz crystal microbalance.

AFM was performed using a Veeco Enviroscope with a Nanoscope IIIa controller and Veeco RTESPA phosphorus (n) Si tips with nominal radii of 10 nm or less. The AFM images were analyzed using Gwyddion data analysis software.[15] The height resolution of the AFM data is 0.06 nm. Three different organic film thicknesses were vacuum deposited for step height analysis: B5 (~2.5 nm at 20˚C), B4Q1 (~1 nm at 20˚C) and B3Q2 (~1.5 nm at 24˚C).

Electrochemical measurements were carried out using a 1287 Solartron potentiostat coupled to a 1252 Solartron frequency response analyzer for electrochemical impedance spectroscopy (EIS) measurements. A Paracell of flat specimen is used for this experiment which is designed for mounting flat and large samples on either end of the cell for experiments. In that

electrochemical cell, steel coupons with coatings of different forms of PCAT were used as a working electrode with a platinum counter electrode and a calomel (SCE) reference electrode. EIS spectra were recorded after the working electrode was conditioned at the corrosion potential for 2 h. The EIS experiments were carried out in the frequency range from 0.01 Hz to 100 kHz with an AC excitation potential of 10 mV in a 3.5% NaCl solution. The experimental time varied from 5 hrs (2 cycles, 1 cycle = 2 hrs) to 48 hrs (24 cycles) for fresh and week old coated samples. The exposed area of each sample was 2.85 cm^2. Data was recorded and analyzed using Corrware and Zplot software (Scribner Associates).

Optical surface profiler (OSP) was used to measure the surface roughness of the corroded samples in the EIS experiment. The measurement was done in the M470-OSP instrument with laser spot size of ~30 μm. The line scan was taken across the centre of the circle in each sample.

5.3 RESULTS AND DISCUSSION

Characterization of Different Forms of PCAT

Raman spectra of different oxidation states of PCAT were recorded for comparison with the species that will arise from the interactions with iron (III) oxide surfaces. Raman spectra of B5, B3Q2, and B4Q1 powders are shown in Figure 5.2. The intense Raman bands at 1623 cm^{-1} (Figure 5.2b) of B5 and at 1617 cm^{-1} (Figure 5.2c) of B4Q1 were attributed to C-C stretching of the benzene rings while the band of B3Q2 (Figure 5.2a) at 1619 cm^{-1} is a shoulder of another band at 1585 cm^{-1} .[16] The bands at 1515 cm^{-1} and 1496 $cm^{-1}$of B3Q2 and B4Q1, respectively are due to a combination band of C═N stretching and C-H bending. The band of B4Q1 at around 1585 cm^{-1} is due to C═C stretching of the quinoid ring.[10] The three bands at 1164, 1163 and

1181 cm^{-1} of B3Q2, B4Q1, and B5, respectively are assigned to C-H bending at the quinoid ring (first two) and a benzene ring (last band).[10] Three other bands at 1215 (B3Q2), 1223 (B5) and 1206 cm^{-1} (shifted, B4Q1) arise due to C-N stretching. The two bands at 996 and 1030 cm^{-1} that only arise in B5 are attributed to ring deformation of benzene.[10]

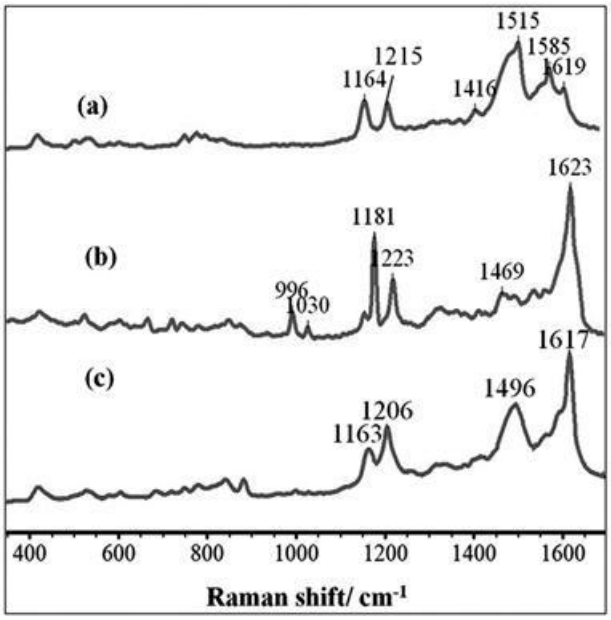

Figure 5-2. Raman spectra of the powder form of (a) B3Q2, (b) B5 and (c) B4Q1.

Interactions of B5, B3Q2, and B4Q1 with α-Fe_2O_3 Surfaces

The species that arise from the interactions of different forms of PCAT with iron oxide surfaces and with methanol were investigated. Figure 5.3a shows a Raman spectrum of B5 drop cast from methanol onto a glass substrate. When compared to the Raman spectrum of pure powder B5 in Figure 5.2b, even though almost all the bands are slightly red-shifted all spectroscopic features of the molecules remain the same. This means that the B5 molecules did

not change oxidation state upon interaction with methanol. The Raman features of a methanolic solution of B5 drop cast onto a steel substrate (native oxide) in Figure 5.3b are different from B5 in MeOH (Figure 5.3a) or pure powder B5 (Figure 5.2b). The Raman bands at 1002 cm^{-1} (ring deformation), 1335 cm^{-1} (C-$N^{+\bullet}$ stretching) and 1407 cm^{-1} (C-$N^{+\bullet}$ stretching) in this spectrum (Figure 5.3b) are assigned to semiquinone species.[17,18,19] The band at 1636 cm^{-1} can be assigned to a radical cation species that formed.[17] The other bands at 1603 cm^{-1}, 1567 cm^{-1} and 1496 cm^{-1} (very weak) of the same spectrum arise due to C-C stretching of the benzene ring, C=C stretching of the quinoid ring and C=N stretching, respectively.[16] The first band corresponds to B5, the second and third one are indications of B5 tending to transform into B3Q2 and also B4Q1 by contact with the native oxide of steel in methanolic solution.

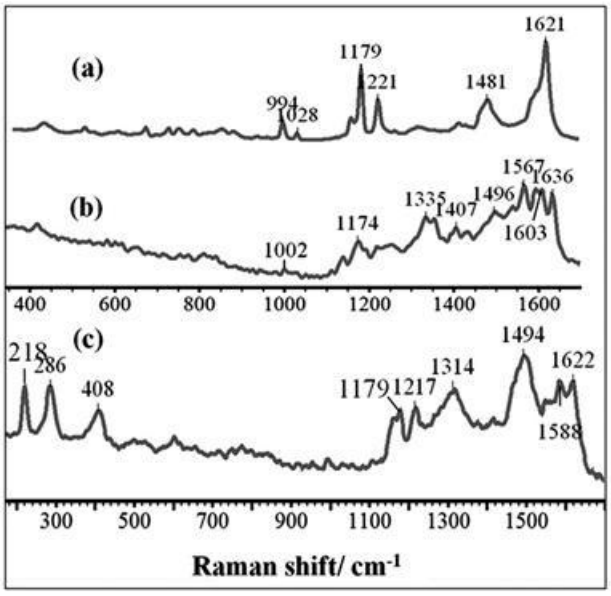

Figure 5-3. Raman spectra of powder of (a) B5 in methanol, (b) B5 on a native oxide covered steel substrate, and (c) B5 in Fe_2O_3 powder mixture

Figure 5.3c shows the Raman spectrum of a B5 and α-Fe_2O_3 powder mixture, which had no contact with methanol. This spectrum has Raman bands at 1622, 1179, 1217, and 1314 cm^{-1} which are almost the same features as in Figure 5.3a, corresponding to B5.[16] On the other hand, the two bands at 1494 cm^{-1} (very intense, C═N stretching and C-H bending) and 1588 cm^{-1} (C═C stretching of quinoid ring) correspond to B4Q1.[16] This same spectrum also has bands at 218, 286 and 408 cm^{-1}, which can be assigned to hematite (α-Fe_2O_3) but are a little bit shifted.[20] These results suggest that B5 does not change oxidation state in methanol itself but there is interaction as a result of drop casting B5 in methanol on the steel surface. This interaction is between B5 and native oxide of iron (α-Fe_2O_3) which converts most of the B5 molecules into the semiquinone form, and a very small portion also into the B3Q2 (fully oxidized) and B4Q1 (half oxidized) forms. These results suggest that hydroxyl groups on the iron oxide surface and from methanol are playing a role of in the hydrogen bonding of B5 with iron oxide surfaces to produce semiquinone, B3Q2 and B4Q1 species. In the absence of methanol, the B5 molecules tend to transform into B4Q1 (half oxidized).

In order to systematically understand the interactions of different oxidation states of the phenyl-capped aniline tetramer, we next looked at B4Q1 (half oxidized). Figure 5.4a shows a Raman spectrum of B4Q1 drop cast from methanol onto a glass substrate, while Figure 5.4b shows a Raman spectrum of B4Q1 drop-cast from methanol onto a steel substrate (native oxide) and Figure 5.4c shows a Raman spectrum of B4Q1 in the α-Fe_2O_3 powder mixture. There are substantial differences between the Raman spectrum of B4Q1 cast from methanol onto a glass substrate (Figure 5.4a) and the Raman spectrum of pure powder B4Q1 (Figure 5.2c). The intensity of the bands at 1617, 1496, and 1163 cm^{-1} (Figure 5.2c) decreased and shifted to 1635,

1498 and 1180 cm^{-1}, respectively (Figure 5.4a). New bands arise at 1335 and 1568 cm^{-1}. The Raman bands at 1335 and 1635 cm^{-1} are assigned to the semiquinone species.[17,18,19,21] The band at 1498 cm^{-1} still belongs to B4Q1 but the bands at 1568 and 1180 cm^{-1} are an indication that B4Q1 tends to transform into the fully oxidized form (B3Q2) upon exposure to methanol. It means that B4Q1 molecules change their oxidation states in part to semiquinone and in part to B3Q2 through interaction with methanol.

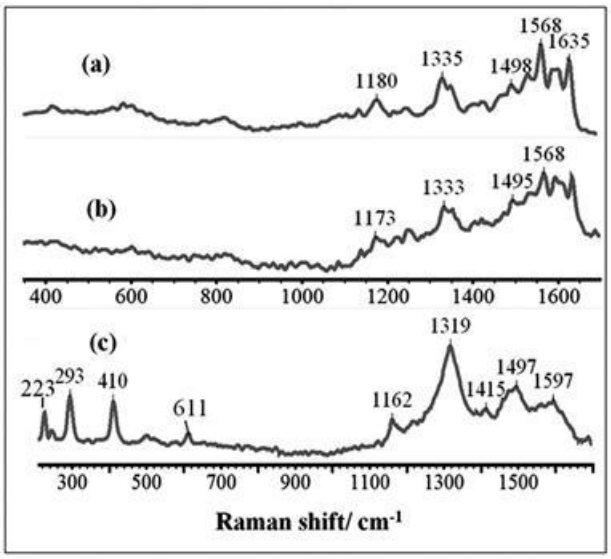

Figure 5-4. Raman spectra of B4Q1 (a) in methanol, (b) on steel substrate (native oxide Fe_2O_3) and (c) in the α-Fe_2O_3 powder mixture.

The Raman spectrum of B4Q1 drop cast from methanol onto a native oxide covered steel substrate (Figure 5.4b), looks similar to the Raman spectrum of B4Q1 in MeOH (Figure 5.4a), indicating that B4Q1 molecules interact in a similar way with iron oxide surfaces as with methanol, or are prevented from interacting with iron oxide surfaces in the presence of methanol. Figure 5.4c shows the Raman spectrum of a powder mixture of B4Q1 and α-Fe_2O_3 which did not have contact with methanol. The Raman bands at 1162 cm^{-1} and 1497 cm^{-1}

correspond to B4Q1 and the bands at 1415 cm^{-1} (C-C stretching of the quinoid ring) and at 1597 cm^{-1} (C-C stretching of benzene ring) correspond to B3Q2 and B5, respectively.[16] The band at 1319 cm^{-1} (C-$N^{+\bullet}$ stretching) corresponds to semiquinone species.[17,21] This same spectrum has bands at lower wavelengths 223, 293, 410 and 611 cm^{-1}, all these bands are assigned to hematite (α-Fe_2O_3).[20] These results suggest that B4Q1 molecules at α-Fe_2O_3 surfaces tend to transform into a mixture of semiquinone, B5 and B3Q2 forms in the absence of methanol. On the other hand, methanol itself transforms B4Q1 mostly into the semiquinone form and partially into the B3Q2 form. As a result, when drop-casting B4Q1 in MeOH on a steel substrate, B4Q1 does not significantly interact with the native iron oxide of steel and does not form any detectable films via dip coating.

The interaction of the fully oxidized form of the phenyl-capped aniline tetramer (B3Q2) with iron oxide surfaces was also observed in the same fashion as the other two oxidation states. Figure 5.5a shows a Raman spectrum of B3Q2 drop cast from methanol onto a glass substrate, Figure 5.5b shows a Raman spectrum of B3Q2 drop-cast from methanol onto a steel substrate (native oxide), and Figure 5.5c shows a Raman spectrum of B3Q2 in a dry powder mixture with α-Fe_2O_3. The Raman spectrum of B3Q2 drop cast from methanol onto a glass substrate (Figure 5.5a) differs from the Raman spectrum of pure powder B3Q2 (Figure 5.2a). The bands at 1585, 1416, 1215 and 1164 cm^{-1} (Figure 5.2c) are shifted to higher wavenumbers at 1591, 1419, 1218 and 1167 cm^{-1}, respectively (Figure 5.5a). All these bands still belong to B3Q2. New bands arise at 1142, 1407 and 1500 cm^{-1}. The band at 1407 cm^{-1} is assigned to the semiquinone species.[17] The bands at 1142 cm^{-1} (C-H bending quinoid) and 1500 cm^{-1} (C=N stretching) belong to B4Q1.[16,18] This means that in methanol a portion of fully oxidized (B3Q2) molecules

change their oxidation states to the half-oxidized form (B4Q1) and to a smaller extent into the semiquinone form.

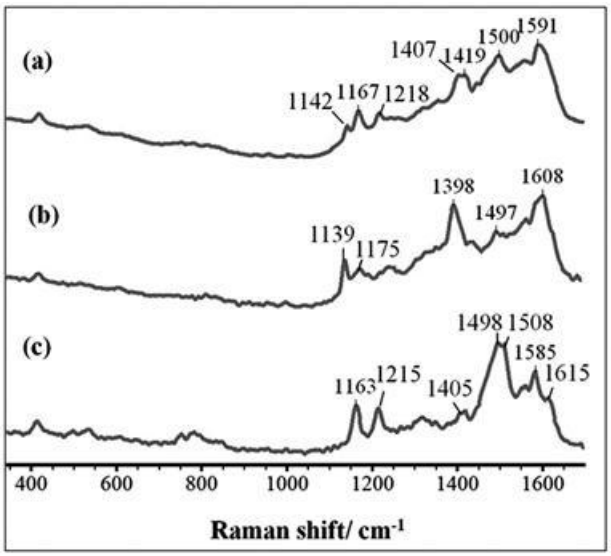

Figure 5-5. Raman spectra of B3Q2 (a) in methanol, (b) on steel substrate (native oxide) and (c) in the α-Fe_2O_3 powder mixture.

The bands in the Raman spectrum in Figure 5.5b of B3Q2 drop cast onto a steel substrate (native oxide) are shifted but show the same interaction as B3Q2 in MeOH (Figure 5.5a). The bands at 1139 cm^{-1} (C-H bending of Q), 1497 cm^{-1} (C=N stretching), and 1608 cm^{-1} (C-C stretching of benzene ring) correspond to B4Q1.[16,18] The band at 1398 cm^{-1} is assigned to the semiquinone species.[21] B3Q2 molecules tend to convert into B4Q1 and partially into the semiquinone form by interacting either with iron oxide or with methanol.

Figure 5.5c shows the Raman spectrum of a B3Q2 and α-Fe_2O_3 dry powder mixture, which has had no contact with methanol. This spectrum has a very weak semiquinone band at 1405 cm^{-1} and intense bands belonging to B4Q1 at 1498 cm^{-1} and 1508 cm^{-1} (C=N stretching).[16,17] The rest of the bands belongs to B3Q2.[16] We conclude that in the absence of methanol, a

portion of the B3Q2 molecules tends to transform into B4Q1 and into the semiquinone form upon interaction with iron oxide. On the other hand, methanol itself transforms a portion of B3Q2 molecules into the semiquinone form and into the B4Q1 form. When drop-casting methanolic B3Q2 solution onto a steel substrate, B3Q2 is not significantly changed any further through interaction with the native iron oxide of steel.

In summary, we have looked at the interactions of the B5, B4Q1, and B3Q2 forms of PCAT with iron oxide surfaces as a first step towards understanding the corrosion inhibition mechanism of these molecules. Methanol is found to be a suitable solvent for B5 molecules because it does not change their oxidation state. As a result, B5 molecules can strongly interact with the native oxide and adhere to the surface, which is beneficial for corrosion inhibition. After drop casting the molecules transform mostly into the semiquinone form and B4Q1, and to a smaller extent into B3Q2. On the other hand, the powder mixture of B5 and α-Fe_2O_3 shows very little interactions and this turns only a very small amount of B5 into B4Q1 but the rest remains as B5. We have also found that methanol not only changes the oxidation states of B4Q1 and B3Q2 but also hinders the interactions between the native oxides of steel surface and these two molecules. B4Q1 turns into the semiquinone form and B3Q2 after dissolving in methanol. Drop-casting that solution onto steel surfaces results in interactions comparable to those with methanol. The lower intensity of the molecular bands of this sample is also an indication of less interaction with the surface. In the dry powder mixture of B4Q1 and α-Fe_2O_3 nanoparticles, however, B4Q1 transforms mostly into B5 by interacting with α-Fe_2O_3. B3Q2 exhibited similar interactions with both methanol and native oxides of steel surfaces (α-Fe_2O_3). In both cases, B3Q2 transforms into the semiquinone and B4Q1 forms. Drop-cast B3Q2 also showed fewer

Raman bands which are an indication of weak bonding interaction with the surface. B3Q2 in a powder mixture with Fe_2O_3 transformed into both the semiquinone and the B4Q1 forms as a result of the interactions. Powder mixtures showed indications of stronger bonding than drop cast samples.

Orientation of B5 on Native Iron Oxide Surfaces

After elucidating the interactions of different oxidation states of PCAT with iron oxide surfaces, we can now turn our attentions towards the orientation of these molecules at these surfaces. We start by investigating B5 using synchrotron-based mid-IR spectromicroscopy. For this experiment, B5 was vacuum deposited on one-half of a steel coupon and the other half was kept clean using a tantalum shadow mask. Figure 5.6A (a-d, left image) shows the IR mapping spectra of B5 from the deposited film towards the clean part at $\theta_E = 0^\circ$ and the right image, Figure 5.6B (a-d, right image) shows the spectra on the same spots (a-d) at $\theta_E = 90^\circ$. These spectra in Figures 5.6A and 5.6B correspond to the points (a-d) shown on the bottom optical image of the sample in Figure 5.6C. The black 'T' shape (vertical and horizontal) line represents a mechanical scratch made on the sample to visually separate the deposited area and the clean part as shown in Figure 5.6C. The 3 points on the left side of the black line [Figure 5.6C (a - c)] are points on the B5 molecular film and 1 point on the right side of the black line [Figure 5.6C (d)] is on the clean side. A grazing incident ($\theta = 80^\circ$ to the surface normal) objective in reflection geometry was used to take the spectra. Two polarizer orientations, $\theta_E = 0^\circ$ and $\theta_E = 90^\circ$ were used to study the orientation of the molecules. With the polarizer orientation $\theta_E = 0^\circ$, the electric field of the polarized light was parallel to the substrate surface and with the

polarizer orientation, $\theta_E = 90^\circ$ it was perpendicular to the substrate surface. IR bands can be divided into two regions: Out-of-plane ring vibrations mostly below 1000 cm^{-1} and in-plane ring vibrations in the range of 1000 – 1700 cm^{-1}.[22] The intensity ratio between these two regions of vibrations can be used to determine the orientation of the molecules on the surface.[22] In case of B5 molecules, the two bands that were taken into account for orientation calculations are 1529 cm^{-1} and 836 cm^{-1}. The band at 1529 cm^{-1} is assigned to the C-H in-plane bending vibration and the band at 836 cm^{-1} is the C-H out of plane wag of the mono-substituted benzene ring.[16,23]

All the intensity ratios for $\theta_E = 90°$ and $\theta_E = 0°$ for the bands at 836 cm^{-1} and 1529 cm^{-1} are gathered in Table 5.1. On the molecular film region (left side of the line) the band at 1529 cm^{-1} is very prominent for $\theta_E = 90°$ but the band 836 cm^{-1} is just a shoulder of another band in Figure 5.6B, whereas for $\theta_E = 0°$ both bands are prominent. Three spectra are shown of three points on

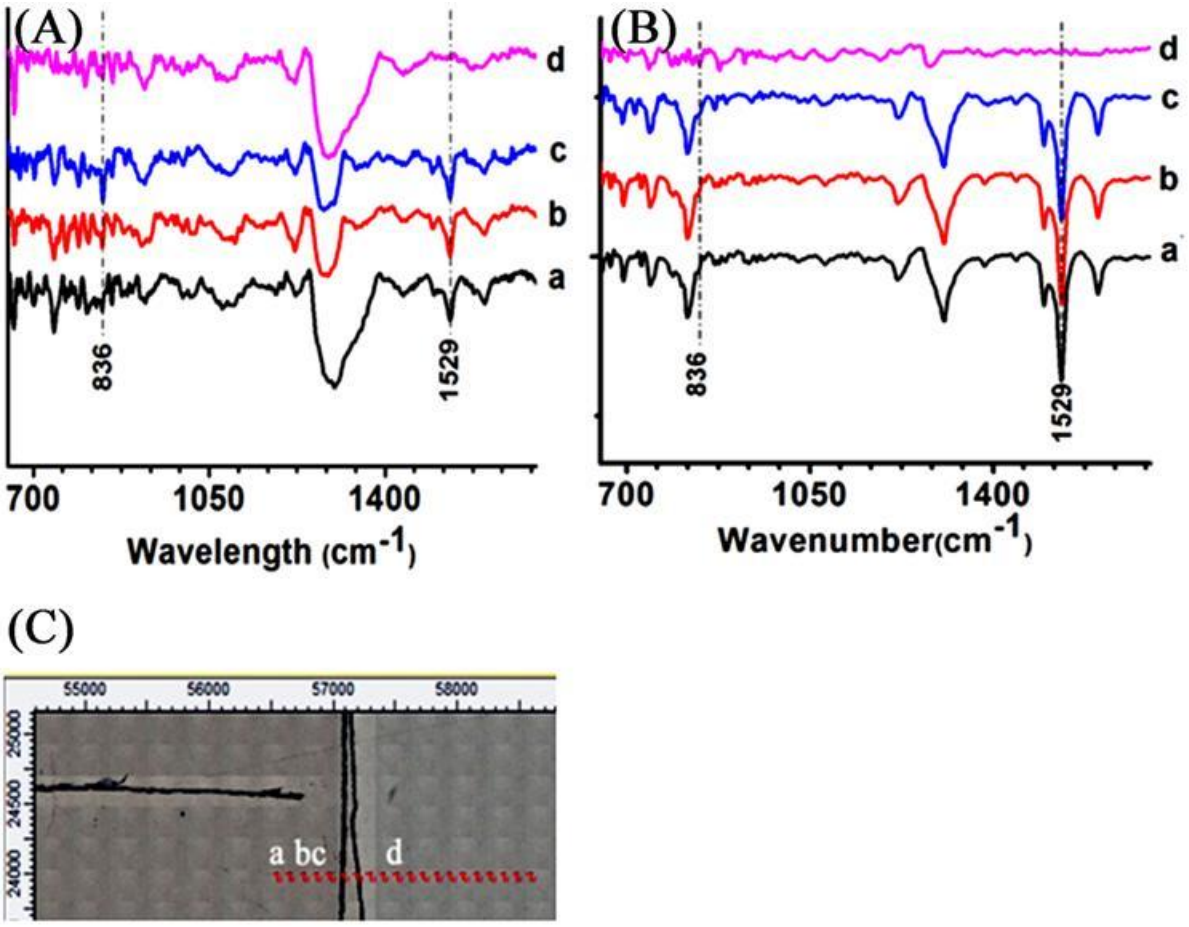

Figure 5-6. Mid-IR mapping spectra of B5 on steel substrate (A) at $\theta_E = 0^\circ$ (upper left) and (B) $\theta_E = 90^\circ$ (upper right). (C) The IR spectrum (a-d) represents the point from molecules side to clean side. These points are shown in the optical image map at the bottom. The spacing between sample points (red marks) is 100 µm, for a total cross-section length of about 2 mm.

the molecular side and one on the clean side. The presence of the molecules on the clean side at point (d) in Figure 5.6 A-C is a result of migration of some molecules during or after deposition. The intensity ratios (836 cm^{-1}/1529 cm^{-1}) in Table 1 show that the ratio for $\theta_E = 90^\circ$ is very low in comparison to the ratio for $\theta_E = 0^\circ$ on the organic film (points a - c). It can also

seen that the overall ratio (836 cm^{-1}/1529 cm^{-1}) individually for $\theta_E = 90^\circ$ and $\theta_E = 0^\circ$ increases as the film is getting thinner. A lower ratio means that the molecules are standing on their edge or standing up on the surface as opposed to lying down.[22] Due to the high coverage of molecules in this region, the dominant interactions are between molecules rather than with the surface. On the other hand, on the clean region the point (d) for $\theta_E = 90^\circ$ shows an increase in ratio and on the same point for $\theta_E = 0^\circ$ the ratio drops. This is an indication that the orientation of the molecules changes the clean region. Due to the very low coverage of migrated molecules in the clean region, these molecules have close interactions with the iron oxide surface. According to the ratios, these B5 molecules are lying down on the surface.[22] B5 molecules very close to the surface may also partially be standing on their edges but a twisted backbone of the molecule still leads to its identification as lying down in the IR spectra.

Table 5-1: Intensity ratio of the selected IR absorption bands for $\theta_E = 0^\circ$ and $\theta_E = 90^\circ$ of B5.

	836 cm^{-1}/1529 cm^{-1} for $\theta_E = 90^\circ$	836 cm^{-1}/ 1529 cm^{-1} for $\theta_E = 0^\circ$
1st point (a) of the mapping image.	0.13	0.78
3 rd point (b)	0.14	0.81
4th point (c)	0.16	0.99
10th point (d) after the molecular edge	5.99	0.13

Orientation of B3Q2 on Native Iron Oxide Surfaces

For investigating the orientation of B3Q2 molecules on iron oxide surfaces, the two bands that were considered are 1529 cm^{-1} and 852 cm^{-1}. Figure 5.7A (a-g, left image) shows the IR mapping spectra of B3Q2 from the deposited film to towards the clean part at $\theta_E = 0^\circ$ and Figure 5.7B (a-g, right image) shows the spectra on the same spots (a-g) at $\theta_E = 90^\circ$. These spectra in Figures 5.7A and 5.7B correspond to the points (a-g) shown on the bottom optical image of the sample in Figure 5.7C. The band at 1529 cm^{-1} is assigned to C=N stretching and C-H in-plane bending vibration and the band at 852 cm^{-1} is the C-H out of plane wag of the para-substituted benzene ring.[16,23]

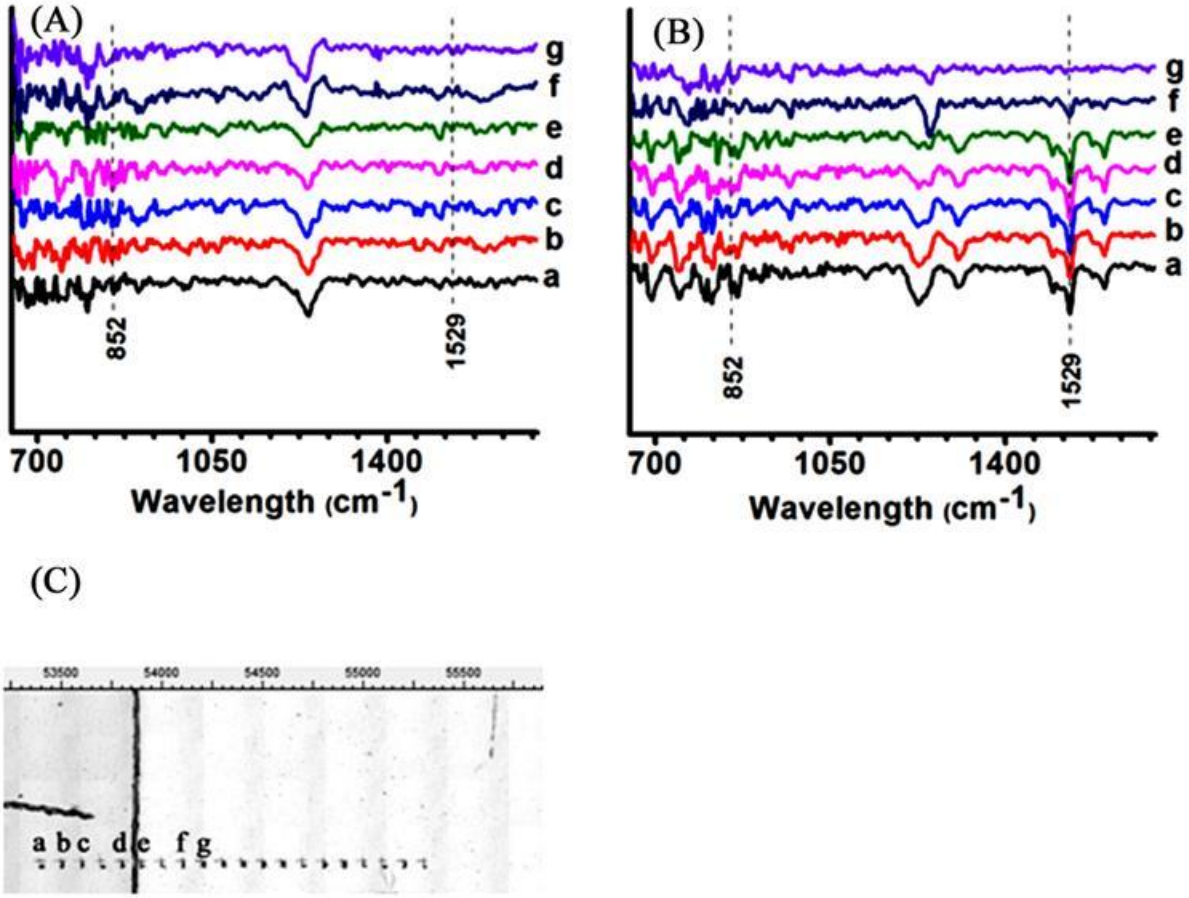

Figure 5-7. Mid-IR mapping spectra of B3Q2 on steel substrate, (A) at $\theta_E = 0^\circ$ (upper left) and (B) $\theta_E = 90^\circ$ (upper right). (C) The IR spectrum (a-g) represents the point from molecules side to clean side. These points are shown in the optical image map at the bottom. The spacing between sample points (black marks) is 100 µm, for a total cross-section length of about 2 mm.

The intensity ratios between the bands at 852 cm^{-1} and 1529 cm^{-1} for $\theta_E = 90^\circ$ and $\theta_E = 0$ are shown in Table 5.2. Four spectra are shown of four points on the organic film side (left side of the vertical line) [points (a-d) in Figures 5.7A and 5.7B] and three spectra of three points (e-g) on the clean side (right side of the vertical line). The presence of a spectral signature of the

molecules on the clean side is an indication of molecules migration during or after deposition [points (e-g) in Figures 5.7A-C].

Table 5-2: Intensity ratio of the selected IR absorption bands for $\theta_E = 0^\circ$ and $\theta_E = 90^\circ$ of B3Q2.

	$852cm^{-1}/1529\ cm^{-1}$ for $\theta_E = 90^\circ$	$852cm^{-1}/1529\ cm^{-1}$ for $\theta_E = 0^\circ$
1st point (a) of the mapping image.	0.55	2.21
2nd point (b)	0.38	3.19
3rd point (c)	0.32	4.31
5th point (d)	0.50	4.02
6th point (e) after the molecular edge	0.46	0.58
8th point (f)	0.34	2.55
9th point (g)	4.18	2.05

Table 5.2 shows that the overall intensity ratios for $\theta_E = 90^\circ$ are very low in comparison to the intensity ratios for $\theta_E = 0^\circ$ on the molecular films (points a - d). This lower intensity ratio means that the molecules are more aligned with the electric field for $\theta_E = 90^\circ$ than $\theta_E = 0^\circ$. This is an indication of B3Q2 molecules are lying on their edge or standing up when they are interacting with each other because the side of the molecular film has a higher coverage of molecules. On the molecular film there is a variation in ratios for both $\theta_E = 90^\circ$ and $\theta_E = 0^\circ$ in

different points from (a-d), likely due to inhomogeneities in the film thickness. On the clean region, the first point (e), almost on the vertical line shows a low ratio for $\theta_E = 0^\circ$ but still higher than for $\theta_E = 90^\circ$. This huge drop is probably due to defects created by the scratch (vertical line). The point (f) on the clean side also shows the presence of molecules and the same ratio trend as on the molecular film (low ratio for $\theta_E = 90^\circ$ and higher for $\theta_E = 0^\circ$). It means that up until this point there exists a multilayer of B3Q2 molecules, and they are also oriented the same as the other two forms of PCAT. On the other hand, point (g) marks the furthest distance from the deposited film at which evidence of B3Q2 molecules is observed. Here we see an increase in the intensity ratio for $\theta_E = 90^\circ$ and a decrease in the ratio for $\theta_E = 0^\circ$. This suggests that during interaction with the iron oxide surface the B3Q2 molecules are oriented either lying down or standing on their edge with a twisted chain. IR spectroscopy makes it is possible to differentiate between standing up and lying down orientations, but not necessarily between molecules that are lying down or are twisted while standing on their edge. While there is a significant difference between the standing up film layer thickness (2.2 nm) and the other two orientations (lying down at 0.44 nm or standing on their edge at 0.57 nm), the lying down and standing on their edge orientations are very close to each other in layer thickness. Furthermore, the transition between lying face-on and standing on edge is fluent, given the possibility of twisted molecular geometries and tilted orientations.

Orientation of B4Q1 on Native Iron Oxide Surfaces

For B4Q1 molecules on an iron oxide surface, the intensity ratio was obtained for the two bands at 1531 cm^{-1} (shifted) and 817 cm^{-1}. Figure 5.8A (a-e, left image) shows the IR mapping spectra of B4Q1 from the deposited film towards the clean part at $\theta_E = 0^\circ$ and Figure 5.8B (a-e, right image) shows the spectra on the same spots (a-e) at $\theta_E = 90^\circ$. The intensity ratios between the bands at 817 cm^{-1} and 1531 cm^{-1} for $\theta_E = 90^\circ$ and $\theta_E = 0$ are shown in Table 5.3. Three IR spectra are shown in Figures 5.8A and 5.8B (spectra, a-c) that are belonging to three points [(a-c) in Figure 5.8C] on the molecular side (left side of the vertical line) and two spectra are shown in Figures 5.8A and 5.8B (spectra, d-e) belonging to two points (d-e) on the clean side (right side of the vertical line).

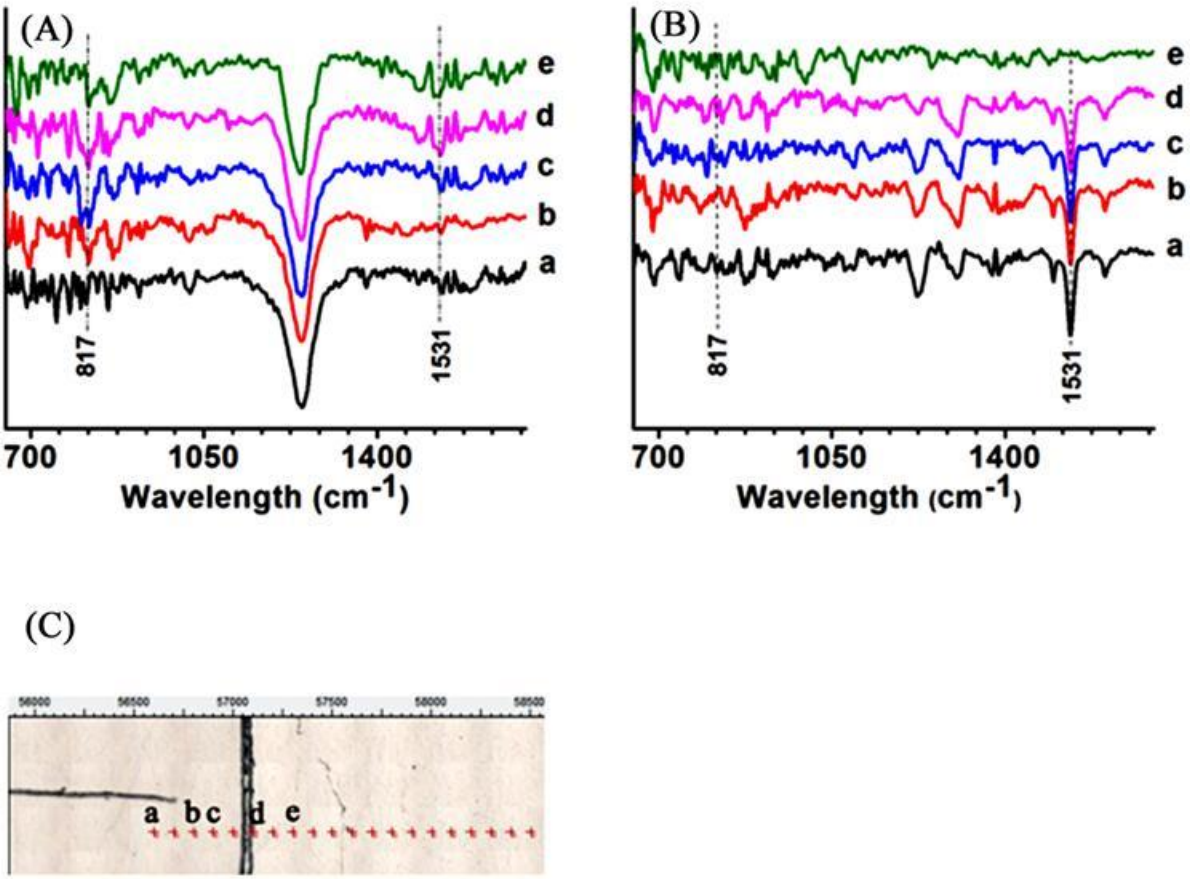

Figure 5-8. Mid-IR mapping spectra of B4Q1 on steel substrate, (A) at $\theta_E = 0^\circ$ (upper left) and (B) $\theta_E = 90^\circ$ (upper right). (C) The IR spectra (a-e) represent the points from the molecular side to the clean side. These points are shown in the optical image map at the bottom. The spacing between sample points (red marks) is 100 µm, for a total cross-section length of about 2 mm.

Table 5-3: Intensity ratio of the selected IR absorption bands for $\theta_E = 0^\circ$ and $\theta_E = 90^\circ$ of B4Q1.

	817 cm^{-1} / 1531 cm^{-1} for $\theta_E = 90^\circ$	817cm^{-1} / 1531 cm^{-1} for $\theta_E = 0^\circ$
1st point (a) of the mapping image.	0.24	1.23
3rd point (b)	0.07	3.42
4th point (c)	0.24	2.45
6th point (d) after the molecular edge	0.25	1.44
8th point (e)	4.43	1.55

Table 5.3 shows that the overall intensity ratios for $\theta_E = 90^\circ$ are very low in comparison to the intensity ratios for $\theta_E = 0^\circ$ in the molecular region (points a-c). This lower intensity ratio means that the molecules are more aligned with the electric field for $\theta_E = 90^\circ$ than $\theta_E = 0^\circ$. This is an indication of B4Q1 molecules standing on their edge or standing up, interacting in the same way as B5 and B3Q2 molecules. On the clean region, the first point (d) shows the presence of molecules and shows a trend in the ratio similar to the organic film side (low ratio for $\theta_E = 90^\circ$ and higher for $\theta_E = 0^\circ$). It means that B4Q1 molecules form multilayers until this point (d), and they are also standing on their edge or standing up up to this point. However, the last instance of B4Q1 molecules observed at point (e) shows an increase in the intensity ratio for $\theta_E = 90^\circ$ and decrease in ratio for $\theta_E = 0^\circ$. This is again the indication of these molecules being oriented in lying down or standing on their edge similar to B5 and B3Q2 molecules during interaction with the iron oxide surfaces. The orientation of the fully oxidized form

(B2Q1) of the phenyl-capped aniline dimer is shown in previous work by us, to be lying down on iron oxide surfaces.[24] On the other hand, the fully reduced dimer (B3) is standing on its edge on iron oxide surfaces.[25] IR spectroscopy shows all three oxidation states of the tetramer to have either lying down or standing on their edge orientations during interaction with the surface. In the work of Poncet et all, it is shown that non-planer B5 is lying down flat on the surface.[22]

Step Height Analysis of B5, B3Q2 and B4Q1 Films on Iron Oxide Surfaces

Step heights in the molecular layer were also measured using atomic force microscopy, giving information about the thickness of the different layers formed on the surface. All three forms of PCAT were vacuum deposited for the AFM experiments. Both B5 (2.5 nm film) and B4Q1 (1 nm film) molecules were deposited at 20˚C, while the B3Q2 film (1.5 nm thick) was deposited at 24˚C substrate temperature on steel substrates.

Figure 5.9a shows the homogeneous islands of B4Q1 molecules on native oxide covered steel on which a nominally 1 nm thick film of molecules was deposited. Figure 5.9b shows the histogram of measured step heights and Figures 5.9c, d show examples of how the step height was obtained from the line profile. The histogram shows the most frequent first layer thickness of B4Q1 molecules to be ~0.5 nm, followed by 0.4 nm. Since the resolution of the AFM used is ~0.06 nm, the histogram bins used were in 0.1 nm steps. According to Evain et al.,[26] tetramer molecules lying on their edge have a thickness of ~0.57 nm and when these molecules are lying down they will form a ~0.44 nm thick layer.[26] On the other hand, if these molecules are standing up they will form a ~2.2 nm thick monolayer. The AFM step height of most of the first layer is ~0.5 nm for B4Q1 molecules, somewhere between the edge-on and face-on orientations, which

is either a result of the molecules being twisted along their axis or possibly suggesting a tilt angle of ~60°. The twisted configuration is the more likely explanation, also in line with mid-IR results.

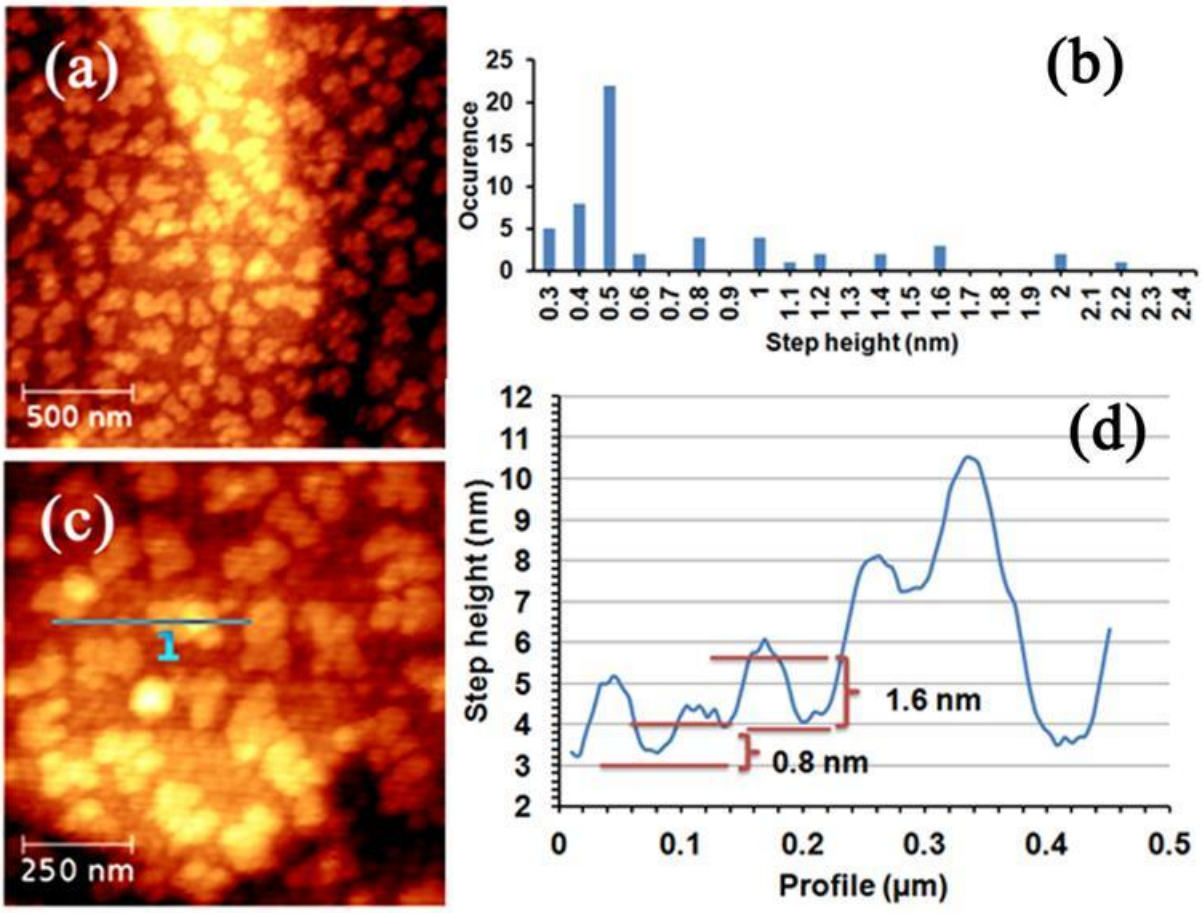

Figure 5-9. AFM height image of B4Q1 vacuum deposited (a) at 20˚C substrate temperature (2 μm × 2 μm), (b) the histogram of the step height from the line profiles, (c) an example of cross-section of AFM image, and (d) the line profile of the AFM image (c).

The step height analysis of the B5 molecules is shown in Figures 5.10a, b. In the histogram (Figure 5.10b) the most frequent first layer thickness of B5 molecules are found to be ~0.5 nm and ~0.4 nm followed by 0.3 nm. These results mean that B5 molecules largely prefer the face-

on lying down orientation. There is also a considerable occurrence of 0.8 nm steps, indicative of bilayer formation, but no indication whatsoever of standing up molecular domains (around 2.2

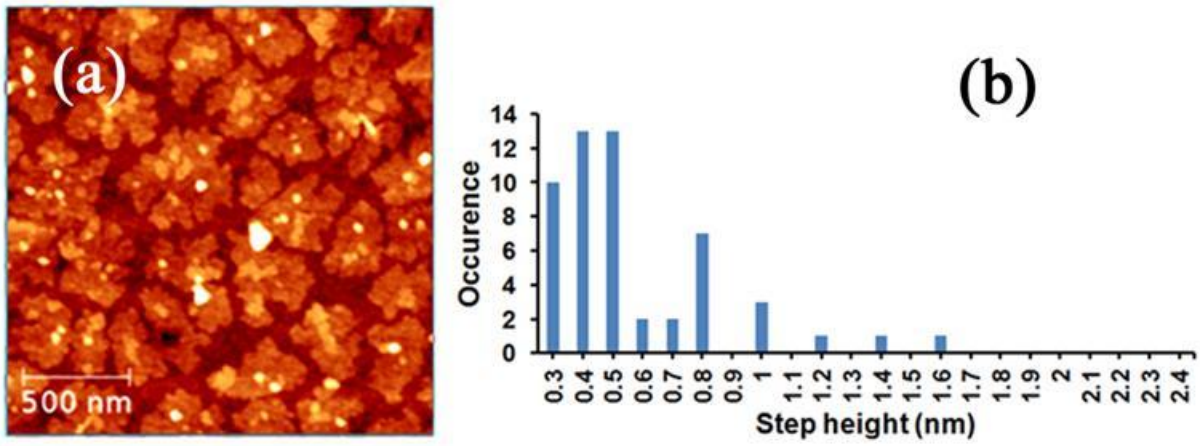

Figure 5-10. AFM height image of B5 vacuum deposited (a) at 20˚C substrate temperature (2 µm × 2 µm), (b) the histogram of the step height.

In the histogram (Figure 5.11b) for B3Q2 molecules, the most frequent first layer thickness is observed to be ~0.5 nm, indicating that these molecules are preferentially standing on edge compared to the other two molecules (B5 & B4Q1). Some islands are less than ~0.5 nm thick, which indicated face-down orientation. The two next most common island thicknesses for these molecules that observed are ~0.8 nm and ~1.0 nm, an indication of multilayer formation on the surface. B3Q2 molecules prefer to form multilayers (~0.8 nm and ~1.0 nm) due to strong interactions with each other. Unlike for B5, there is a small but distinct population of 2.2 nm steps, consistent with either multilayer formation or molecules standing on end. This is consistent with the diminished surface interactions of B3Q2 molecules.

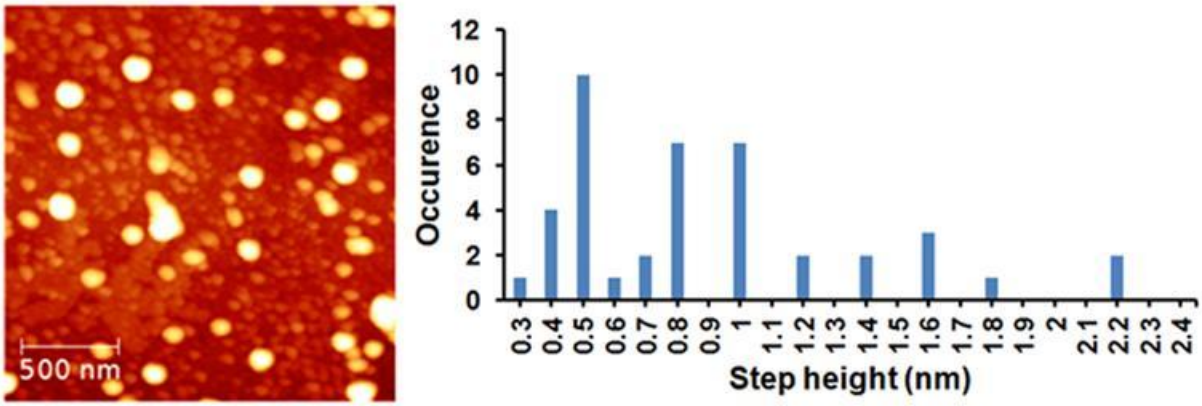

Figure 5-11. AFM height image of B3Q2 vacuum deposited (a) at 24˚C substrate temperature (2 µm × 2 µm), (b) the histogram of the step height.

Electrochemical Impedance Spectroscopy (EIS) Measurements of B5, B3Q2 and B4Q1 Coated Steel Surfaces

The corrosion performance of B5, B3Q2 and B4Q1 coated steel was monitored using EIS measurements. Two kinds of samples (coated for 24 hours or one week before EIS) were prepared by coating (drop casting) steel coupons with each of the molecules.

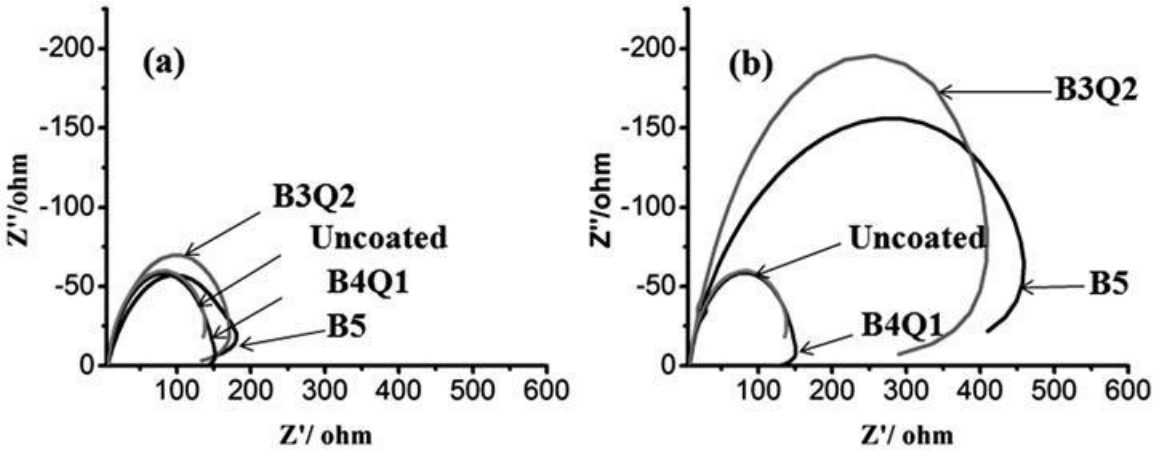

Figure 5-12. Nyquist plots of (a) polished steel samples freshly (24hrs) coated with B5, B3Q2, B4Q1 and uncoated and (b) uncoated steel samples and coated for one week with B5, B3Q2, and B4Q1, measured after immersion in 3.5% NaCl.

The 24-hour samples were denoted as fresh samples and one-week-old samples as aged samples. Figure 5.12a shows Nyquist plots of samples freshly coated (24 hours) with B5, B3Q2, B4Q1 as well as uncoated samples. The semicircle represents the charge transfer resistance of the interface between the metal (oxide) and the coating for coated samples, and the interface between metal (oxide) and the solution for uncoated samples. A larger diameter of the semicircle indicates better corrosion resistance of the coating.[27] Figure 5.12a allows to qualitatively conclude that among the freshly coated samples B5 provides the highest corrosion resistance, followed by B3Q2 coated steel. B4Q1 results in less corrosion resistance than the other two molecules. When the samples were kept for one week after coating with the molecules they show better corrosion resistance and the trend stays the same, meaning that corrosion resistance increased with time due to molecules settling down on the surface (Figure 5.12b). However, B4Q1 coated samples stay steady with time neither increasing corrosion

resistance nor being degraded. In this paper the EIS result is qualitatively discussed and the complex behavior of the plot (low frequency capacitive and inductive effects) is yet to be explored.

Weight Loss Measurement of the EIS Samples

The degree to which a coating protects the underlying surface can also be ascertained through measuring weight loss. The weights of both aged and fresh EIS samples were measured before and after their EIS tests. The samples were rinsed with acetone, methanol, and DI water before weighing. The inhibition efficiency was measured using equation 13, where W^0 is the weight loss of uncoated samples and W^1 is the weight loss of the coated samples.[27]

$$\%IE = \frac{W^0 - W^1}{W^0} \times 100\% \text{ --------- } (13)^{21}$$

Table 5.4 shows the inhibition efficiency and weight loss of the uncoated iron oxide surface and freshly (24 hours) coated samples with B5, B3Q2, and B4Q1 after 48 hours of EIS measurements. It shows that B5 and B4Q1 loose almost the same amount, and less weight than B3Q2, which makes their corrosion inhibition efficiency higher (~66%). B3Q2 would in fact seem to initiate corrosion as indicated by the negative value. Table 5.5 shows the weight loss of the uncoated iron oxide surface and aged samples (one week) coated with B5, B3Q2, and B4Q1 after 48 hours of EIS measurements. Even though B3Q2 improved a lot in the total weight loss with time, still the B5 and the B4Q1 coatings are showing better results.

Table 5-4: Inhibition efficiency after 48 hrs EIS measurement using weight loss of uncoated iron oxide surface and freshly (24hrs) coated with B5, B3Q2, and B4Q1 in 3.5% NaCl.

sample	Weight before EIS exp.(g)	Weight after EIS exp.(g)	Weight loss of Fresh samples (g)	Inhibition efficiency for fresh samples %IE
Uncoated mild steel coupon	3.2105	3.1825	0.0280	
Coated with B5	3.7323	3.7227	0.0093	66.78
Coated with B4Q1	3.7370	3.7275	0.0095	66.07
Coated with B3Q2	4.0460	3.9950	0.0510	-82.14

Table 5-5: Inhibition efficiency after 48 hours EIS measurement using weight loss of uncoated iron oxide surface and aged (one week old) coated with B5, B3Q2, and B4Q1 in 3.5% NaCl.

sample	Weight before EIS exp.(g)	Weight after EIS exp.(g)	Total weight loss of aged samples (g)	Weight loss of the middle part (g)	Weight loss of the crevice corrosion (g)
Uncoated mild steel coupon	3.2105	3.1825	0.0280		
Coated with B5	3.5244	3.5132	0.0112	0.0065	0.0047
Coated with B4Q1	3.5055	3.4922	0.0133	0.0061	0.0072
Coated with B3Q2	4.0702	4.0351	0.0351	0.0172	0.0173

The aged samples were further studied to observe the corrosion effect visually under an optical microscope and by optical surface profiler. Figure 5.13 shows the aged samples before and after EIS test and the related optical line scans. The circle shown on those samples is the area exposed to 3.5% aqueous NaCl for 48 hours during the EIS test. The edge of the circle is about ~2 mm wide. The optical line scan was taken approximately across the centre of the circle from edge to edge. It can be seen from Figures 5.13a, b for the B4Q1 sample and Figures 5.13c, d for the B3Q2 sample and its laser line scan that mostly crevice corrosion takes place at the edge of the circle as well as small subsequent corrosion progress across the surface on both samples. The crevice corrosion could be due to tightening of the ring creating large defects on the coatings at the edge of the ring which initiate localized corrosion. The average depth of the corrosion inside the ring of B4Q1 and B3Q2 coated samples are ~1.86 µm and ~ 5.26 µm, respectively. The B5 coated sample shows less crevice corrosion compared to the other two coated samples and the depth of corrosion inside the ring of this sample is ~1.99 µm. Comparing these three samples with the uncoated sample (Figs. 5.13g, h), it is easy to evaluate the relative benefits of the different coatings. The uncoated sample is corroded all over the exposed area as well as at the circle edge to the same extent.

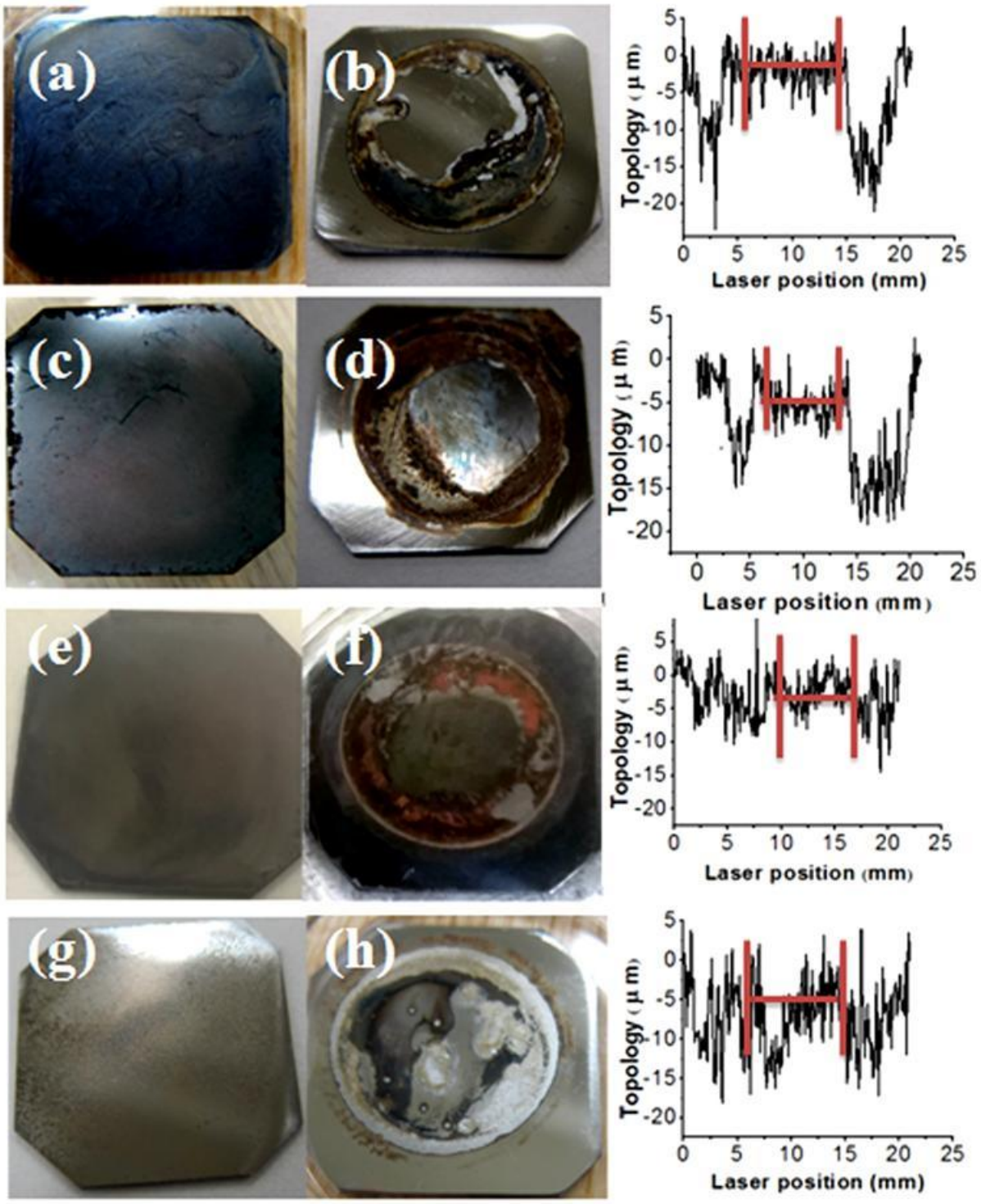

Figure 5-13. Optical image of (a & b) B4Q1 coated carbon steel before and after EIS test and laser line scan, (c & d) B3Q2 coated carbon steel before and after EIS test and laser line scan, (e

& f) B5 coated carbon steel before and after EIS test and laser line scan, (g & h) uncoated carbon steel before and after EIS test and laser line scan.

The average depth of corrosion in the middle is ~7.06 μm. Out of the total weight loss, the contribution due to corrosion inside the ring of B5 and B4Q1 is 0.0065 g and 0.0061 g respectively, with the rest being attributable to crevice corrosion at the ring. This result also indicates that B5 initiates less crevice corrosion than B4Q1, whereas, B3Q2 coated samples show equal proportions of weight loss due to crevice corrosion and also corrosion inside the ring. Among the three coatings B5 shows overall better corrosion resistance than B4Q1 and B3Q2. Even though B3Q2 shows better corrosion resistance at the beginning of the EIS test (Figures 5.13a, b), the weight loss data shows that it degraded the sample. On the other hand, B4Q1 showed low impedance at the beginning of the EIS test but from weight loss data it is as good as B5 at creating protection for the sample. It means that there is some beneficial interaction between these molecules and the iron oxide surface during the EIS test which causes them to passivate the surface.

Interactions of B5, B3Q2 and B4Q1 with Iron Oxide Surfaces after Completion of EIS Tests

The effectiveness of these molecules for corrosion inhibition depends on their interactions with the native iron oxide layer. Figure 5.14a shows a Raman spectrum of B5 drop cast from methanol onto a steel substrate before the EIS test. It is comparable to the spectrum in Figure 5.3b of a similar sample. B5 tends to transform in small part into the semiquinone form (bands 1639 and 1337 cm^{-1}), a very small portion into B3Q2 (1571 cm^{-1}) and B4Q1 (1496 and 1606

cm^{-1}) by interacting with the native oxide of steel while it is dissolved in methanol. On the other hand, after the EIS test is complete (Figure 5.14b) Raman bands at 1488, 1565 and 1415 cm^{-1} emerge corresponding to B3Q2.[16] The band at 1352 cm^{-1} belongs to the semiquinone species[18] and the others belong to B5.[16] This means that the fully reduced B5 molecules tend to convert mostly into the fully oxidized B3Q2 form during the EIS test.

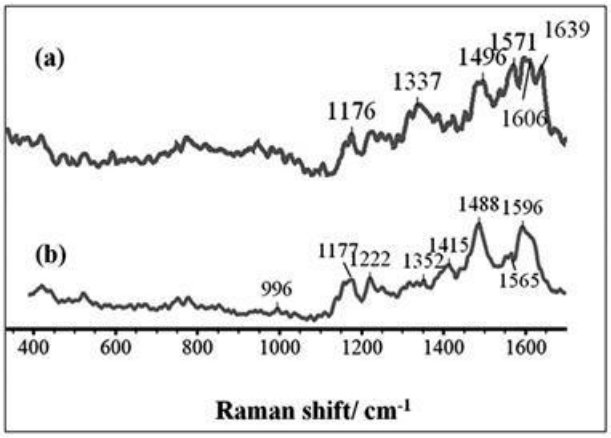

Figure 5-14. Raman spectra of B5 molecules on steel surface (a) before EIS test (b) after EIS test

The Raman spectrum of B3Q2 on a steel substrate after drop casting from methanolic solution is shown after the EIS test in Figures 5.15a, b which corresponds to a thin and thick layer of molecules, respectively. Thin and thick are differentiated by visual inspection under an optical microscope. The Raman spectrum shows that when B3Q2 is very close to the iron oxide surface (Figure 5.15a, thin film) some portion turns into the semiquinone species due to interactions with the surface (1408 and 1252 cm^{-1}) and the rest turns into B4Q1 (1497, 1593 and 1606 cm^{-1}).[16,17,18] For the thick film, the interactions are mostly between molecules. The Raman spectrum

of a thick film of B3Q2 after the EIS test shows in Figure 5.15b that these molecules partially turn into B4Q1 (1497 and 1590 cm^{-1}),[16] with the rest remaining as B3Q2.

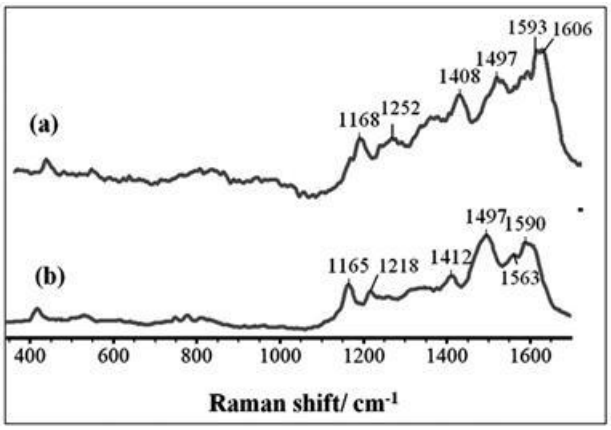

Figure 5-15. Raman spectra of B3Q2 after EIS test, (a) thin films of molecules (b) thick films of molecules.

Figures 5.16a, b show the Raman bands of B4Q1 drop cast from methanol onto native oxide before and after the EIS test. We have already discussed the impact that methanol has on B4Q1. Methanol changes the oxidation states in part to semiquinone and the rest to B3Q2. The Raman bands before the EIS test show semiquinone bands at 1407 and 1635 cm^{-1}.[17] The bands at 1568 and 1176 cm^{-1} are an indication of B4Q1 tending to transform into fully oxidized B3Q2 upon interaction with the iron oxide surface in the presence of methanol.[16] On the other hand, the Raman spectrum after EIS shows that the B4Q1 molecules turn back mostly to B4Q1 (Figure 5.15b) with just small portion of semiquinone (1400 cm^{-1}) and B3Q2 (1568 cm^{-}) left.

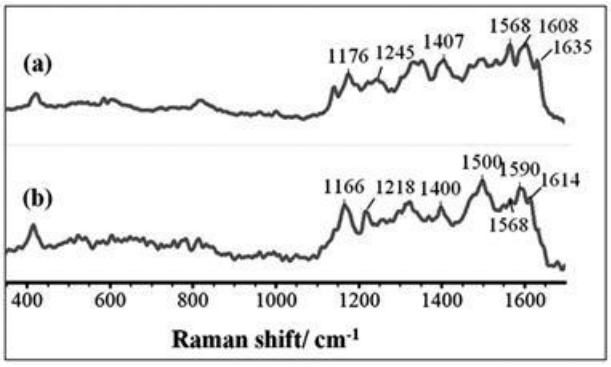

Figure 5-16. Raman spectra of B4Q1, (a) molecules before EIS test (b) molecules after EIS test.

Comparing the EIS test with weight loss data and with the optical line scan results it can be concluded that B5 is much more effective at inhibiting corrosion than the other two molecules. B5 molecules have 4 amine groups in their chain which allow them to bond more strongly with the surface than B4Q1 which has only two. A combination of amine and imine groups is also beneficial to improving the interactions within the molecular film.[25] Above it was shown that drop cast B5 molecules bond strongly to iron oxide surfaces. After 48 hours of EIS testing there are still B5 molecules left on the surface, some turning into the semiquinone form and B3Q2. These leftover B5 and semiquinone species continue to protect the surface making a physical barrier. In contrast, B3Q2 has no amine groups resulting in only weak bonding to the surface. Even though the EIS test shows B3Q2 to be second best in corrosion resistance, the weight loss data does not bear out this story. This is because when interacting with the native oxide surface before the EIS test, B3Q2 transforms into B4Q1 and the semiquinone form which allows the molecules that are very close to the surface to stick to the surface strongly and protect. But with time (48 hours of EIS test) the molecules that are not close to the surface are removed in their B3Q2 form (Figure 5.15b) which causes degradation of the surface. On the other hand, before

the EIS test the B4Q1 molecules that are close to the surface transform into the semiquinone and B3Q2 forms by interacting with the iron oxide surface. As a result, this coating showed less corrosion resistance (EIS test) at the beginning but with time (during EIS test) these molecules transform mostly into B4Q1 and the semiquinone form (Figure 5.16b). This allowed these B4Q1 molecules to stick to the surface more strongly over time and at last protect the surface which is visible in the weight loss test and the laser line scan data. This also explains why the B5 and B4Q1 molecules showed less weight loss due to crevice corrosion in the junction of the O-ring. It is because these B5 molecules by sticking to the surface make physical barrier better than B4Q1, and B4Q1 molecules are better than B3Q2. Their redox activity is also an important factor.

5.4 CONCLUSIONS

We have investigated the interactions of B5, B4Q1 and B3Q2 molecules with iron oxide surfaces using Raman spectroscopy. We found that methanol has no impact on B5 molecules, but it does impact B4Q1 and B3Q2, even changing their oxidation states. As a result, B4Q1 and B3Q2 interact less with the native oxide (α-Fe_2O_3) on steel surfaces in the presence of methanol. B5 molecules transform mostly into their semiquinone and B4Q1 forms when interacting with the native oxide of a steel surface. Interacting with the same surface, B4Q1 transforms mostly into the semiquinone and B3Q2 forms and some of the B3Q2 transforms into the semiquinone and B4Q1 forms. Mid-IR revealed that the orientation of all three molecules closer to the surface is either lying down or standing on edge but molecules in the multilayer are either lying on edge or standing up. AFM was used to identify the specific orientations and

compliment IR results during interaction with iron oxide surfaces. While the AFM results are indicative of all three molecules mostly preferring to stand on their edges, twisting of the molecular backbone and the possibility of tilted orientations make it challenging to clearly pinpoint the molecular orientation at the interface. AFM also revealed that B3Q2 molecules prefer to form multilayers due to strong interactions with each other rather than with the substrate surface. The EIS test, weight loss test and optical line measurements of the EIS samples all show that the corrosion resistance of B5 and B4Q1 coatings on steel is higher than that of B3Q2 coatings. These coatings were applied without any modification just using methanol as a solvent. Before the EIS test, the B4Q1 molecules closer to the surface transform into their semiquinone and B3Q2 forms due to interactions with the iron oxide surface. Since B3Q2 is weakly bonded to the surface, the transformed B4Q1 coating showed less corrosion resistance (EIS test) at the beginning but with time (during EIS test) these molecules transform back mostly into the B4Q1 and semiquinone forms. This allows these B4Q1 molecules, at last, to protect the surface. In contrast, B3Q2 caused degradation of the surface although EIS test shows it is the second best. This is because before the EIS test B3Q2 transforms into mostly B4Q1 and semiquinone by interacting with the native oxide surface which allows the molecules that are very close to the surface to stick to the surface strongly. But the bulk of the B3Q2 molecules that remains in the B3Q2 form detaches from the surface over time, causing degradation of the surface.

These results elucidate the role of the different oxidation states of oligoanilines and polyaniline in the corrosion protection of iron and steel, and lay the foundation for the rational design of smart corrosion inhibiting coatings. While we confirm that the oxidized (or half-

oxidized) form of PCAT is crucial for its function as corrosion inhibitor, the fully oxidized form only weakly adheres to the surface and does not form a reliable coating. Starting with the reduced form is essential to attaining a coating with co-existing multiple oxidation states, which is ultimately the best case for corrosion inhibition. In practice, likely a composite coating with tetra-aniline fragments bound to an inert backbone would be the most feasible approach, although in that case the mobility of the oligonanilines would be compromised, preventing self-healing of these coatings in the case of mechanical damage.

Acknowledgements

We thank Dr. Kirk Green from the McMaster Regional Mass Spectrometry Facility for his technical assistance and helpful discussions and Dr. Steve Kornic for assistance with Raman spectroscopy. *Some of the research described in this paper was performed at the Canadian Light Source, which is supported by the Canada Foundation for Innovation, Natural Sciences and Engineering Research Council of Canada, the University of Saskatchewan, the Government of Saskatchewan, Western Economic Diversification Canada, the National Research Council Canada, and the Canadian Institutes of Health Research.* We thank Dr. Ferenc Borondics, Dr. Scott Rosendahl and Dr. Xia Liu at CLS for their assistance in the mid-IR spectroscopy. Thanks to our group members for their kind support: Enamul Hoque, Stephen Yue Wang, Alan Awez, Alexander Imbault. Financial support was provided by National Science and Engineering Research Council of Canada through the Discovery Grant Program.

5.5 REFERENCES

1. I.Willner, B. Willner, and E. Katz, Biomolecule–nanoparticle Hybrid Systems for Bioelectronic Applications. *Bioelectrochem.*, **70**, 2–11 (2007).

2. A. Bessière, C. Duhamel, J.-C. Badot, V. Lucas, and M.-C. Certiat, Study and Optimization of a Flexible Electrochromic Device Based on Polyaniline. *Electrochim. Acta*, **49**, 2051–2055 (2004).

3. M. Michel, J. Bour, J. Petersen, C. Arnoult, F. Ettingshausen, C. Roth, and D. Ruch, Atmospheric Plasma Deposition: A New Pathway in the Design of Conducting Polymer-Based Anodes for Hydrogen Fuel Cells. *Fuel Cells*, **10**, 932–937 (2010).

4. C.-H. Wang, C.-C. Chen, H.-C. Hsu, H.-Y. Du, C.-P. Chen, J.-Y. Hwang, L. C. Chen, H.-C. Shih, J. Stejskal, and K. H. Chen, Low Methanol-Permeable Polyaniline/Nafion Composite Membrane for Direct Methanol Fuel Cells. *J. Power Sources*, **190**, 279–284 (2009).

5. W.-K. Lu, R. L. Elsenbaumer, and B. Wessling, Corrosion Protection of Mild Steel by Coatings Containing Polyaniline. *Synth. Met.*, **71**, 2163–2166 (1995).

6. D. W. DeBerry, Modification of the Electrochemical and Corrosion Behavior of Stainless Steels with an Electroactive Coating. *J. Electrochem. Soc.*, **132**, 1022–1026 (1985).

7. B. Wessling, Passivation of Metals by Coating with Polyaniline: Corrosion Potential Shift and Morphological Changes. *Adv. Mater.*, **6**, 226–228 (1994).

8. M. Rohwerder and A. Michalik, Conducting Polymers for Corrosion Protection: What Makes the Difference between Failure and Success? *Electrochim. Acta*, **53**, 1300-1313 (2007).

9. Y. Wei, H. Jamasbi, S. Cheng, S. A. Jansen, L. T. Sein, W. Zhang, and C. Wang, Corrosion Protection Properties of Coating of the Epoxy-Cured Aniline Oligomers Based on Salt Spray and UV-Salt Fog Cyclic Tests. *ACS Symp. Ser.*, **843**, 208–227 (2003).

10. W. J. Zhang, Y. H. Yu, L. Chen, H. P. Mao, C. Wang, and Y. Wei, Synthesis and Study of Phenyl-Capped Tetraaniline as an Anticorrosion Additive. *ACS Symp. Ser.*, **843**, 156–165 (2003).

11. M. T. Greiner, M. Festin, and P. Kruse, Investigation of Corrosion-Inhibiting Aniline Oligomer Thin Films on Iron Using Photoelectron Spectroscopy. *J. Phys. Chem. C*, **112**, 18991–19004 (2008).

12. A. Mohtasebi, T. Chowdhury, L. H. H. Hsu, M. C. Biesinger, and P. Kruse, Interfacial Charge Transfer between Phenyl-Capped Aniline Tetramer Films and Iron Oxide Surfaces. *J. Phys. Chem. C*, **120**, 29248-29263 (2016).

13. L. H. H. Hsu, E. Hoque, P. Kruse, and P. R. Selvaganapathy, A Carbon Nanotube Based Resettable Sensor for Measuring Free Chlorine in Drinking Water. *Appl. Phys. Lett.*, **106**, 063102 (2015).

14. W. Wang and A. G. MacDiarmid, New Synthesis of Phenyl/phenyl End-Capped Tetraaniline in the Leucoemeraldine and Emeraldine Oxidation States. *Synth. Met.*, **129**, 199–205 (2002).

15. D. Nečas and P. Klapetek, Gwyddion: an open-source software for SPM data analysis. *Open Phys.*, **10**, 181–188 (2012).

16. M.-I. Boyer, S. Quillard, E. Rebourt, G. Louarn, J. P. Buisson, A. Monkman, and S. Lefrant, Vibrational Analysis of Polyaniline: A Model Compound Approach. *J. Phys. Chem. B*, **102**, 7382–7392 (1998).

17. H. de Santana, S. Quillard, E. Fayad, and G. Louarn, In Situ UV–vis and Raman Spectroscopic Studies of the Electrochemical Behavior of N,N'-Diphenyl-1,4-Phenylenediamine. *Synth. Met.*, **156**, 81–85 (2006).

18. T. Lindfors and A. Ivaska, Raman Based pH Measurements with Polyaniline. *J. Electroanal. Chem.*, **580**, 320–329 (2005).

19. T. Lindfors, C. Kvarnström, and A. Ivaska, Raman and UV–vis Spectroscopic Study of Polyaniline Membranes Containing a Bulky Cationic Additive. *J. Electroanal. Chem.*, **518**, 131–138 (2002).

20. D. L. A. de Faria, S. Venâncio Silva, and M. T. de Oliveira, Raman Microspectroscopy of Some Iron Oxides and Oxyhydroxides. *J. Raman Spectrosc.*, **28**, 873–878 (1997).

21. M. Boyer, S. Quillard, M. Cochet, G. Louarn, and S. Lefrant, RRS Characterization of Selected Oligomers of Polyaniline in Situ Spectroelectrochemical Study. *Electrochim. Acta*, **44**, 1981–1987 (1999).

22. M. Poncet, B. Corraze, S. Quillard, W. Wang, and A. G. Macdiarmid, Elaboration and Characterizations of Oligoaniline Thin Films. *Thin Solid Films*, **458**, 32–36 (2004).

23. M. Cochet, G. Louarn, S. Quillard, M. I. Boyer, J. P. Buisson, and S. Lefrant, Theoretical and Experimental Vibrational Study of Polyaniline in Base Forms: Non-Planar Analysis. Part I. *J. Raman Spectrosc.*, **31**, 1029–1039 (2000).

24. T. Chowdhury, A. Mohtasebi, and P. Kruse, Nature of the Interaction of N,N'-Diphenyl-1,4-Benzoquinonediimine with Iron Oxide Surfaces and its Mobility on the Same Surfaces. *J. Phys. Chem. C*, **121**, 2294-2302 (2017).

25. T. Chowdhury, E. Hoque, A. Mohtasebi, and P. Kruse, Nature of the Interaction of N,N'-Diphenyl-1,4-Phenylenediamine with Iron Oxide Surfaces. *J. Phys. Chem. C*, **121**, 2721-2729 (2017).

26. M. Evain, S. Quillard, B. Corraze, W. Wang, and A. G. MacDiarmid, A Phenyl-End-Capped Tetramer of Aniline. *Acta Crystallogr. Sect. E Struct. Rep. Online*, **58**, 0343–0344 (2002).

27. S. Velrani, B. Jeyaprabha, and P. Prakash, Inhibition of mild steel corrosion in 3.5% NaCl medium using 1-butyl-3-methylimidazolium chloride. *Int. J. Innovative Sci., Eng. Technol.,* **1**, 57-69 (2014).

28. W. Zheng, M. Angelopoulos, A. J. Epstein, and A. G. MacDiarmid, Experimental Evidence for Hydrogen Bonding in Polyaniline: Mechanism of Aggregate Formation and Dependency on Oxidation State. *Macromolecules*, **30**, 2953–2955 (1997).

TOC Graphic

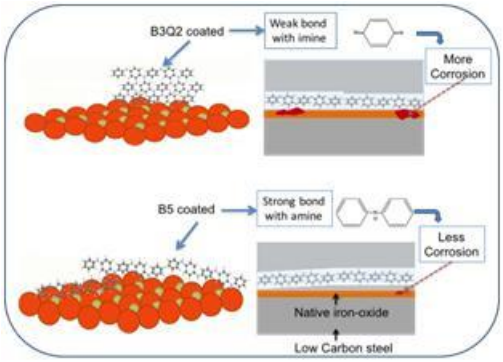

CHAPTER -6
SUMMARY AND FUTURE WORK

6.1 SUMMARY

The fundamental understanding of the interactions between the native iron oxide and redox-active aniline oligomers is very important since they have many potential applications in the anti-corrosion coating industry and also in organic electronics. A large number of corrosion studies have been performed without fully understanding the underlying surface chemistry of redox-active molecules on iron oxide. This thesis enhances and deepens the fundamental understanding of the interactions of aniline oligomers with the iron oxide surface. Our study will be useful in the corrosion coating industry as well as in other smart coatings and molecular electronics.

We investigated two different redox-active aniline oligomers. One of them is the phenyl-capped aniline dimer, the smallest possible redox-active oligomer with two oxidation states [fully reduced (DPPD) and fully oxidized (B2Q1)]. The other one is the phenyl-capped aniline tetramer (PCAT) with three oxidation states [leucoemeraldine or B5 base form ("fully reduced"; benzoid; amine) emeraldine or B4Q1 base form ("half-oxidized"; part benzoid, part quinoid; part amine, part imine) and pernigraniline or B3Q2 base form ("fully oxidized"; quinoid; imine)]. The phenyl-capped version of the oligomers was chosen to avoid the polymerization of the molecules on the surface. Although the dimer does not represent the perfect model of the redox behavior of polyaniline because of the missing half oxidized form, a pair of the amino groups is enough to cycle through two different oxidation states. On the other hand, the phenyl-capped aniline tetramer (PCAT) can fully mimic the redox properties of PANI and also the

corrosion inhibition properties of polyaniline on iron and steel. All different oxidation states needed to be studied individually in order to build up a full understanding of the system.

The interaction of the different molecules with iron oxide surfaces was investigated using a range of techniques, including Raman spectroscopy. For all five molecules, two kinds of samples were investigated. One kind of samples was obtained by drop-casting molecules on steel substrates to study the interactions between molecules and the native oxide of the steel surfaces. Another kind was obtained by mixing powders of molecules and α-Fe_2O_3 nanoparticles. This shows the effect of methanol on all oxidized and half oxidized molecules but not on reduced molecules. We found that oxidized and half oxidized molecules interact less with the native oxide surface in the presence of methanol solvent, because methanol can interfere with the interactions through its hydroxyl group. Raman spectroscopy further reveals that both DPPD and B2Q1 reach an intermediate unstable semiquinone state by interacting with the iron oxide surface, indicative of charge transfer between them. In the case of PCAT, the interaction experiment shows that B5 molecules close to the surface transform mostly into their semiquinone and B4Q1 forms when interacting with the native oxide of a steel surface. Interacting with the same surface, B4Q1 close to the surface transforms mostly into its semiquinone and B3Q2 forms, and B3Q2 transforms into its semiquinone and B4Q1 forms. Both the powder mixture and the drop cast PCAT molecules show the same reaction product after interaction with the iron oxide surface. The interactions of these molecules also depend on their orientation on the surface.

Mid-IR spectroscopy was used to study the orientations of all dimer and tetramer molecules. This shows that the DPPD molecules closer to the surface are stand on their edge (tilted by 45°)

but B2Q1 molecules closest to the surface prefer a lying down orientation. In the case of multilayers, there are less restrictions on how these molecules orient themselves, and they can be either standing on their edge or standing up. Mid- IR shows that PCAT molecules in all three oxidation states close to the surface are oriented either lying down or standing on their edge. To confirm the specific orientation and to compliment the mid-IR results, atomic force microscopy (AFM) was used. The AFM results identified that all three PCAT molecules mostly preferred to stay standing on their edge. Due to twisting and tilt angles, it is difficult to identify whether some molecules are completely lying down or not. AFM confirms the mid-IR results of the orientation of the DPPD and B2Q1 molecules. AFM also revealed that both the oxidized dimer and tetramer (B2Q1 and B3Q2) molecules prefer to form multilayers due to strong interactions with each other than with the substrate surface.

Thermal desorption experiments were performed using thermo-gravimetric analysis (TGA) to measure the strength of the interactions of both DPPD and B2Q1 with iron oxide, and also to complement the orientation information of these molecules obtained by AFM and mid-IR. TGA shows that DPPD molecules are chemisorbed on the surface. The analysis also shows that the chemisorption energies of DPPD tend to increase with coverage due to cooperative molecular interactions until complete monolayer coverage has been achieved, and during the second layer formation the chemisorption energy drops slightly due to a change in molecular orientation but rises again afterward. On the other hand, B2Q1 species are chemisorbed on the iron oxide surface at monolayer or sub-monolayer coverage, but in the following multilayers molecules strongly interact with each other and only weakly with the surface. The obtained results for the strengths of surface interactions of DPPD and B2Q1 with iron oxide surfaces are representative

of the reduced and oxidized forms respectively, of the oligoanilines and polyaniline. Based on TGA results and the migration observed in the AFM image analysis of a sample with mixed DPPD and B2Q1 molecules one can conclude that B2Q1 molecules are the mobile species on the iron oxide surface.

Since PCAT mimics the redox system of PANI and has been shown to inhibit corrosion equally well, the corrosion resistance of all three PCAT (B5, B4Q1, and B3Q2) coatings on low carbon steel was investigated using EIS, weight loss test and laser line measurements. The combination of all three measurements shows that the corrosion resistance of B5 and B4Q1 coatings on low carbon steel is higher than that of B3Q2 coatings. All these coatings were applied to steel surfaces without any modification, just using methanol as a solvent. The interaction experiments showed that all these molecules were interconverting to different oxidation states upon close contact with the iron oxide surface. As a result, before the EIS test, the B4Q1 molecules closer to the surface transformed into their semiquinone and B3Q2 forms by interacting with the iron oxide surface. Since B3Q2 is weakly bonded to the surface, possibly due to a lack of amino groups in the molecular chain, it can easily detach from the surface. As a result, the B4Q1 coating at the beginning of the EIS test showed less corrosion resistance but as it transformed back mostly into B4Q1 and semiquinone molecules during the EIS test, the surface was protected at the end. In contrast, before the EIS test, the B3Q2 molecules that were very close to the surface transformed into mostly into the B4Q1 form and semiquinone by interacting with the native oxide surface which allowed these molecules to stick strongly to the surface by hydrogen bonding which tells us why at the beginning of the EIS test the B3Q2 coating showed the second best corrosion resistance. The B3Q2 molecules in the multilayers

remained in the B3Q2 form and were detached over time due to weak bonding to the surface which caused degradation of the surface with time compared to the other two cases discussed above. In the case of B5 molecules, their ability to strongly stick to the surface through hydrogen bonding and to transform into more B4Q1 form than B3Q2 form during interaction let them offer stronger resistance to corrosion than the resistance offered by B4Q1 and B3Q2 molecules. Having amino groups in the chain helps B5 and B4Q1 molecules to form strong hydrogen bonds with the hydrated iron oxide surface which are absent in the B3Q2 molecules. As a result, B3Q2 molecules become more mobile on the surface and aggregate among themselves rather than coating the surface. This result suggests that the fully oxidized molecules are the ones that take part in the self-healing of the coatings. These molecules can migrate in the fully oxidized state and with time they change their oxidation states to half reduced states by passivating (oxidizing) substrate surface and become stable on the new sites of the substrate surface. The way of interaction with the surface and the direction of change in oxidation states impact the corrosion inhibition properties of the different forms of PCAT as well as any related molecules. Till now the self-healing properties of PANI were observed but never really understood or studied in detail. Our detailed understanding of the interactions of the oligoanilines with iron oxide surfaces will open the door not only for corrosion control but also for designing smart coatings and modifying electronic devices. Our results will benefit not only systems based on oligomers but also systems using polyaniline and other related polymers.

6.2 FUTURE WORK:

Our full understanding of the interactions of aniline oligomers with iron oxide surfaces can be a foundation for more future research activities related to any redox-active oligomers or

polymers. Indeed, to gain the full control of the molecules there is plenty of room for more research in the future. Thermal desorption studies were conducted to quantify the strength of the surface interactions of DPPD and B2Q1. Based on those results and also relating orientations and interaction results of all three PCAT molecules, assumptions were made for the interaction strength of the B5, B4Q1 and B3Q2 molecules, but no specific number was calculated for the activation energy to quantify the chemisorption or physisorption of these molecules. TGA experiments can be carried out for different coverages for each of the three molecules on iron oxide surfaces and the results can be used to calculate activation energy for each of the molecules. This will give a quantitative result for the energy of interaction for these molecules. If the α-Fe_2O_3 nanopowder can be dehydrated and the same TGA experiment is performed, it is possible to find out if the water molecules are blocking the bonding sites of the oxide surface.

The mobility of phenyl-capped dimer molecules was observed qualitatively by AFM and mid-IR. Neither the dimer nor the tetramer molecules' mobility were quantitatively calculated and defined so far. There are several quantitive studies on organic film growth on the inorganic substrate.[1,2] One of the studies was about the growth kinetics of a tetracene film on silicon dioxide which was calculated using island size distribution measurement from the AFM image by Shi et al (2008).[1] They showed that the film growth on silicon dioxide was diffusion mediated and their calculation showed that the smallest stable tetracene island consisted of 4 molecules. Similar studies can be performed on B5, B3Q2 and B4Q1 molecules. These studies need homogenous surface coverage of the molecules on the surface. Getting a homogenous film of oxidized molecules requires to avoid dewetting and is challenging but doable. The substrate

temperature during vacuum deposition should be optimized and go down closer to 0˚C to get a continuous film of molecules. Reduced and partially reduced molecules are easier to deposit.

The mobility of the PCAT and dimer molecules can also be tracked as a function of temperature, humidity, and other environmental influences using AFM. By heating up the AFM stage it is possible to observe the temperature effect on mobility directly from AFM images. Purging dry nitrogen once and then atmospheric oxygen again in the AFM chamber mobility can be turned off and on. The effect of water can also be observed by purging humid air or humid nitrogen in that chamber.

All the experiments done in the 3rd study (chapter 5) can be repeated to study the interaction of PCAT on magnetite (Fe_3O_4) surfaces. Studying the interactions of PCAT with magnetite is more complex because it can contains a mix of Fe (II) and Fe (III) oxidation states in the bulk.

There is another oligomer of PANI called amine-capped aniline trimer (ACAT) which possesses similar redox properties as PANI and PCAT. This molecule fully mimics the electronic behavior of PANI (leucoemeraldine, emeraldine and pernigraniline oxidation states), and can inhibit corrosion of steel substrate even better than PANI.[3-5] ACAT has a different end-capping compared to the phenyl-capped dimers and PCAT used in this thesis which will make their surface interactions more complex because they can also polymerize on the surface during the interaction. Prior work in our group showed that vacuum depositing ACAT is a great challenge because it decomposes with temperature. On the other hand, the amine-capped termination of these molecules makes it more likely that these molecules will bond more strongly with the iron oxide surfaces than PCAT or the phenyl-capped dimer. Using our prior

knowledge and also the understanding of the interaction characteristics of dimer and tetramer molecules from this work, it will be worth studying the interactions of different oxidation states of ACAT on iron oxide surfaces. This will result in even better understanding of all the members in the phenyl-capped and amine-capped oligomer family. Our current work will also be useful in understanding other related polymers such as polypyrrole. Polypyrrole is also known as a good corrosion inhibitor for low carbon steel as PANI.[6,7] Any detailed investigation of interactions of this polymer with iron oxide surfaces is yet to be done. To study corrosion inhibition, one can explore little bit longer chain phenyl-capped oligomers such as phenyl-capped octamers. All oxidation states of the phenyl-capped octamer should act similarly to those of PCAT but because of the longer chain, they will be more complex.

The interactions of different oxidation states of PCAT and iron oxide surface can be utilized in chemical sensing devices because any modification in these molecular' films by acid- base or redox reactions will be detectable through conductivity measurements of the films. Since iron oxide films are inexpensive and easy to fabricate, designing such sensing devices will be economically beneficial. A very recent publication of our group showed a new sensing device detecting free chlorine in water using the redox properties of PCAT on single wall carbon nanotube (SWCNT) films. It was demonstrated that the free chlorine present in the water can p-dope the PCAT-SWCNT system into a low resistance state by oxidizing PCAT. This oxidation can be detected by probing a small voltage in it and resetting it back to the undoped state again electrochemically.[8] A similar method can be used to design sensors using PCAT/iron oxide system for sensing other oxidant chemical species.

PCAT molecules can also be used in the stabilization of iron oxide nanoparticles. A recent publication showed that polyaniline can be used in an electrochemically exfoliated graphene sheet to stabilize nanoparticles to build well-defined 2D sandwich-like hybrid nanostructures.[9] They used polyaniline (PANI) in the emeraldine base form as a dopant to couple NPs (Si, Fe_3O_4 etc.) onto EEG with either electrostatic interactions or hydrogen bonding. Since PANI has challenges, it is more feasible to use different oxidation states of PCAT to get more control on iron oxide nanoparticles as an alternative system. Again the knowledge gained from this work about the interactions of PCAT molecules with iron oxide will be very useful in such a study.

The full understanding of aniline oligomers interaction with iron oxide surface can be utilized in any organic electronics system exploring polymers or aniline oligomers. To our knowledge, we are the first group to study the interactions of all three oxidation states of redox active aniline oligomers with iron oxide surface in such detail. We believe our work will benefit most of the ongoing work and will also build up ideas for any future research related to our system.

6.3 REFERENCES:

(1) Shi, J.; Qin, X. R. Nucleation and Growth of Tetracene Films on Silicon Oxide. *Phys. Rev. B* **2008**, *78* (11), 115412.

(2) Ruiz, R.; Nickel, B.; Koch, N.; Feldman, L. C.; Haglund, R. F.; Kahn, A.; Family, F.; Scoles, G. Dynamic Scaling, Island Size Distribution, and Morphology in the Aggregation Regime of Submonolayer Pentacene Films. *Phys. Rev. Lett.* **2003**, *91* (13), 136102.

(3) Sein Jr., L. T.; Wei, Y.; Jansen, S. A. Corrosion Inhibition by Aniline Oligomers through Charge Transfer: A DFT Approach. *Synth. Met.* **2004**, *143* (1), 1–12.

(4) Huang, K.-Y. Effect of Amino-Capped Aniline Trimer on Corrosion Protection and Physical Properties for Electroactive Epoxy Thermosets. *Electrochimica Acta* **2009**, *54* (23), 5400–5407.

(5) Huang, H.-Y.; Huang, T.-C.; Yeh, T.-C.; Tsai, C.-Y.; Lai, C.-L.; Tsai, M.-H.; Yeh, J.-M.; Chou, Y.-C. Advanced Anticorrosive Materials Prepared from Amine-Capped Aniline Trimer-Based Electroactive Polyimide-Clay Nanocomposite Materials with Synergistic Effects of Redox Catalytic Capability and Gas Barrier Properties. *Polymer* **2011**, *52* (11), 2391–2400.

(6) Trung, L. M. D. and V. Q. *Layers of Inhibitor Anion – Doped Polypyrrole for Corrosion Protection of Mild Steel*; InTech, 2013.

(7) Iroh, J. O.; Su, W. Corrosion Performance of Polypyrrole Coating Applied to Low Carbon Steel by an Electrochemical Process. *Electrochimica Acta* **2000**, *46* (1), 15–24.

(8) Hsu, L. H. H.; Hoque, E.; Kruse, P.; Selvaganapathy, P. R. A Carbon Nanotube Based Resettable Sensor for Measuring Free Chlorine in Drinking Water. *Appl. Phys. Lett.* **2015**, *106* (6), 063102.

(9) Wei, W.; Wang, G.; Yang, S.; Feng, X.; Müllen, K. Efficient Coupling of Nanoparticles to Electrochemically Exfoliated Graphene. *J. Am. Chem. Soc.* **2015**, *137* (16), 5576–5581.